FORSCHUNGSZENTRUM JÜLICH GmbH

Institut für Festkörperforschung

Spin-Resolved Photoemission from Ultrathin fcc Co (100)-Films and the Influence of Oxygen Chemisorption

Wolfgang Clemens

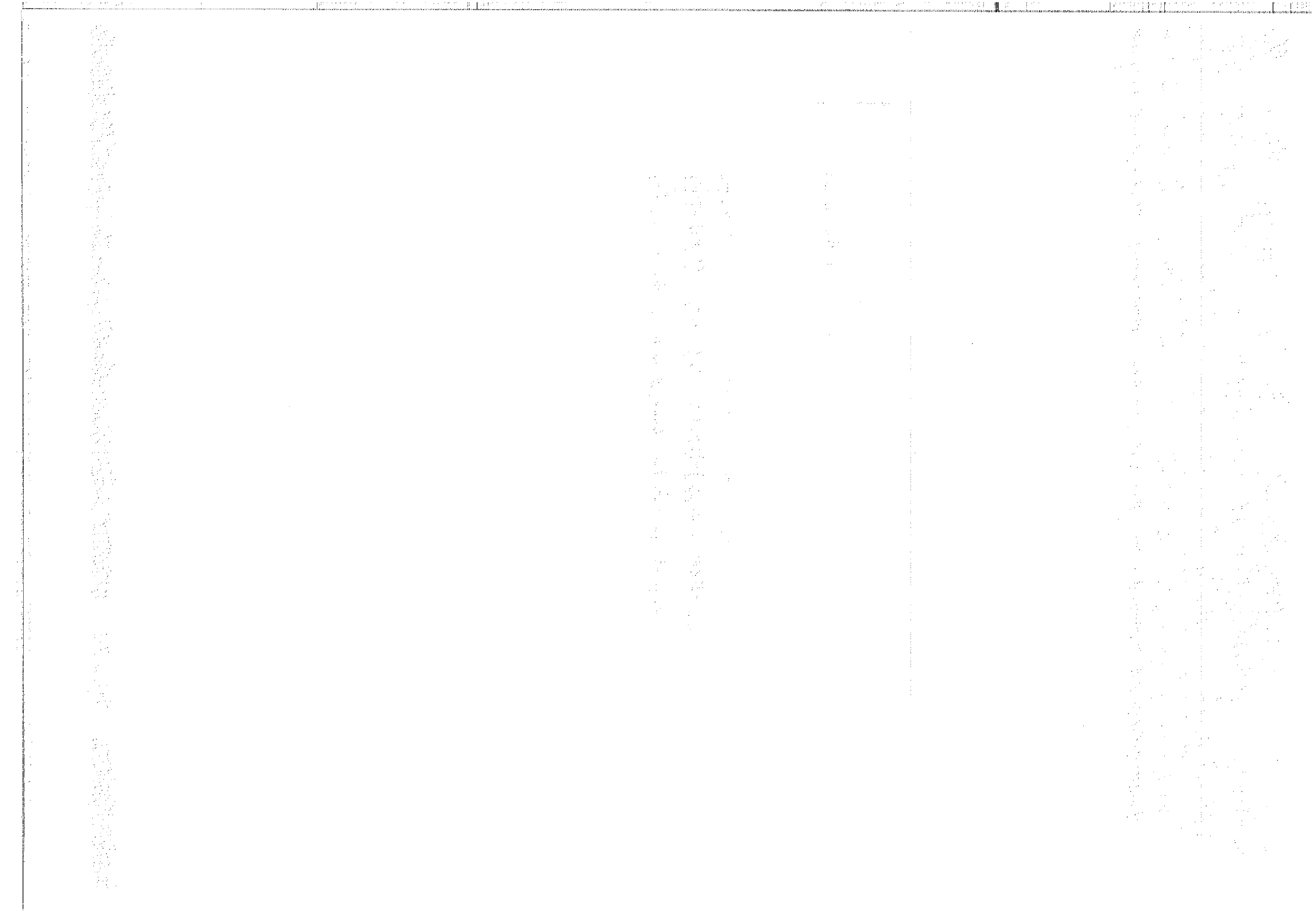

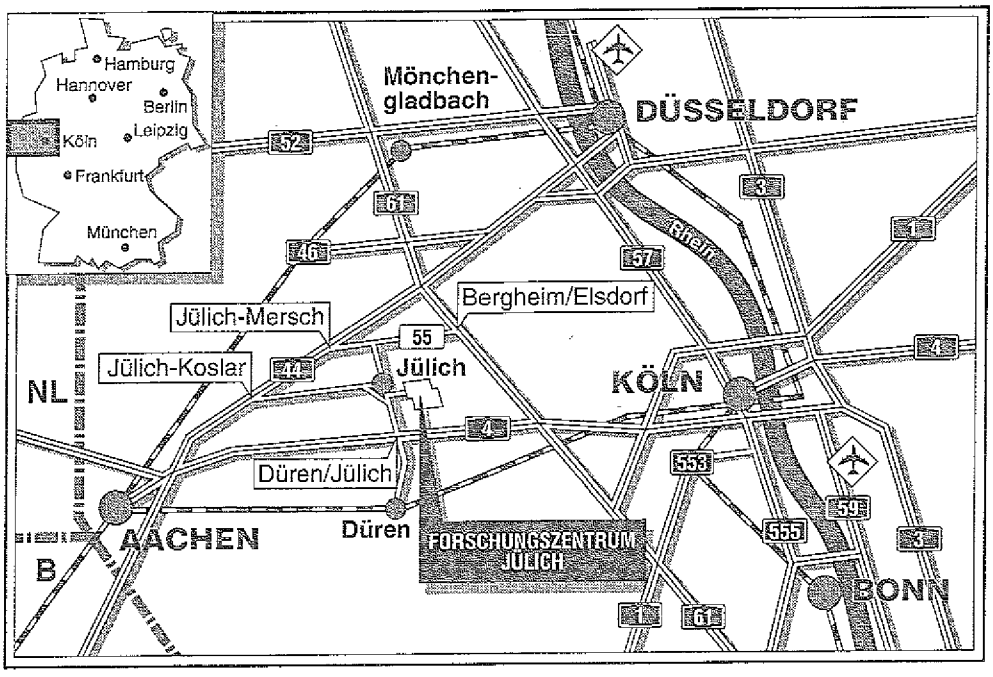

Berichte des Forschungszentrums Jülich ; 2601
ISSN 0366-0885
Institut für Festkörperforschung Jül-2601

Zu beziehen durch: Forschungszentrum Jülich GmbH · Zentralbibliothek
Postfach 1913 · D-5170 Jülich · Bundesrepublik Deutschland
Telefon: 02461/61-6102 · Telefax: 02461/61-6103 · Telex: 833556-70 kfa d

Spin-Resolved Photoemission from Ultrathin fcc Co (100)-Films and the Influence of Oxygen Chemisorption

Wolfgang Clemens

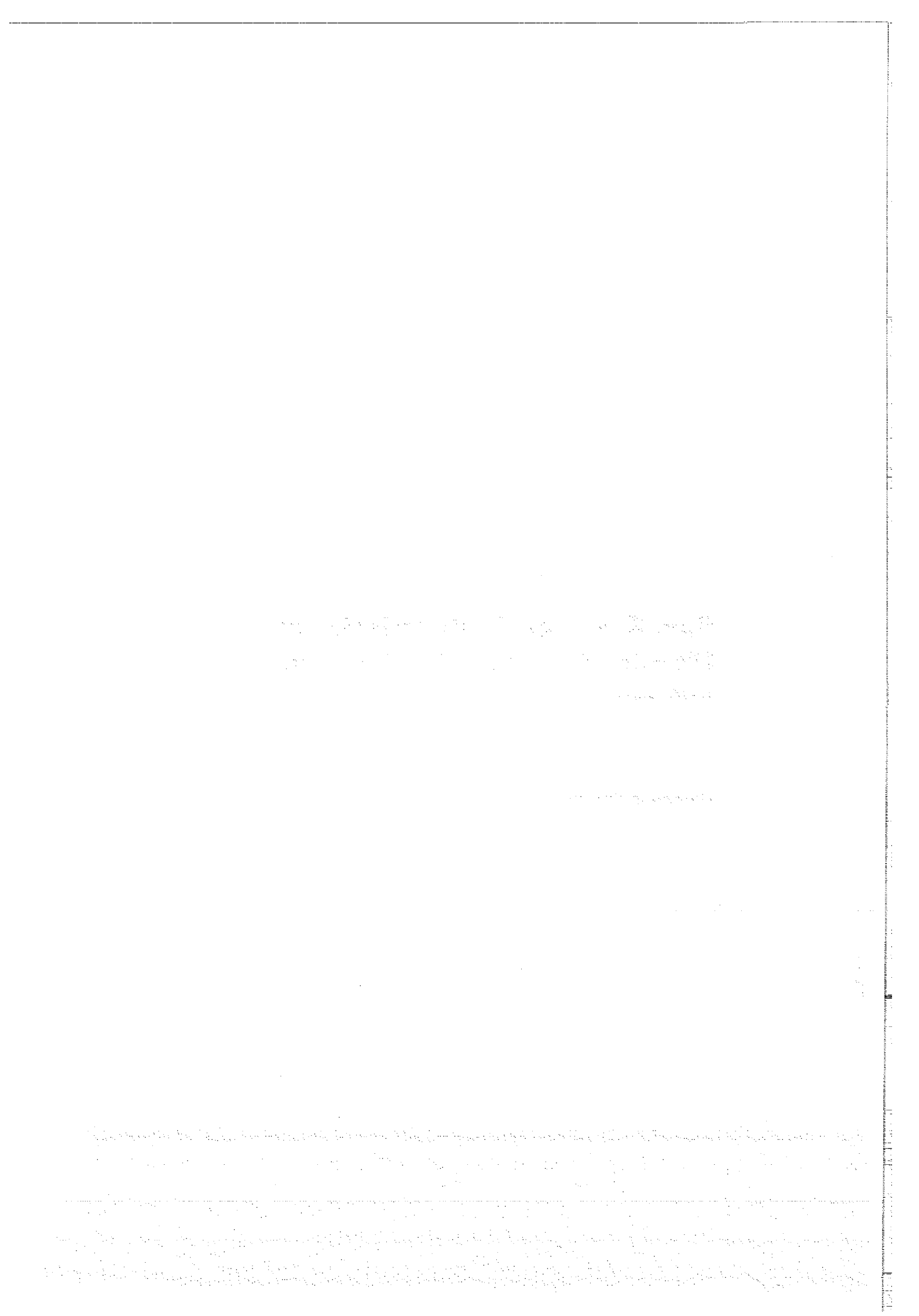

Zusammenfassung

Die spinabhängige elektronische Struktur epitaktischer Co-Überlagen auf Cu (100) und der Einfluß von O_2-Chemisorption wurde mit spin- und winkelaufgelöster Photoemissionsspektroskopie mit Synchrotronstrahlung untersucht.

Co-Lagen mit Schichtdicken von weniger als 5 Monolagen zeigen eine erhöhte Austauschaufspaltung im Zentrum der Brillouinzone, bedingt durch Quanten-Size-Effekte. Die experimentellen Ergebnisse wurden unterstützt durch FLAPW-Rechnungen für 1, 2 und 3 Co Lagen auf Cu (100). Diese Rechnungen zeigen, daß der Anstieg der mittleren Austauschaufspaltung verknüpft ist mit der Erhöhung des magnetischen Moments in ultradünnen Co-Lagen.

Sauerstoff adsorbiert dissoziativ auf der Co (100) Oberfläche in einer geordneten c(2x2) Struktur bei einer Sauerstoffzufuhr von 2 bis 7 Langmuir (bei Raumtemperatur). Die chemische Wechselwirkung zwischen Adsorbat und Substrat manifestiert sich durch eine Reduktion der Co 3d Oberflächenzustands-Emission bei E_F. Die Sauerstoff 2p-Bänder zeigen eine induzierte Austauschaufspaltung im Zentrum der Oberflächen - Brillouinzone. Bei höherer Sauerstoff-Zufuhr zeigen die Photoemissionsspektren, bedingt durch die Bildung einer CoO-Oberflächenoxid-Phase, Anzeichen für starke Korrelationseffekte in der elektronischen Struktur. Die Bildung der CoO-Oberflächenoxid-Phase wird begleitet von einer Abnahme der Spinpolarisation der Photoelektronen, was auf einen Verlust der ferromagnetischen Ordnung an der Oberfläche zurückzuführen ist. Bei niedriger Temperatur (150 K) und hoher Sauerstoffzufuhr wird die Bildung einer Co_3O_4 - Phase beobachtet.

Abstract

The spin dependent electronic structure of epitaxial Co overlayers on Cu (100) as well as the influence of O_2 chemisorption has been studied by spin and angle resolved photoemission spectroscopy with synchrotron radiation.

Co layers with a thickness below 5 monolayers show an enhanced value of the exchange splitting at the center of the Brillouin zone due to quantum size effects. The experimental results are supported by FLAPW calculations for 1, 2 and 3 Co layers on Cu (100). These calculations show that the increase of the average exchange splitting is related to the enhancement of the magnetic moment in ultrathin Co layers.

Oxygen adsorbs dissociatively on the Co (100) surface in an ordered c(2×2) structure for oxygen exposure between 2 and 7 L (at room temperature). The chemical interaction between the adsorbate and the substrate manifests itself by a reduction of the Co 3d surface state emission near E_F. The oxygen 2p-derived bands exhibit an induced exchange splitting at the center of the surface Brillouin zone. At higher oxygen exposure, corresponding to the formation of a CoO surface phase, the photoemission spectra show evidence for strong correlation effects in the electronic structure. The formation of the CoO surface oxide phase is accompanied by a decrease of the photoelectron spin polarization revealing the quenching of the surface ferromagnetic order. At low temperatures (150 K) and high exposures of O_2 the formation of a Co_3O_4 phase is observed.

Parts of this work have been published in:

Quantum Size Effects and the Enhancement of the Exchange Splitting in ultrathin Co Overlayers on Cu (100)
W.Clemens, T.Kachel, O.Rader, E.Vescovo, S.Blügel, C.Carbone, W.Eberhardt; Solid State Comm. 81 No. 9, 739 (1992)

Spin Resolved Photoemission Study of the Reaction of O_2 with fcc Co (100)
W.Clemens, E.Vescovo, T.Kachel, C.Carbone, W.Eberhardt; to be published

Contents

1. Introduction

The electronic and magnetic properties of surfaces and ultrathin (with thicknesses of some atomic layers) magnetic films are of considerable interest [Gradmann 74], [Pescia 89], [Falicov 90], [Erice 91]; (i) because they represent experimental realization of two-dimensional (2D) macroscopic quantum systems with thermodynamic and magnetic properties (like critical temperature, anisotropy) quite different from bulk materials [Jonker 86], [Heinrich 87], [Przybylski 87], [Stampanoni 87 (1)], [Liu 88], [Dürr 89], [Schneider 90 (1)]; (ii) they are technologically relevant as new materials tailored for recording and device applications.

Recent theoretical studies even predict ferromagnetism in ultrathin films of some nonmagnetic materials (e.g. Rh, Ru), evaporated on nonmagnetic single crystal substrates [Eriksson 91], [Blügel (1)]. The magnetic coupling between two magnetic films oscillates depending on the thickness of a nonmagnetic material in between [Pescia 90], [Parkin 90], [Grünberg 90]. Multilayers of alternating magnetic and nonmagnetic films can have prominent properties. Some of them have a perpendicular anisotropy [Gradmann 86], [Chappert 88], which can be used for magnetic storage with high information density. Multilayers can also have a huge magnetoresistance [Baibich 88], [Binasch 89], which is of technical interest for new magnetic recording heads.

The properties of surfaces also differ from the bulk properties. The magnetic moment of surface layers of ferromangetic materials is found to be enhanced compared to the bulk moment [Ohnishi 83], [Li C. 88]. The changes of the electronic properties on surfaces is also of great interest, because the electronic structure is modified by the influence of adsorbates [Plummer 82]. The influence of adsorbates on surface-magnetism is discussed contradictory [Johnson 90]. Some groups find magnetically "dead layers" [Schmitt 85], [Abraham 87], others find induced magnetic moments in the chemisorbed phases [Johnson 88], [Schönhense 88 (1)], [Schönhense 88 (2)]. Weber et al. [Weber 90] even find an enhancement of the Curie temperature of ultrathin magnetic films due to adsorbates.

The question of the influence of adsorbates on surface magnetism is of topical interest, because some adsorbate induced magnetic "dead layers" on the surface of thin films or multilayers would have a drastic influence on their technical application. The

solution of this question requires more data under well defined experimental conditions.

We studied the spin dependent electronic structure of ultrathin epitaxial fcc Cobalt (Co) films evaporated under ultra high vacuum conditions on the (100) surface of a Copper (Cu) single crystal substrate. Co on Cu (100) is an extensively studied and well characterized system; Co grows epitaxially in the layer by layer mode on the Cu substrate [Gonzales 81], [Clarke 87], [Germar 88], [Miguel 89], [Li H. 90]. In this system Cobalt is stabilized in the fcc structure (of the Cu substrate), which is stable for bulk systems only above 720 K. At lower temperatures, bulk Co is stable in the hcp structure.

The measurements were done by spin- and angle resolved photoemission spectroscopy with linear polarized and monochromatized synchrotron radiation at the electron storage ring BESSY, Berlin. We used photon energies in the VUV (vacuum ultraviolet) range (about 10-200 eV photon energy). The samples have further been characterized by Auger-spectroscopy and low energy electron diffraction (LEED). Additionally spin resolved bandstructure calculations for the thickness dependence of the electronic structure of the Co films have been performed with the FLAPW (Full Potential Linearized Augmented Plane Wave) method at the super computer CRAY, Jülich.

We discuss first the development from the two- to the three-dimensional electronic structure of Co films varying in thickness from the submonolayer regime up to 15 atomic layers. The experimental results are compared to calculations for 1 - 3 Co layers on Cu (100) and an 11 layer Co slab. For a bulk-like Co film (> 5 ML thickness) we determined experimentally the bandstructure in the Γ - X high-symmetry direction of the three dimensional Brillouin zone.

In the second part we report about the changes in the spin dependent electronic structure of the Co-valence band and of the Co 3p core levels induced by oxygen adsorption at room temperature and at 150 K.

2. Itinerant Magnetism

Magnetism is one of the oldest physical phenomena studied, but it continues to be an active and challenging subject. This is due to the fact that magnetic phenomena represent a complex application of quantum mechanics and statistical physics. As new magnetic materials are synthesized and new experimental conditions realized (like ultrathin magnetic films), the very fundamentals of these subjects are probed. We want to give here a short overview over the most important aspects of magnetism, especially of the magnetism of delocalized (itinerant) electrons in 3d metals. More detailed descriptions can be found for example in ref. [Nolting 86], [White 83] and [Erice 91].

2.1 Fundamentals

First we want to give the definitions of the magnetic moment, the magnetization and the magnetic susceptibility. The *magnetic moment* m is defined as

$$m = \partial E / \partial H \tag{2.1}$$

thus m is the change of the energy E of the magnetic system induced by the change of the external magnetic field H. The *magnetization* M is obtained by averaging the moments $\langle m \rangle$ over a region of space which is large enough to give such an average a meaning but smaller than spatial variations in the system, so M is defined as

$$M = N/V \cdot \langle m \rangle \ , \tag{2.2}$$

where N/V is the number of atoms per unit volume.

The *magnetic susceptibility* χ is a response function, which describes the magnetization as a function of an external field H. In general, χ is a tensor and is defined by the relation

$$M(r,t) = \iint dr'\, dt'\, \chi(r,r';t,t') \cdot H(r',t') \tag{2.3}$$

If the magnetic medium possesses translational invariance, is magnetized homogeneously and if one assumes a homogeneous, static field then

$$\chi_{\alpha\beta} = (\partial M_\alpha / \partial H_\beta)_T \qquad \alpha,\beta \in \{x,y,z\} \tag{2.4}$$

So χ depends in general on H and the temperature T.

Magnetic Ordering

There are roughly three different kinds of magnetic ordering:

a) *Diamagnetic* ordering is defined by

$$\chi^{dia} < 0 \; ; \; \chi^{dia} = \text{const.}$$

Here the external field H induces magnetic dipols that are aligned antiparallel to the external field according to Lenz's rule. Diamagnetism is a property of *all* materials, but it is relatively weak, so it can easily be covered by other forms of magnetism. (examples for diamagnetic materials: noble metals, non-metals, superconductors)

b) *Paramagnetism* is defined by

$$\chi^{para} > 0 \; ; \; \chi^{para} = \chi^{para}(T)$$

In paramagnetic materials, there are permanent magnetic dipols that are aligned by an external field H. This alignment is hindered by thermal movements. The permanent magnetic dipols can be due to localized moments caused by only partially filled atomic shells; this leads to Langevin-paramagnetism: $\chi^{Langevin} = \chi^{Langevin}(T)$ and to Curie´s law

$$\chi(T) = C/T \qquad (2.5)$$

at high temperatures. The permanent moments can also be itinerant moments of nearly free conduction electrons, that have a permanent moment of one Bohr magneton (μ_B). This causes the Pauli-Paramagnetism, where the susceptibility χ^{Pauli} is constant in the first approximation. Generally, $\chi^{Pauli} << \chi^{Langevin}$.

c) In *collective magnetism* the susceptibility is a complex function of the magnetic field, the temperature and often also of the 'history' of the sample:

$$\chi^{c} = \chi^{c}(H,T,\text{'history'})$$

It results from a quantum mechanical exchange interaction between permanent magnetic dipols. This leads to a critical temperature T^*, below which a spontaneous magnetization is observed. The permanent magnetic moments can again be localized (EuO, Gd, Rb_2MnC_{l4}, ...) or itinerant (Fe, Co, Ni, ...). Collective magnetism is mainly found in three different types:

i) In the case of *ferromagnetism* the critical temperature is the Curie-temperature T_C. For temperatures $0 < T < T_C$ the permanent moments have a preference direction and at $T = 0$ all moments are aligned.

ii) In *ferrimagnetic* materials, the lattice consists of two ferromagnetic sublattices A and B with different magnetizations $M_A \neq M_B$, where $M = M_A + M_B \neq 0$ for $T < T_C$.

iii) *Antiferromagnetism*; here the critical temperature is the Néel temperature T_N. It is a special case of ferrimagnetism, where $M_A = - M_B$ for $T < T_N$.

Magnetic Exchange Interactions

Materials with collective magnetism are marked by their spontaneous ordering of the magnetic moments below a critical temperature. The reason for the spontaneous ordering are the quantum mechanical exchange interactions that have many sources and forms; the most important types are:

- direct exchange, i.e. interaction due to direct overlap of the spin polarized wave function; examples: H_2-molecule, Fe, Co, Ni.

- indirect exchange, i.e. interaction due to the polarization of basically non-magnetic conduction electrons $\propto {}^1/_R \cdot \cos(2 k_F R)$ ($\rightarrow$ oscillatory!); examples: RKKY interaction, rare earth metals, magnetic impurities in noble metals.

- super exchange, i.e. indirect exchange in insulators due to the polarization of an anion (e.g. O^{2-}). This interaction is short ranged and strongly direction dependent; example: antiferromagnetic coupling in CoO.

2.2 Metallic Magnetism

We want to review the field of metallic (or itinerant) magnetism with particular emphasis on the 3d-transition metal series containing the 'classical' ferromagnetic metals iron, cobalt and nickel [Capellmann 86]. In the transition metals Cr, Mn, Fe, Co, Ni the electrons responsible for the magnetic properties in the ferromagnetically (Fe, Co, Ni) or antiferromagnetically (Cr, Mn) ordered phases participate in the Fermi surface. These electrons are

itinerant, their wave functions are delocalized, therefore no truly localized magnetic moments exist. The delocalized nature of the wave functions is due to the possibility of the electrons to move around rather freely in the crystal (free-hopping processes). It is this property, which distinguishes itinerant magnetism from the magnetism due to localized moments, such as in the insulating transition metal oxides and in rare earth metals. The magnetism in the localized systems can be discussed concentrating on the magnetic degrees of freedom alone, governed by some magnetic Hamiltonian (like a Heisenberg Hamiltonian).

This separation of the magnetic degrees of freedom from the translational degrees of freedom is not possible in itinerant systems. The relevant d electrons are delocalized: they can move freely through the crystal. The kinetic energy associated with this electron movement is characterized by the bandwidth W, which is of the order of 5 eV. This energy is much larger than the thermal energy $k_B T_c$ leading to a phase transition from the magnetically ordered to the paramagnetic state. To achieve an understanding of the magnetic properties, one has to deal with the full many-body problem incorporating magnetic and translational degrees of freedom of the electrons responsible for the magnetism. This is the reason why it took so long until even a qualitatively understanding of itinerant magnetism evolved. We discuss here shortly the jellium model and the Stoner model, that give a good qualitative describtion of ferromagnetism in metals.

Jellium Model with Spin Polarization.

In this model the ionic charges are homogeneously smeared out, i.e. the electron density is assumed to be constant (= n_o). The total electron energy is:

$$E_{tot} = N \cdot \left\{ \frac{3}{5} \frac{\hbar^2 k_F^2}{2m} - \frac{3}{4} \frac{e^2 k_F}{\pi} \right\} \qquad (2.6)$$

= kinetic energy (E_{kin}) - exchange energy (E_x)

with N = total number of electrons, $\hbar$ = Planck´s constant,

m = electron mass and $k_F = (3\pi^2 n_o)^{1/3}$.

Therefore magnetism in solids depends on the balance between increase of kinetic energy because of delocalization and gain of exchange energy, so magnetism in solids depends on the degree of localization of the electron wave functions;

completely delocalized : not magnetic

localized : magnetic.

The jellium model is qualitatively correct, but it fails quantitatively, i.e. it overestimates the tendency for magnetism. For the description of the ferromagnetism in transition metals, it is better to use the

Stoner Model for 3d Ferromagnetism.

Here the effective one-particle Hamiltonian for spin direction ↑ is $H^{\uparrow} = H_0 - {}^1/_2\, I\, M$ (majority electrons) and for spin direction ↓ $H^{\downarrow} = H_0 + {}^1/_2\, I\, M$ (minority electrons) where H_0 is the Hamiltonian in the paramagnetic state, M is the local magnetic moment and I the exchange integral ($I \approx 0.7$ eV/μ_B). Now there are two bandstructures (and densities of states) for majority and minority electrons, shifted in energy by $\Delta E = \pm {}^1/_2\, I\, M$, related to the value in the paramagnetic state, where the minority bands (states) are shifted to higher energy. The energy difference between the majority and minority bands is the exchange splitting.

The *Stoner criterion* for ferromagnetism predicts that a system is ferromagnetic, if the density of states at the Fermi energy in the paramagnetic state (n_0) times the exchange integral (I),

$$n_0(E_F) \cdot I \geq 1 \ , \qquad (2.7)$$

else it is paramagnetic. The value of $n_0(E_F)$ depends strongly on the bandwidth W with $W^2 = Z_{nn}\, a^2$ (Z_{nn} is the number of nearest neighbors and a the hopping matrix element), a narrowing of W leads to an enhancement of $n_0(E_F)$.

For transition metals one can find general trends for the properties which are relevant for magnetism, like the value of the exchange integral I, the bandwidth W, and also the behavior at surfaces and monolayer systems:

Trends for transition metals:

i) $I_{3d} > I_{4d} > I_{5d}$

ii) in each series there is a strong contraction of W with increasing atomic number, therefore only Fe, Co and Ni are ferromagnets, Pd is nearly so.

iii) at surfaces or in monolayer systems Z_{nn} is reduced. This leads to band narrowing and therefore to an enhancement of the surface magnetic moment or magnetism in materials that do not display bulk magnetic behavior.

For the "classical" ferromagnets Fe, Co and Ni we want to give in table 2.1 some important magnetic and structural properties in an overview:

	atom		crystal		
	electron. config.	m (μ_B/atom)	lattice	m (μ_B/atom)	T_c (K)
Fe	[Ar] $4s^2 3d^6$	4	bcc	2.22	1043
Co	[Ar] $4s^2 3d^7$	3	hcp/fcc	1.72	1388
Ni	[Ar] $4s^2 3d^8$	2	fcc	0.61	627

Table 2.1: magnetic properties in the atoms and crystals of Fe, Co and Ni, taken from ref. [Kittel].

3. Photoelectron Spectroscopy

Among the various probes for surfaces electrons as the carriers of the specific information have found by far the widest application for a number of reasons:

1. Electrons have an inelastic mean free path of a few Å depending on the energy (see fig. 3.1 and ref. [Seah 79], [Zangwill 88], [Ebel 90]). Energy and momentum of an electron are therefore characteristic of elementary excitations near the surface.

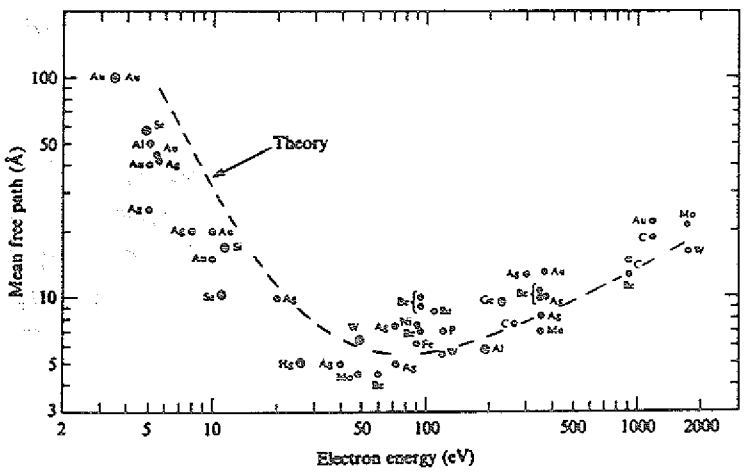

Fig. 3.1: "Universal curve" of electron mean free path, after ref. [Zangwill 88].

2. Electrons are easily focused into beams and the energy may be varied by applying appropriate potentials.

3. Electrons are efficiently detected and counted.

4. Electrons may be analyzed with respect to angular and energy distribution using electrostatic lenses and deflection systems.

5. The spin of the electrons can also be analyzed (see chapter 3.2). Therefore one can additionally get information about the magnetic properties of the sample.

Photoelectron spectroscopy is an experimental technique that measures the kinetic energy of an emitted electron following the absorption of a photon. If an electron is to be photoemitted, the energy of the incident light must be larger than the ionization potential of an atom or molecule, or the work function of a solid (which is in the range of some eV). Therefore ultraviolet to X-ray light sources are commonly used. Because of the surface sensitivity in VUV-(Vacuum Ultraviolett) photoemission (10 - 200 eV photon energy) the electronic properties both of the surface and bulk can be studied as well as of ultrathin films and of interface systems. For a given energy of the incident light (hν), the peaks in the kinetic energy distribution of the emitted electrons (energy distribution

curve: EDC) reflect the nature of the quantum states of the system being studied.

3.1 Angle Resolved Photoemission Spectroscopy (ARPES)

Conventional angle-integrated photoelectron spectroscopy measures the energy and intensity of the peaks in the spectra as a function of the electronic structure of the sample. Angle resolved detection adds a new dimension to photoelectron spectroscopy. The intensity and energy dependence can be measured as a function of the collection angle with respect to the crystallographic direction. Review articles about angle resolved photoemission spectroscopy one can find in ref. [Cardona 79], [Thiry 80], [Plummer 82], [Himpsel 83], [Davis 86].

Angle resolved photoemission is even more powerful when polarized radiation is used in systems with a high degree of symmetry. For example the emission intensity from a single crystal low index surface is measured with respect to the photon energy ($h\nu$), the direction of the polarization of the light (defined by the vector potential $\mathbf{A}$), the incidence angle of the light (α) and the emission angle of the photoelectrons (Θ), see fig. 3.2.

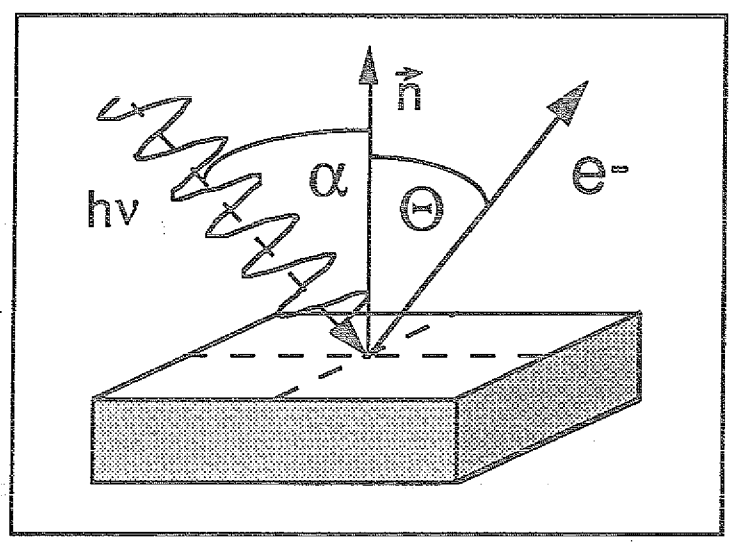

Fig. 3.2: Photoemission geometry.

The Photoionization Process.

The transition probability per unit time between two eigenfunctions of the same Hamiltonian H_o denoted by $|\Psi_i\rangle$ and $\langle\Psi_f|$ is given by Fermi's golden rule, if the perturbation H' is small.

$$\frac{d\omega}{dt} = \frac{2\pi}{\hbar} \cdot |\langle\psi_f| H' |\psi_i\rangle|^2 \cdot \{\delta(E_f - E_i - h\nu)\} \qquad (3.1)$$

The perturbation to the system caused by the incident radiation is found by replacing the momentum operator $\mathbb{P}$ by $\mathbb{P} + (e/c)\,\mathbb{A}$, in the original Hamiltonian H_0. So that the full Hamiltonian H is

$$H = H_0 + \frac{e}{2mc}(\mathbb{A}\cdot\mathbb{P} + \mathbb{P}\cdot\mathbb{A}) - e\,\Phi + \frac{e^2}{2mc^2}\cdot|\mathbb{A}|^2 \qquad (3.2)$$

where $\mathbb{A}$ and Φ are the vector and scalar potentials of the incident light field. The diamagnetic term $|\mathbb{A}|^2$ is always small and is neglected now. It is always possible to choose a gauge where $\Phi = 0$. The differential photoionization cross-section can then be written as:

$$\frac{d\sigma}{d\Omega} \propto |\langle\psi_f|\,\mathbb{A}\cdot\mathbb{P} + \mathbb{P}\cdot\mathbb{A}\,|\psi_i\rangle|^2\cdot\{\delta(E_f - E_i - h\nu)\} \qquad (3.3)$$

The differential cross section can be simplified by using the commutator $[\mathbb{P},\mathbb{A}] = -\,h\,\nabla\cdot\mathbb{A}$. The term $\nabla\cdot\mathbb{A}$ is usually assumed to be small or zero. However at the surface this is not generally justified. The wavelength of the light is so large compared to the atomic dimensions, that we can treat $\mathbb{A}$ as a constant. The momentum of the photon is ignored, which is a good approximation below photon energies of about 10 keV. Now equation (3.3) becomes

$$\frac{d\sigma}{d\Omega} \propto |\langle\psi_f|\,\mathbb{P}\,|\psi_i\rangle\cdot\mathbb{A}_o|^2\cdot\,\delta(E_f - E_i - h\nu) \qquad (3.4a)$$

This 'electric dipole' matrix element can be converted into two alternate forms by using the commutation relation of H_0 with $\mathbb{P}$ and $\mathbb{r}$, yielding

$$\frac{d\sigma}{d\Omega} \propto |\langle\psi_f|\,\mathbb{r}\,|\psi_i\rangle\cdot\mathbb{A}_o|^2\cdot\,\delta(E_f - E_i - h\nu) \qquad (3.4b)$$

$$\frac{d\sigma}{d\Omega} \propto |\langle\psi_f|\,\nabla V\,|\psi_i\rangle\cdot\mathbb{A}_o|^2\cdot\,\delta(E_f - E_i - h\nu) \qquad (3.4c)$$

where V is the potential in H_0. Note that all forms of (3.4) are incomplete if $\nabla\cdot\mathbb{A} \neq 0$.

The wave function $\langle\Psi_f|$ in the golden rule matrix element describes an electron state which contains an outgoing plane wave with the energy E_f and the wave vector k_f of the photoelectron having amplitude 1. The initial state wave functions $|\Psi_i\rangle$ contributing to the golden rule matrix element are determined by energy conservation and momentum conservation in a periodic medium (for example, a single crystal):

$$E_i = E_f - h\nu, \qquad (3.5)$$

$$k_i^{\parallel} = k_f^{\parallel} - g^{\parallel}, \qquad (3.6)$$

($h\nu$ = photon energy, $k = p/\hbar$) where $g^{\parallel}$ is a reciprocal surface lattice vector. The second equation shows that $k^{\parallel}$ is conserved when it is reduced to the unit cell in $k^{\parallel}$ space, i.e. the surface Brillouin zone. The momentum of U.V. photons is negligible compared to the electron momentum. The momentum perpendicular to the surface $k^{\perp}$ is not conserved because the outgoing electron has to overcome the work function at the surface and the lack of periodicity allows any amount of momentum transfer perpendicular to the surface. Generally, a theoretical angle-resolved photoelectron spectrum consists of discrete δ functions which originate from bulk initial states with different k_i and from surface states. Experimental spectra are broadened by initial- and final-state-lifetime effects and phonon scattering, which are not included in this matrix element.

Experimental Determination of Bulk Energy Band Dispersions

Energy bands are used to describe many basic properties of solids, such as electrical conductivity, optical properties, magnetism and others. Theoretically, energy bands (E(k)) originate from a single particle ground state picture, which leads to the concept of Bloch states for a periodic crystal lattice. With angle resolved photoemission spectroscopy one is able to determine not only the energy and momentum (E_f,k_f) of the excited final state of the electron but also for the initial state (E_i,k_i) [Himpsel 80], [Thiry 80], [Plummer 82]. Energy and momentum conservation are given by equations (3.5) and (3.6). Thus the excitation of the photoelectron by the photon (with the energy $h\nu$) from the initial to the final state can be described as a vertical transition where k (in the reduced Brillouin zone) is conserved. This vertical transition is shown in fig. 3.3.

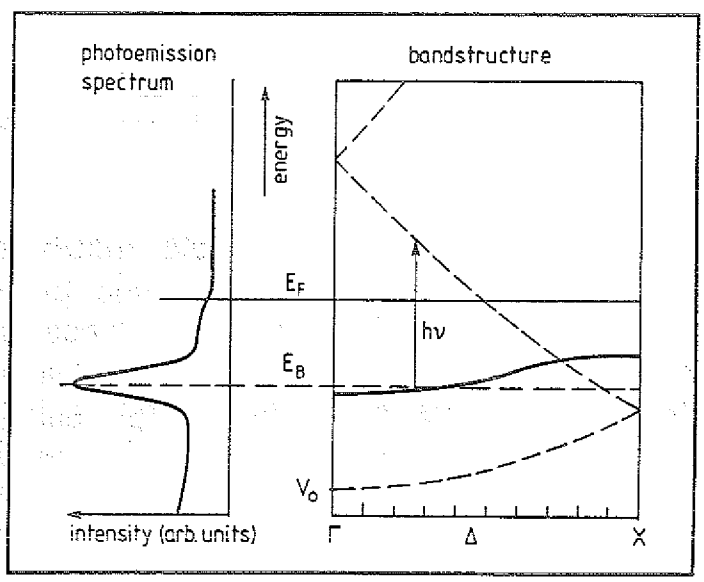

Fig. 3.3: Band structure determination with angle resolved photoemission

Measuring the kinetic energy E_{kin} of the photoelectrons we know their $|k|$ value by the dispersion relation

$$E_{kin} = \frac{\hbar^2 \cdot |k|^2}{2m} \tag{3.7}$$

By measuring also the emission angle Θ we get $k_{\parallel}$ inside (= $k_{\parallel}$ outside):

$$k^{\parallel} = \frac{1}{\hbar}\sqrt{2m\,E_{kin}} \cdot \sin\Theta \tag{3.8}$$

$$= 0.51\ \text{Å}^{-1} \cdot \sqrt{E_{kin}/\,eV} \cdot \sin\Theta$$

To determine the complete momentum vector directly from an angle resolved experiment, one has to find the momentum transfer perpendicular to the surface, as $k^{\perp}$ is not conserved. There are several approximative and exact methods to do this, we want to discuss here the approximation for the final state (E_f, k_f) as a parabolic free-electron-like band:

$$E_f(k_f) = \frac{\hbar^2 \cdot k_f^2}{2m} + V_o \qquad (V_o < 0) \tag{3.9}$$

Here m is the effective electron mass, which can normally be assumed to be 1 m_e (electron rest mass), and V_o is a constant inner potential (fig. 3.3).

This and the conservation of the energy (3.5) leads to

$$E_f = E_i + h\nu = \frac{\hbar^2 \cdot k^2}{2m} + V_o$$

$$\Rightarrow \qquad |k| = \left(\frac{1}{\hbar}\right)\sqrt{2m\,(E_i + h\nu - V_o)} \tag{3.10}$$

$$= 0.51\ \text{Å}^{-1} \cdot \sqrt{(E_i + h\nu - V_o)/eV}$$

Fixing Θ to a given value restricts k_f and k_i to certain curves in k space, which are given by

$$k_f^{\parallel} = 0.51\ \text{Å}^{-1} \cdot \sin\Theta \cdot \sqrt{(E_i + h\nu)/eV}\ \frac{k^{\parallel}}{|k|} + g^{\parallel} \tag{3.11a}$$

$$k_f^{\perp} = \sqrt{(E_i + h\nu - V_o)/3.84\ eV - k_f^{\parallel\,2}} \tag{3.11b}$$

If one restricts the experimental geometry to normal electron emission ($\Theta = 0 \rightarrow k^{\parallel} = 0$) from a low index single-crystal surface, the situation becomes even easier:

$$k^{\parallel} = 0,$$

$$k_i^{\perp} = 0.51\ \text{Å}^{-1} \cdot \sqrt{(E_i + h\nu - V_o)/eV}\ . \qquad (3.12)$$

The initial energy E_i can be obtained from the energy distribution curves (photoemission spectrum), when they are normalized to the Fermi energy E_F. In this case, E_i is the negative of the binding energy E_B of a peak in the photoemission spectrum: ($E_i = -E_B$), see also fig. 3.3. hν is again the photon energy. In equation 3.12 one sees that $k_i^{\perp}$ depends on the photon energy but also on the binding energy of the state. That means that different peaks at different binding energies in one photoemission spectrum correspond to emission from states at different k-points in the Brillouin zone.

The only unknown parameter in equation (3.12) is the constant inner potential V_o. This can be experimentally determined by taking a set of photoemission spectra in normal emission at different photon energies, where one follows the dispersion of one state in the spectra. For this it is necessary to have a light source, where the photon energy can be varied continuously over a wide range, like synchrotron radiation. By varying the photon energy, the spectra correspond to emission from states along a high symmetry direction of the Brillouin zone. For example at the (100) surface of a face centered cubic (fcc) crystal one follows the Γ - X direction, see fig. 3.4.

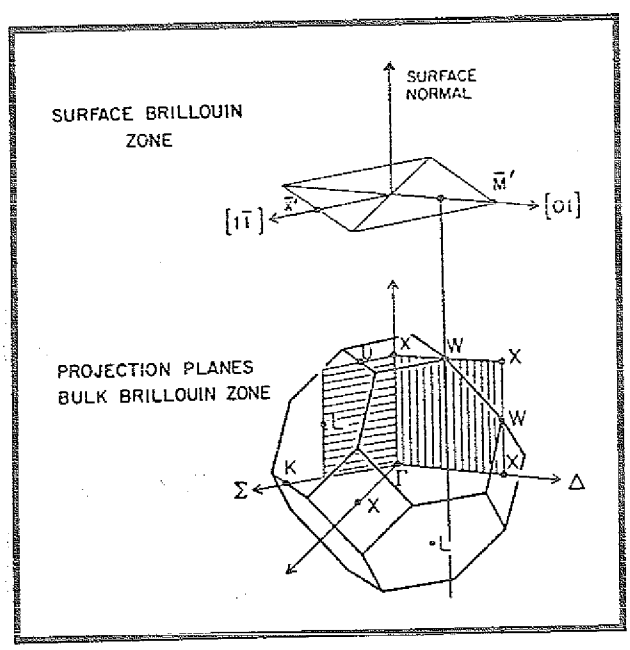

Fig. 3.4: (Top) Surface Brillouin zone and (bottom) bulk Brillouin zone of an fcc crystal with the surface normal in [100] direction [Plummer 82].

The states at high symmetry points like the Γ point in the Brillouin zone have an extremum in the binding energy E_B^*, that one sees in the photoemission spectra. At that particular photon energy $h\nu^*$, where the peak of a special state is at an extremum position in binding energy, the transition is likely to take place at a high symmetry point in the Brillouin zone, where $k_f^{\perp}$ is k_{BZ} (k vector of the first Brillouin zone) times an integral number n. This determination of a high symmetry point in the Brillouin zone is independent of any assumption. k_{BZ} is known from the lattice of the sample, the surface and the lattice constant (see for example ref. [Plummer 82]). Now one gets V_0 from

$$V_0 = E_B^* + h\nu^* - 3.84\ \text{eV}\cdot\left(n\cdot k_{BZ}/\text{Å}^{-1}\right)^2 \qquad (3.13)$$

V_0 is typically in the range of -5 to -10 eV.

As mentioned above, with ARPES one can study bulk properties as well as surface electronic properties (for instance the surface band structure of ordered adsorbates). They can be distinguished from each other by their different behavior in the energy distribution curves due to the chosen parameters:

Surfaces

The influence of the surface on the valence states of a crystal is twofold. First, bulk states are modified near the surface but remain periodic going towards infinity inside the crystal. Second, there also exist completely new states at the surface, called surface states. Surface states are states at the surface with an Energy E and $k_{\parallel}$ such that there are no states of the same symmetry in the bulk with the same values of E and $k_{\parallel}$, independent of $k^{\perp}$. This type of electronic state cannot mix with any bulk state. Surface states must lie in a bandgap in the projection of the bulk states onto the surface. The following rules apply for the identification of a peak in the angle-resolved photoemission spectrum as a surface state:

1. The energy E and parallel momentum $k_{\parallel}$ of the state must lie in a gap in the projection of the bulk band structure onto the surface Brillouin zone. These projections must consider the symmetry of the bulk states.

2. The initial state energy of the peak must be independent of the exciting photon energy for a fixed $k_{\parallel}$. If a peak moves in the

photoemission spectra as hν is changed in normal emission, then it is due to an initial state whose energy depends on $k^{\perp}$ (bulk state).

3. The peak should be (but does not always have to be) sensitive to the surface conditions like perfection and cleanliness.

Besides pure surface states there exist also surface resonances. These are electronic states at the surface that are modified bulk states.

Using polarized light (like linear or circular polarized synchrotron radiation) one can also select special electron wave functions by their symmetry. This one can reach by choosing the right experimental parameters for the sample geometry, the incoming light and the detection direction of the photoelectrons:

Symmetry and Selection Rules

Apart from energy and momentum there exist extra symmetry quantum numbers for electron wave functions in a crystal. The situation is easy with photoelectrons detected in planes of mirror symmetry perpendicular to the surface. The solutions of Schrödinger's equation with $\mathbf{k}$ in a mirror plane must be of odd or even parity under reflection. The final state wave function Ψ_f has even parity since it contains a plane wave with amplitude 1 approaching the detector. The photoemission intensity is given by the matrix element of the operator $\mathbf{A}\cdot\mathbf{P}$ in equation (3.4). The operator $\mathbf{A}\cdot\mathbf{P}$ is of even parity if the polarization vector $\mathbf{A}$ is parallel to the mirror plane and odd if $\mathbf{A}$ is perpendicular to the mirror plane. A non-zero matrix element is therefore obtained with either $\mathbf{A}$ perpendicular and Ψ_i odd, or $\mathbf{A}$ parallel and Ψ_i even.

Linear polarization of the light is characterized by a fixed polarization direction (defined by the vector potential $\mathbf{A}$), that is perpendicular to the propagation direction. In this case one achieves $\mathbf{A}$ perpendicular to the surface normal (s-polarized light) for example by normal incidence of the light ($\alpha = 0$, see fig. 3.2). P-polarized light requires a polarization vector $\mathbf{A}$ parallel to the surface normal, which can only be achieved by off-normal incidence.

For wave functions with higher symmetry at special points in momentum space one has to take into consideration dipole selection rules. Table 3.1 shows these dipole selection rules, that are valid in the one electron picture, in the case of normal emission from low index surfaces [Hermanson 77]. Similar tables for the more general case of off-normal emission can be found in ref. [Eberhardt 80].

Crystal Face	Coordinate axes			Irreducible Representations	Initial Symmetries		
	x	y	z		A||x	A||y	A||z
(001)	<100>	<010>	<001>	$\Delta_1\ \Delta_1'\ \Delta_2\ \Delta_2'\ \Delta_5$	Δ_5	Δ_5	Δ_1
(110)	<001>	<1$\underline{1}$0>	<110>	$\Sigma_1\ \Sigma_2\ \Sigma_3\ \Sigma_4$	Σ_3	Σ_4	Σ_1
(111)	<$\underline{1}$10>	<$\underline{1}$ $\underline{1}$2>	<111>	$\Lambda_1\ \Lambda_2\ \Lambda_3$	Λ_3	Λ_3	Λ_1

Table 3.1: Dipole-allowed initial state symmetries for normal emission from low index faces of cubic crystals (after ref. [Hermanson 77]). For each face the directions of Cartesian coordinate axes are referred to the conventional cubic axes, and irreducible representations at $k_{\|} = 0$ are listed in single group notation. A is the vector potential of the light.

3.2 Spin- and Angle Resolved Photoemission Spectroscopy (SARPES)

Besides energy, momentum and symmetry, it takes one more quantum number to characterize fully an electron: the spin. In this chapter we review the technique of spin and angle resolved photoemission (SARPES) from ferromagnets [Kisker/Carbone], [Feder 85 (1)]. SARPES can give a detailed information on the spin-dependent electronic structure of the bulk and of the surface of a *ferromagnetic* system. The electronic structure of a ferromagnet is characterized by a spin-split density of states with an excess of electrons of one spin direction. They are referred to as "majority (↑)" electrons, those of opposite spins as "minority (↓)" electrons. As an example, Fig. 3.5 shows a calculated fcc Co band structure.

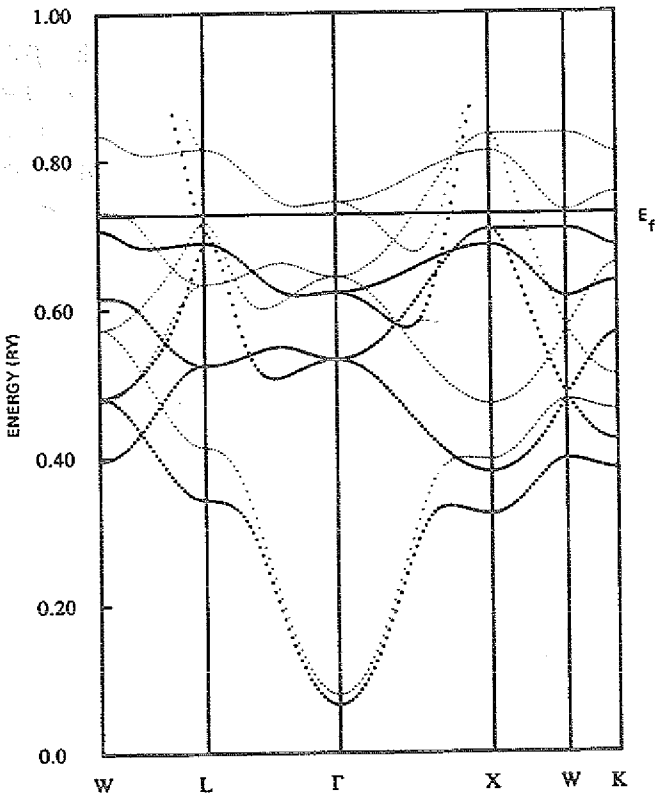

Fig.3.5: Calculated Band-structure of fcc Co along high-symmetry directions (after Moruzzi et.al. [Moruzzi 78]). Dark points indicate majority spin, light points for minority spin.

In the ferromagnetic state, bands for electrons with their magnetic moments parallel to the magnetization direction differ in energy from those of electrons with opposite magnetic moments. In an approximative description (e.g. in the Stoner model), the two sets of bands are of similar shapes, but are shifted in energy by the so-called exchange splitting. For Fe (Co, Ni), it is of the order of 2 (1.5, 0.3) eV. To identify experimentally the spin dependent electronic structure of magnetic materials, the spin information from the photoemitted electrons has to be determined.

For spin analysis either relativistic spin-orbit or quantum mechanical exchange interactions have to be used. The first of these methods has been most commonly applied and is called Mott scattering. Its physical principles are described in detail in ref. [Kessler 76]. Other spin detectors are described in ref. [Kirschner 85], [Tillmann 89]. The spin polarization P is defined as

$$P = (N^{\uparrow} - N^{\downarrow})/(N^{\uparrow} + N^{\downarrow}), \qquad (3.14)$$

where $N^{\uparrow,\downarrow}$ are the numbers of electrons with their magnetic moments parallel or antiparallel to the quantization (z-) axis. In so-called high-energy Mott scattering, a thin Au film is commonly used as target on which the primary beam, accelerated to about 100 keV, is scattered to determine its spin polarization. The asymmetry in the intensity of the electron beam backscattered at angles (Θ) of

typically ±120° (where the sensitivity is largest near 100 keV) is measured by a pair of surface barrier detectors. The spin polarization is obtained from the asymmetry by the relation

$$P = 1/S(d) \cdot A \,. \qquad (3.15)$$

Here S(d) is the effective Sherman factor, which depends on the thickness (d) of the scattering foil (because of multiple scattering), on the electron energy and on the scattering angle. It is largest for scattering nuclei with large atomic number Z. For d = 0, E = 120 keV and $\Theta = \pm 120°$, the Sherman factor has been calculated as S = 0.39; the value of S is typically between 0.2 and 0.3 for gold foils of about 1000 Å thickness.

The low intensity of the scattered beams is the problem which has restricted the application of spin analysis to a limited number of experiments so far. The beams scattered into the collection angles of the electron detectors amount typically to some 10^{-3} of the incoming electron beam.

When also the photoelectron spin is analyzed in photoemission, two energy distribution curves (EDC´s) are obtained for ferromagnets, one for the majority-spin electrons ($I^{\uparrow}(E_B)$), and a second one for the minority-spin electrons ($I^{\downarrow}(E_B)$). These two curves are referred to as the spin-resolved energy distribution curves. From the spin polarization curve $P(E_B)$ as calculated with the help of the determined asymmetry, together with the spin-integrated intensity curve $I_0(E_B)$ (that contains the sum of spin-up and spin-down electrons) the spin resolved energy distribution curves can be calculated as

$$I^{\uparrow,\downarrow}(E_B) = 0.5 \cdot I_0(E_B) \cdot (1 \pm P(E_B)) \qquad (3.16)$$

A specific problem in a spin- and angle-resolved photoemission experiment concerns the magnetization of the samples. The size of the light spot and of the analyzer acceptance area are typically larger than a single Weiss domain of a demagnetized sample. Accordingly, samples have to be magnetically saturated within the sampled surface area to avoid a trivial spin averaging due to electron emission from several macroscopic domains with different magnetization directions. One needs samples of suitable shapes such as a picture frame shaped crystal or thin single crystal plates or films that can be remanently magnetized in-plane. They remain magnetically saturated over a large enough surface area after the removal of the external magnetization field and they have nearly no

magnetic stray field which can influence the detection of the photoelectrons.

Besides the study of the spin split valence band structure, also the spin splittings in the core levels are of great interest for a detailed understanding of the electronic structure of solids. Multi-electron effects such as resonances and Auger processes also show often strong spin dependence [Landolt 89]. Near the core level excitation threshold resonant photoemission and resonant Auger emission are observed when the core electron is exited into a fairly localized unoccupied state. Spin effects have also been observed in these cases since the empty states of a ferromagnetic material are spin split by the exchange interaction.

4. Experimental Aspects

4.1 Experimental Conditions

The experiments have been performed at the 800 MeV electron storage ring BESSY in Berlin. Linear polarized synchrotron radiation in the VUV (vacuum ultraviolet light of about 10-200 eV photon energy) regime has been used as light source. The synchrotron light was monochromatized at the TGM1 (Toroidaler Gitter Monochromator) and TGM5 beamlines. The TGM1 beamline is connected to a bending magnet in the storage ring and one gets monochromatized light with photon energies of about 10 to 100 eV. The spin resolved spectra below 30 eV photon energy are taken at this beamline. The TGM5 beamline [Peatman 89] is connected to a Wiggler/Undulator inside the storage ring, which gives high photon flux even at higher photon energies. The spin resolved spectra above 30 eV photon energy are measured at this beamline.

The Photoelectron Spectrometer

The energy analyzer used for the spin and angle resolved photoemission spectroscopy is shown schematically in fig. 4.1.

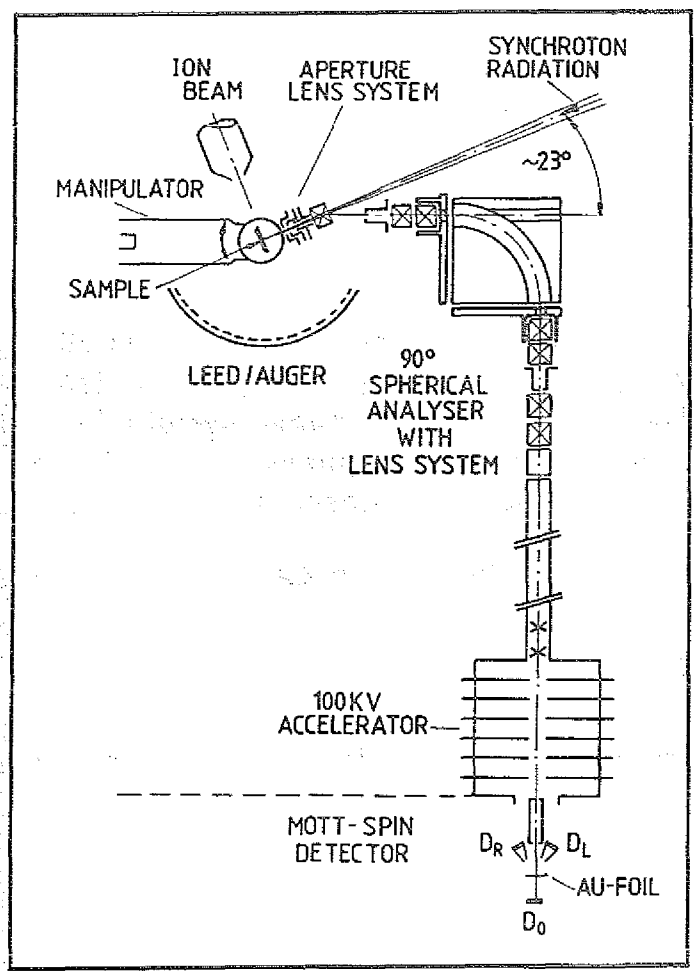

Fig. 4.1: Scheme of the energy analyzer for spin- and angle resolution

The energy analyzer consists mainly of two 90° spheres held at different potentials. An electron that passes through the electric field will be deflected; its path is fixed by means of apertures. One can choose the energy of the transmitted electrons - the pass energy - by varying the voltage between the spheres. A review of electrostatic analyzers can be found in ref. [Ibach 77]. In this work a 90° - spherical analyzer with an energy resolution of about 250 meV at an angular acceptance of ± 3° has been used [Kisker 85]. In this analyzer normal incidence of the light (thus s-polarization) at normal collection direction is realized by a pair of capacitor plates which deflect the electrons from the light axis. Off normal collection directions can be reached by tilting the angle of the sample. If the sample is turned around an axis parallel to the polarization vector, s-polarization will be preserved, otherwise the spectra are taken with mixed (s- and p-) polarization. The spin analysis is done by a 100 keV Mott-detector after the energy analysis.

Experimental Set-Up

Fig. 4.2 shows the experimental set-up at the TGM1 monochromator-beamline at the BESSY storage ring:

Background: concrete wall as protection against the radiation coming from the electron storage ring behind.

1. Beamline with monochromator TGM1

2. UHV - chamber. It contains the manipulator (3), a sputter gun, evaporators, an oscillating quartz thickness monitor, a leak valve for gas exposure, and a combined LEED/Auger system for sample preparation and characterization; a magnetization coil and the energy analyzer for photoemission spectroscopy.

3. Manipulator with sample holder. The sample can be moved, rotated, heated and cooled (with liquid nitrogen or helium).

4. 100 keV Mott - detector for spin analysis.

5. Rack with control units and computer for controlling the sample preparation and photoemission measurements.

6. Rack with control units for LEED and Auger spectroscopy.

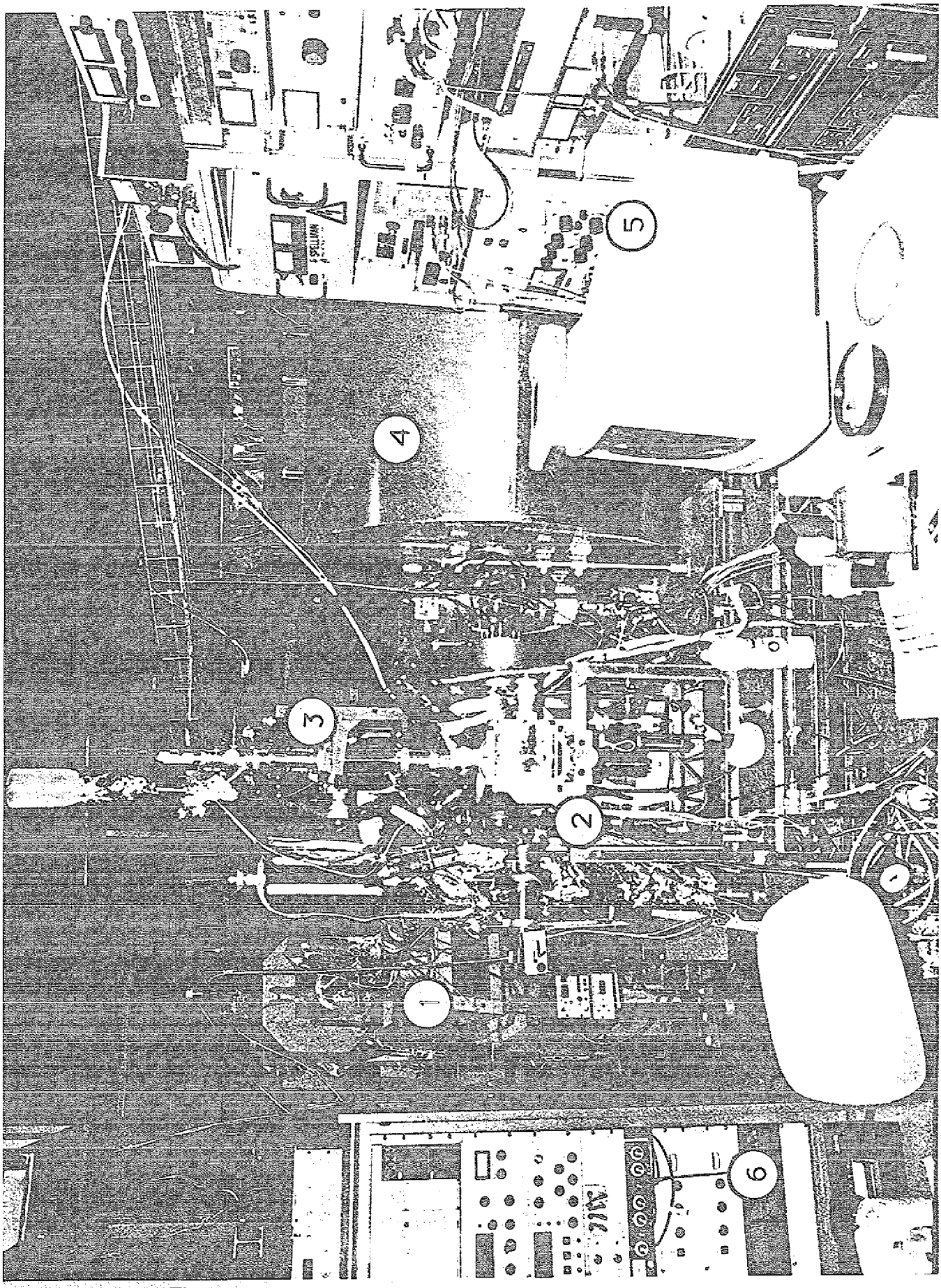

Fig. 4.2: Experimental set-up at the TGM1-beamline at BESSY

4.2 Sample Preparation and Characterization Methods

Sample Preparation

The Co films investigated in this work have been evaporated on the (100) surface of a Copper single crystal. To achieve a clean and well ordered substrate surface, the Copper crystal has been prepared in ultrahigh vacuum by cyclic Ar^+ - sputtering at 650 eV and heating. This procedure has been continued several times, until there was no more contamination detectable with Auger-spectroscopy and the LEED patterns showed sharp spots. Before each evaporation of Co, the Cu substrate has been sputtered and heated up to 700 K for 2 min to have a clean and well ordered surface. Cobalt was then evaporated on the surface after the crystal was cooled down to room temperature.

We evaporated Co at room temperature to avoid thermal diffusion of cobalt and copper which was found at temperatures above 410 K [Arnott 89]; whereas at lower temperatures, no interdiffusion was found. Co was evaporated by electron beam heating from a high purity wire at a rate of typically 0.5 atomic layers/min with the evaporating facilities surrounded by water-cooled jackets to prevent contamination by thermal desorption. The pressure in the UHV system raised during Co evaporation to 5 10^{-10} mbar, while the base pressure was 1.5 10^{-10} mbar. The coverage calibration has been performed with an oscillating quartz thickness monitor and with Auger-Electron-Spectroscopy (AES). The growth mode and surface quality of the sample have been characterized in detail by AES and Low Energy Electron Diffraction (LEED).

The angle and spin resolved photoemission spectra have been measured with the spherical energy analyzer coupled to a 100 keV Mott polarimeter (as discussed above). The Co overlayers were remanently magnetized by applying a short magnetic pulse in the direction of the in plane <110> easy magnetization axis, which was aligned to the spin sensitive direction of the Mott detector.

To study the influence of gas adsorbates on the electronic structure of the Co film, it is necessary to have well defined gas exposure conditions. Gas exposure is measured in units of 1 Langmuir (L) = 10^{-6} Torr·sec (= $1.3 \cdot 10^{-6}$ mbar·sec). If the gas has a sticking coefficient s = 1 the exposure of 1 L corresponds to the building of one layer of adsorbed gas on the sample surface. The exposure of oxygen into the UHV system has been controlled by a leak valve. The partial pressure of oxygen during the exposure normally was 1 10^{-7} mbar, thus exposure of 1 L corresponds to an exposure time of 13 sec.

Characterization Methods

LEED: The method of low energy electron diffraction (LEED) is a tool for studying the atomic structure and degree of order within a surface region of limited depth. Because of the wave nature of matter (with the de Broglie wavelength $\lambda=h/mv$; m = electron mass, v = velocity) electrons that are scattered elastically at a periodic lattice show interference effects. Those electrons that interfere constructively form a structure on a fluorescent screen which represents the reciprocal lattice of the surface. Therefore one can identify the structure of the surface lattice and also its quality by the symmetry and sharpness of the spots. Reconstructions as well as the arrangement of adsorbates can be determined. In this work a four-grid LEED system (as indicated in fig. 4.1) was used. Its compact electron gun generates monoenergetic electrons of energies up to 1 kV. Two outer grids of the analyzer are grounded, the inner grids are connected to a negative potential of about the same magnitude as the accelerating voltage in the electron gun. This potential decelerates the inelastically scattered electrons and thus prevents them from reaching the fluorescent screen.

Auger-Electron-Spectroscopy (AES): If a core level in an atom or a solid is ionized (by irradiation with electrons or photons) holes are created in core levels (X). Following the creation of this hole, the atom relaxes by filling the hole via a transition from an outer level (Y). As a result of that transition the energy difference between the outer and the core level E_X-E_Y becomes available. This excess energy can be used by the atom in either of two ways. It can appear as a characteristic X-ray photon at that energy or it can be given to another electron either in the same level or in a more shallow level Z, whereupon the second electron (the Auger electron) is ejected with a fixed energy [Briggs 83]. The first process is that of X-ray fluorescence, the second that of Auger emission. The three energy levels X,Y,Z reflect the common notation XYZ for Auger electrons, e.g. KLL, LMM emission. Because the energies of the Auger electrons are characteristic of each atom, and the inelastic mean free path of the electrons is in the range of some atomic layers (see chapter 3) Auger electron spectroscopy (AES) is used for element specific surface analysis. An Auger spectrometer on the basis of a LEED system works as a retarding field analyzer (RFA), where a decelerating potential in front of the collector holds back those electrons whose kinetic energy is less than the pass energy. The LEED-RFA used in this work consists of four grids, which are arranged concentrically in front of the LEED screen, which serves as a collector. The inner grids are both connected to the decelerating potential in order to diminish the field

penetration of the single grid. The outer grids are grounded in order to keep the area in front of the sample fieldfree and to screen the collector from modulation on the grids. Because all electrons with higher energy can overcome the potential barrier, the retarding field analyzer is a high-pass filter. Thus a first differentiation of the current on the collector in the lock-in amplifier yields the energy distribution curve (A) and a successive differentiation yields its derivative (B). In spectrum B the peak-to-peak heights are proportional to the intensities, i.e. the areas underneath the peaks in spectrum A.

Growth Modes

Depending on the interaction between substrate-atoms and adsorbate-atoms one can mainly distinguish three different growth modes:

a) In the layer by layer growth (Frank - v.d. Merwe (FM)) mode the interaction between substrate and adsorbate atoms is stronger than between two adsorbate atoms. The next layer starts to grow only after the previous layer is finished.

b) In the Stranski Krastanov - growth mode (SK) the first (or several) monolayer (ML) grows in the FM mode. On top of this complete layer the formation of 3 dimensional islands starts.

c) If the interaction between two adsorbate atoms is stronger than between adsorbate and substrate atoms, then the adsorbate grows as islands from the beginning on (Vollmer-Weber (VM) mode).

In real systems all of these growth modes exist. One possibility to distinguish between these modes is the analysis of the growth with Auger spectroscopy depending on the thickness of the overlayer. The intensity of the substrate and adsorbate emission has a different behavior with increasing adsorbate thickness in each growth mode [Kern 79]. The rel. changing of the AES intensity $\Delta I/I$ can be used in this analysis. In the case of the layer by layer growth mode, $\Delta I/I$ depends on the changing of the adsorbate thickness Δh as following:

$$\frac{\Delta I}{I} = -\frac{\Delta h}{\lambda} \qquad (4.1)$$

where λ is the inelastically mean free path of the electrons. Now we get for the intensity of the adsorbate signal $I_A(h)$:

$$I_A(h) = I_A^o \cdot \left(1 - \exp\left(-\frac{h}{\lambda_A}\right)\right) \qquad (4.2)$$

with I_A^o = AES intensity of the massive adsorbate material, h the adsorbate film thickness, and λ_A the inelastically mean free path of the adsorbate electrons.

For the substrate signal I_S (h)we get:

$$I_S(h) = I_S^o \cdot \exp\left(-\frac{h}{\lambda_S}\right) \qquad (4.3)$$

with I_S^o = AES intensity of the clean substrate and λ_S the inelastically mean free path of the substrate electrons.

During the creation of the first adsorbate monolayer (ML), the AES signal grows linear with the adsorbate coverage (h). During the creation of the next ML the AES signal also grows linear with the adsorbate coverage, but with a smaller ascent (because of the extinction of the signal in the previous layers). Therefore one can identify the completion of an adsorbate monolayer as a kink in the AES signal plotted as a function of the adsorbate thickness.

5. Results from clean surfaces

The spin dependent electronic structure of epitaxial Co overlayers on Cu (100) has been studied by spin- and angle resolved photoemission with linear polarized synchrotron radiation. The experimental results are supported by FLAPW calculations for 1 - 3 Co layers on Cu (100) and for an 11 layer Co slab.

5.1 Characterization of the Co/Cu(100) System

Cobalt occurs in two crystalline forms, hexagonal-close-packed (hcp) α-Co and face-centered cubic (fcc) β-Co. Both forms are ferromagnetic. The lattice constants for the hcp phase are a = 2.51 Å and c = 4.07 Å and for the fcc phase a = 3.54 Å. The stable crystallographic phase of Cobalt from about 720 K to beyond the Curie temperature at 1,388 K, is the fcc phase, while the hcp phase is stable at lower temperatures.

To get single crystals of high purity and quality, as they are needed for angle resolved photoemission, it is necessary to heat them up to some hundred °C [Musket 82]. For Cobalt this is difficult because of the phase transition. Therefore studies of Co single crystals in the hcp and fcc phase have mainly been restricted to works on recrystallized samples with a rather limited crystalline quality. One way out of this problem is to grow epitaxial overlayers of Co on an fcc substrate. In this way one achieves single crystal surfaces of high quality. Thus one can also study the properties of thin Co films and their developments with increasing thickness.

Co on Cu(100) is an extensively studied and well characterized system. Co grows epitaxially on Cu(100), in the layer by layer (Frank v.d. Merwe (FM)) mode [Gonzales 81], [Clarke 87], [Germar 88], [Miguel 89], [Li H. 90], even for Co thicknesses up to 20 ML. There is no interdiffusion of Co and Cu up to an substrate temperature of about 410 K [Arnott 89]. The Curie temperature for thin Co films is found to be significantly lower than the bulk value and to show a strong dependence on the overlayer thickness [Miguel 89], [Mankey 90]. At room temperature, there is a contradictory result, at which coverage Co starts to be ferromagnetic. Beier et al. [Beier 88] find ferromagnetism already in one monolayer of Co (in the same group there was also observed no variation of the magnetization as a function of temperature up to 400 K [Pescia 87]). On the other hand, Schneider et al. [Miguel 89], [Schneider 90 (1)] observe the onset of ferromagnetism at room temperature at about 2 ML coverage, and Mankey et al. report similar results [Mankey 90]. In all studies the magnetization of the Co layers was found to be in the plane of the

film [Pescia 87], [Schneider 90 (1)] and the easy magnetization axis is the <110> direction [Kerkmann 89], [Oepen 90]. Only in ultrathin Co films sandwiched by Au Chappert and Bruno [Chappert 88] find magnetization perpendicular to the film plane for Co thicknesses lower than 11 Å.

The Cu (100) Surface

In fig. 5.1 we show the spin integrated photoemission spectra of the clean Cu (100) surface taken in normal electron emission for different photon energies from 11 to 45 eV.

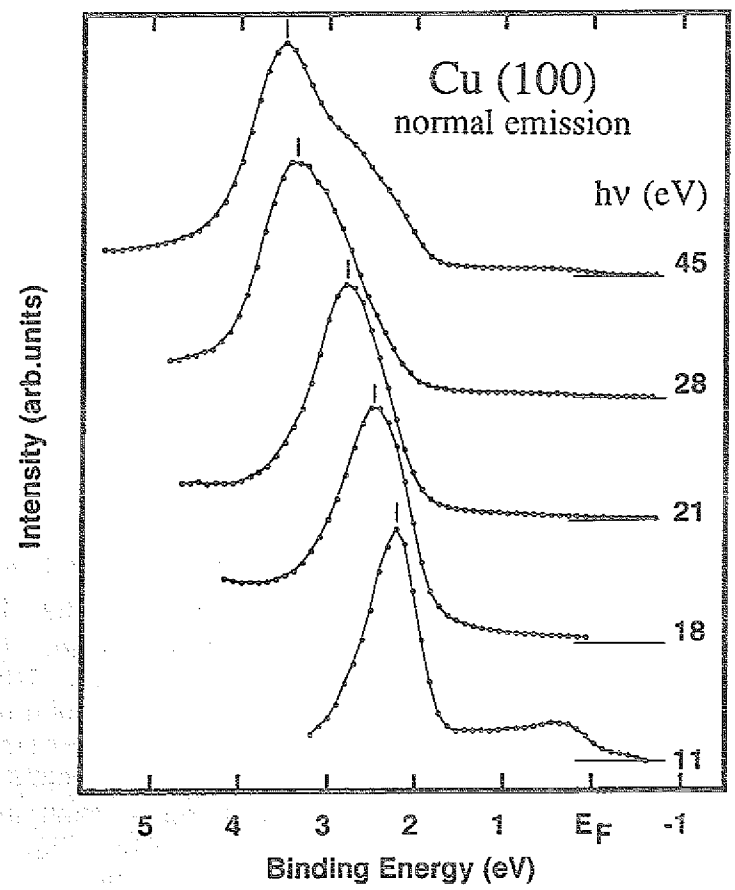

Fig. 5.1: Spin integrated energy distribution curves of Cu (100) taken in normal electron emission with s-polarized light of different photon energies.

The spectra mainly show one strong peak each. Their maxima shift from 2.2 eV to 3.5 eV binding energies with increasing photon energies. By excitation with s - polarized light (A perpendicular to the surface normal) we can detect only states of Δ_5 symmetry, see table 3.1. Varying the photon energy in normal electron emission we can observe states from k points of the Γ - X high symmetry direction of the Brillouin zone, see fig. 3.4. A calculation of this part of the Cu bandstructure [Burdick 63] is shown in fig. 5.2 (solid lines). Here one can see that there is only one band with Δ_5 symmetry, so

the peak in the clean Cu spectra is due to this Δ_5 band. Emission from the Γ - point ($k = 0$ or $2 \cdot k_{BZ}$) was found in normal emission to occur at a photon energy of $h\nu = 45$ eV with a binding energy of the Δ_5 peak of 3.5 eV. By assuming a free electron parabola with an electron mass of $m = m_e$ we get an inner potential of - 5 eV (see chapt. 3). With these final states we determined the band with the help of the spectra of figure 5.1. These points are shown as dots (●) in fig. 5.2, they fit very well to the calculated band structure, just like in previous work of Thiry [Thiry 81].

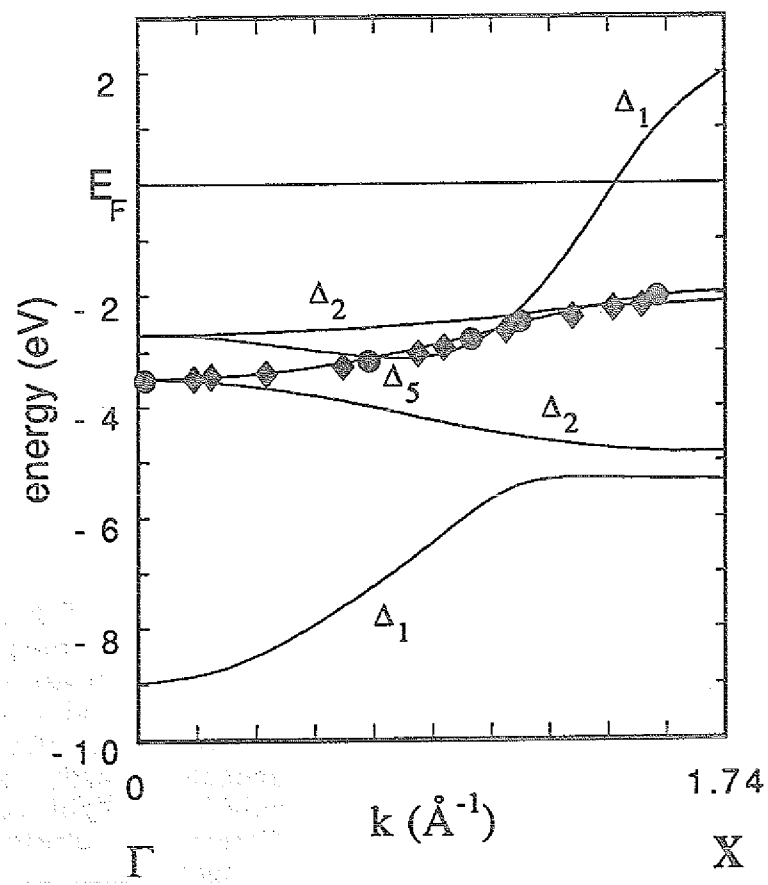

Fig. 5.2: Band structure of Cu in the Γ - X direction after Burdick [Burdick 63]. The dots (●) and diamonds (◆) show experimental determined points of the Δ_5 band taken from fig. 5.1 and fig. 5.13, respectively.

The diamonds (◆) show experimental points from the dispersion of a Cu (100) sample covered with 8 ML Co, see fig. 5.13. Here we also determined that emission from the Γ-point of the Brillouin zone corresponds to a photon energy of 45 eV. Also these points fit very well to the band structure. The spectra in fig. 5.1 do not all consist only of one strong peak. There is also a shoulder visible at about 2.5 eV binding energy in the spectrum for 28 and 45 eV photon energy. We interpret this shoulder to be attributed to Umklapp processes involving transition from the flat Δ_5 band near the X -point.

Co Overlayers on Cu (100)

Epitaxial Co overlayers have been prepared in situ on a Cu(100) single crystal as discussed in chapter 4.

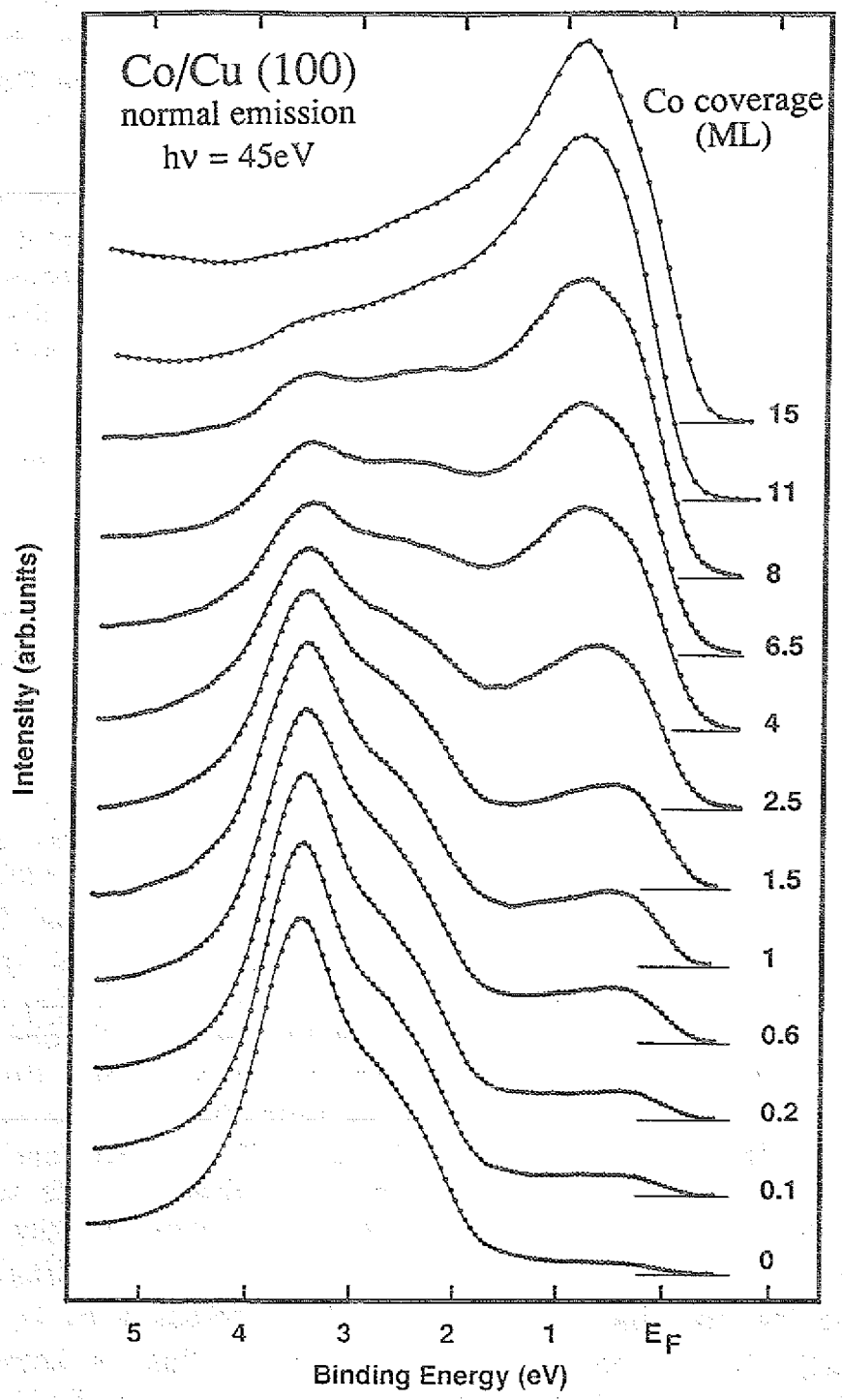

Fig. 5.3: Spin integrated energy distribution curves of Cu (100) with Co overlayers up to 15 monolayers (ML) thickness. The spectra are taken in normal electron emission with s-polarized light of 45 eV photon energy.

In fig. 5.3 we show the changes in the photoemission spectra due to Cobalt overlayers on the Cu (100) surface. The spectra are taken at normal electron emission with a photon energy of 45 eV. The bottom most spectrum is taken from the clean Cu (100) surface. It shows a strong peak at 3.5 eV binding energy coming from emission from the Δ_5 band at the Γ - point. The spectrum changes due to evaporation of Co. The spectra for Co evaporation from the submonolayer regime up to 15 ML thickness are shown. The Co derived features grow within 3 eV binding energy, the strongest structure grows in the region below 1 eV binding energy, but also in the region between 2 and 3 eV a shoulder is visible due to Co. The emission coming from the Cu substrate is suppressed more and more with the Co coverage due to inelastic scattering of the photoelectrons through the overlayer. The spectrum for 15 ML Co coverage shows the bulk Co emission, where almost no more emission from the Cu substrate is seen.

To test the epitaxial growth of Co we studied the surface ordering by low energy electron diffraction (LEED). In fig. 6.7 one can see the LEED-pattern of the clean Cu (100) substrate (see also the text to this figure in chapt. 6). It shows four sharp spots building a square that represents the surface Brillouin zone. After evaporation of 5 ML Co the pattern does not change. This shows, that the Co covered surface has exactly the same structure as the substrate surface, indicating an epitaxial growth of Co.

Whether the adsorbate grows in the layer by layer or in island growth, we checked by different methods. In the first case we determined the peak to peak intensities of the Co and Cu LMM Auger-peaks in the derivative (dN/dE) Auger spectrum. The typical Co peaks are at 656, 716 and 775 eV binding energy, while the typical Cu peaks are at 776, 845 and 920 eV electron energy. Because of the overlap of the 775/776 eV peak, we took the sum of the 656 and 716 eV peaks for the Co (I_{Co}) and the 920 eV peak for the Cu intensity (I_{Cu}). Fig. 5.4 presents the Co intensity normalized to the sum of Co and Cu ($R = I_{Co}/(I_{Co} + I_{Cu})$) as a function of Co coverage (ML). As discussed in chapter 4, in the layer by layer growth mode we expect the intensity of the substrate I_S to decrease exponentially with the completion of each adsorbate layer h by $I_S = I_S^0 \cdot \exp(-h/\lambda_S)$. On the other hand the adsorbate intensity I_A ($= I_{Co}$) increases by $I_A = I_A^0 \cdot (1 - \exp(-h/\lambda_A))$. By plotting the ratio of the intensities as shown in fig. 5.4, one cannot expect kinks at the completion of each layer (because the ratio of two linear curves is not a linear curve); but one is able to identify the growth mode over a wide thickness range.

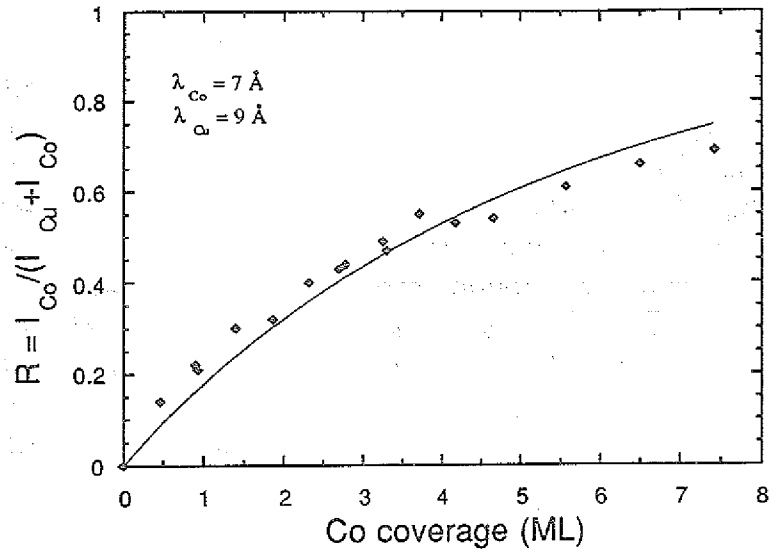

Fig. 5.4: ratio of the Cobalt to Copper peak to peak intensities in the derivative AES - Spectra $R = I_{Co}/(I_{Co} + I_{Cu})$ a function of Co thickness (dots) compared to the expected curve for the layer by layer growth mode

The solid curve in fig. 5.5 shows the expected curve according to the layer by layer growth. We found the best fit with $\lambda_A = \lambda_{Co} = 7\pm1$ Å and $\lambda_S = \lambda_{Cu} = 9\pm1$ Å. These values fit very well to the empirically determined curve for the inelastically mean free path (chapter 3) and also for theoretical calculations [Ebel 90], which is a proof for the layer by layer growth mode of this system.

Another independent test for the layer by layer growth is shown in fig. 5.6, which shows the emission in the photoemission spectra presented in fig. 5.4 normalized to the sum of the Co and Cu emission $R = I_{Co}/(I_{Co} + I_{Cu})$:

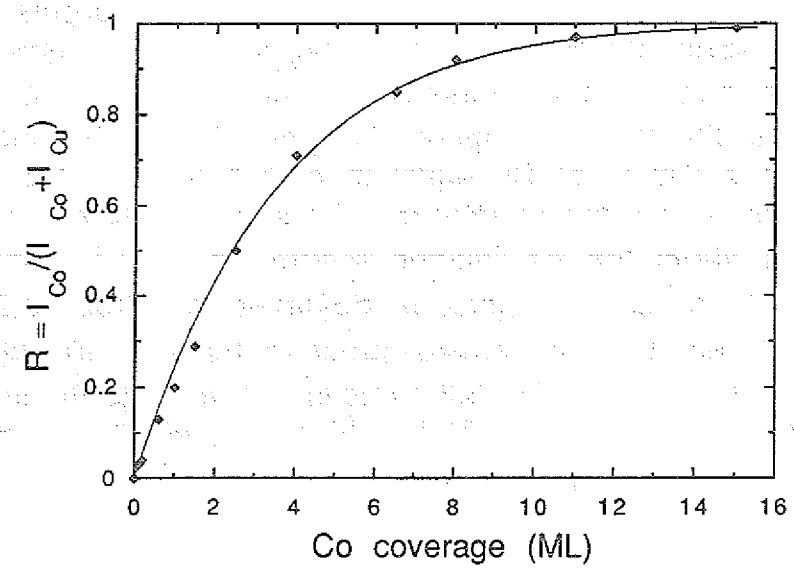

Fig. 5.5: Intensity of the Co emission in the photoemission spectra of fig.5.3 normalized to the sum of the Co and Cu emission plotted as a function of Co thickness

For Co the intensity of the emission at 0.9 eV binding energy has been used (I_{Co}) and for the Cu intensity at 3.5 eV binding energy after subtracting the background of inelastically scattered electrons. The dots in fig. 5.5 show the experimental points taken from the spectra of fig. 5.3. The solid line shows the expected curve for the layer by layer growth by using the same model as for the Auger study, because the Photoemission is also surface sensitive due to the emitted electrons, only the inelastically mean free paths of the photo electrons is different from the Auger electrons because of their different kinetic energies. We obtain the best fit of the curve with $\lambda_A = \lambda_S = 5 \pm 1$ Å, which are again reasonable values, compared to a general empirical curve for the inelastically mean free path, see chapter 3 and ref. [Seah 79]; this is another proof for the layer by layer growth. So we have verified the epitaxial and layer by layer growth of the Co overlayers on the Cu (100) substrate.

Now we want to study the spin dependence of the electronic structure of the Co overlayers. We found that only Co films with a thickness of more than 2 ML are ferromagnetic (with magnetization in the surface plane) at room temperature. For thinner Co films the spectra for both spin channels looked exactly the same (like the spin integrated spectrum), indicating that there is no long range ferromagnetic order in the plane of the sample. In fig. 5.6 we present the spin resolved spectrum of 4 ML Co / Cu (100). This spectrum, taken at normal emission with 45 eV photon energy is shown in fig 5.6 together with the polarization curve ($P = N^{\uparrow} - N^{\downarrow} / N^{\uparrow} + N^{\downarrow}$). Here one can see a structure in the polarization between the Fermi level and 3 eV binding energy, while for higher binding energies it is nearly constant at about 20 %. The spin integrated photoemission spectrum (top) is the sum of the emission of majority ($\blacktriangle$) and minority ($\blacktriangledown$) electrons, as shown in the figure. At about 3.5 eV binding energy one can see the emission of Cu equal in both spin channels, because the Cu substrate is not ferromagnetic. There are features in the majority spectrum at about 2.6 eV binding energy ($A\uparrow$) and at 0.6 eV binding energy ($S\uparrow$). A minority peak is observed at about 0.9 eV binding energy ($A\downarrow$). So, the Co derived structure below 1 eV binding energy, seen in the spectra of fig. 5.3 consists of a majority and a minority peak, while the structure at higher binding energies corresponds to a majority peak. The origin of these peaks will be discussed below in the chapter about the band structure determination.

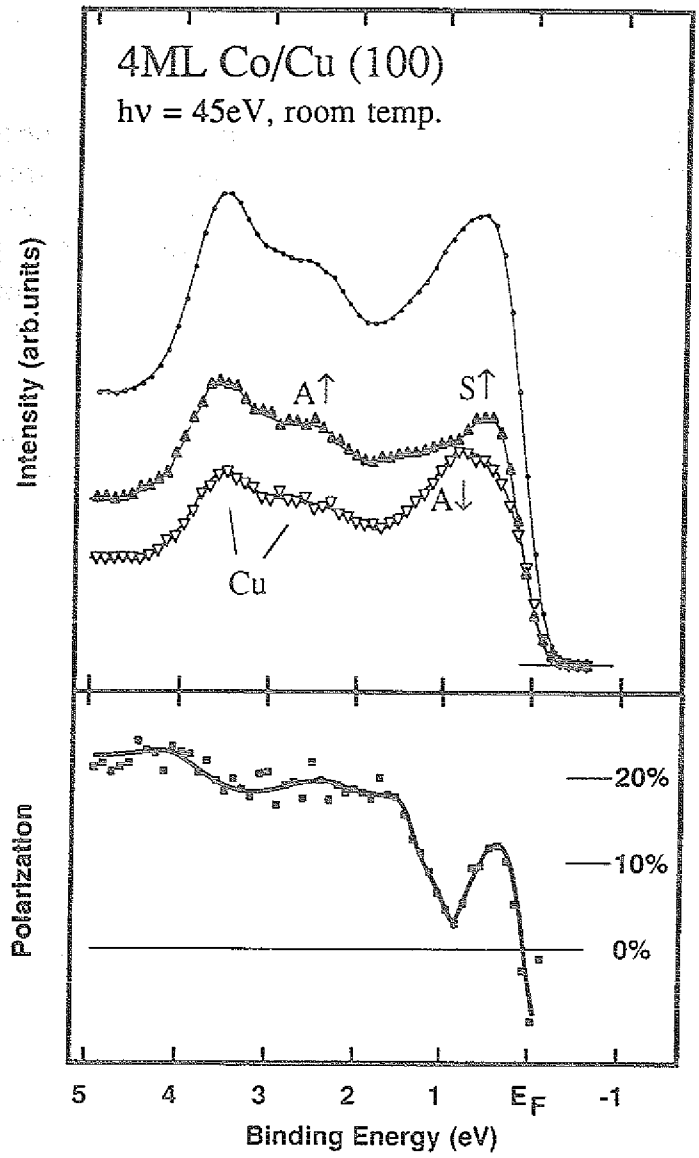

Fig. 5.6: Spin resolved photoemission spectrum of 4ML Co/Cu(100) taken at room temperature with s-polarized light at 45 eV photon energy in normal emission, see text.

Now we want to study samples with different Co film thicknesses. Fig. 5.7 shows the spectrum for 1 ML Co on Cu (100).

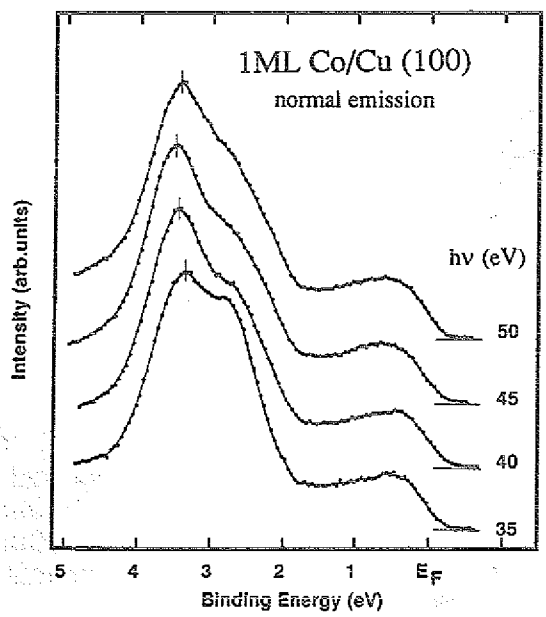

Fig. 5.7: Spin integrated photoemission spectrum of 1ML Co/Cu(100) taken in normal emission at different photon energies.

Because the monolayer system is two - dimensional, it should not show dispersion in the photoemission spectra taken at normal electron emission varying the photon energy. It is not periodic normal to the plane, therefore no $k_\perp$ is defined. This is shown in fig. 5.7. While the Cu structure shows dispersion coming from emission around the Γ - point of the 3D Brillouin zone, there can be identified no shift in the Co derived structures.

The energy dependence of the spectra of thicker Co film is shown in the next figures. Fig. 5.8 presents the spectra of 2.3 ML Co coverage:

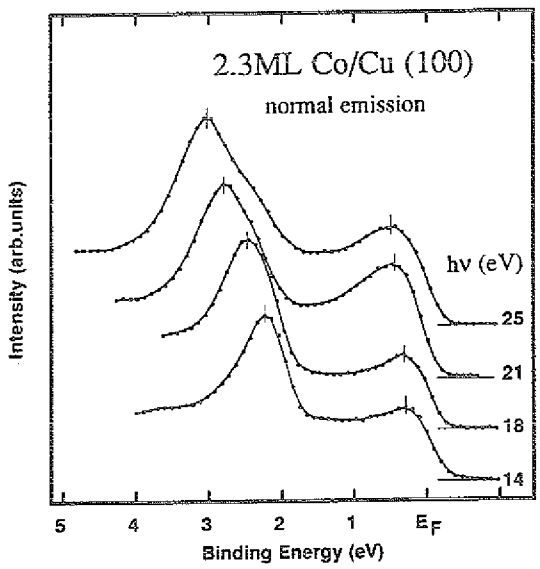

Fig. 5.8: Spin integrated photoemission spectra of 2.3 ML Co/Cu(100) taken in normal emission.

Fig. 5.9 shows the energy dependence of a 2.5 ML Co film:

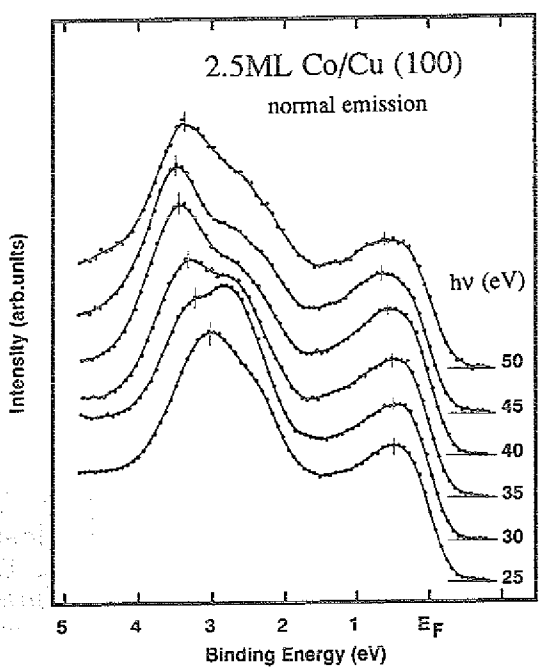

Fig. 5.9: Spin integrated photoemission spectra of 2.5 ML Co/Cu(100) taken in normal emission.

And in fig. 5.10 we present the spectra of a 6 ML Co film:

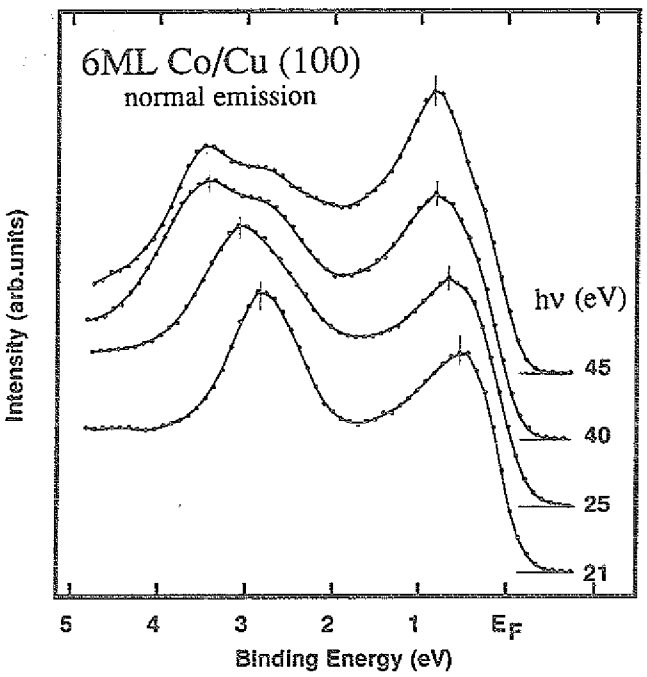

Fig. 5.10: Spin integrated photoemission spectra of 6 ML Co/Cu(100) taken in normal emission.

In the spectra of fig. 5.8-10 one can identify the dispersion of the Cu peak, but also a shift of the Co derived structures below 1 eV binding energy. If this structure would only be one peak, it would show the dispersion of the corresponding state in the bulk Brillouin zone and therefore indicate the three dimensional structure of the overlayer, just as for the Cu substrate. But in the spin resolved spectrum of fig. 5.6 we have seen that this structure is the sum of two peaks, one majority and one minority peak. Therefore the shifts, seen in fig. 5.8-10 can also be due to different intensity ratios of these peaks varying the photon energy. For an unambiguous interpretation of this shift one needs a set of spin resolved spectra, as discussed in chapt. 5.2.

A further characterization of a overlayer system where one can distinguish between emission coming from the substrate or the adsorbate is the use of resonance effects. Photoemission spectra of a 6ML Co / Cu (100) film with photon energies near the Co 3p - 3d threshold energy of about 61 eV are shown in fig. 5.11. In this energy range states with configuration p^5d^{N+1} are degenerate with the final photoemission states p^6d^{N-1} [Davis 86]. If any matrix element connects these two types of states, then autoionization ($p5dN+1 \rightarrow p^6d^{N-1}$) will occur. Therefore one expects resonance effects in this photon energy region due to Co emission, while the Cu emission should be quite constant. One effect one can see in the spectra of fig. 5.11 is the relative decrease of the Co structure near the Fermi

energy. The Cu emission at about 3.5 eV binding energy remains nearly constant and the structure at 2.5 eV binding energy changes slightly, indicating that there is Co and Cu emission in this feature. Above the threshold energy the MNN Co Auger peak with a constant kinetic energy appears in the spectra with a broad structure. Because the spectra are plotted on a binding energy scale relative to the Fermi energy, the Auger peak shifts to higher binding energies with increasing photon energy.

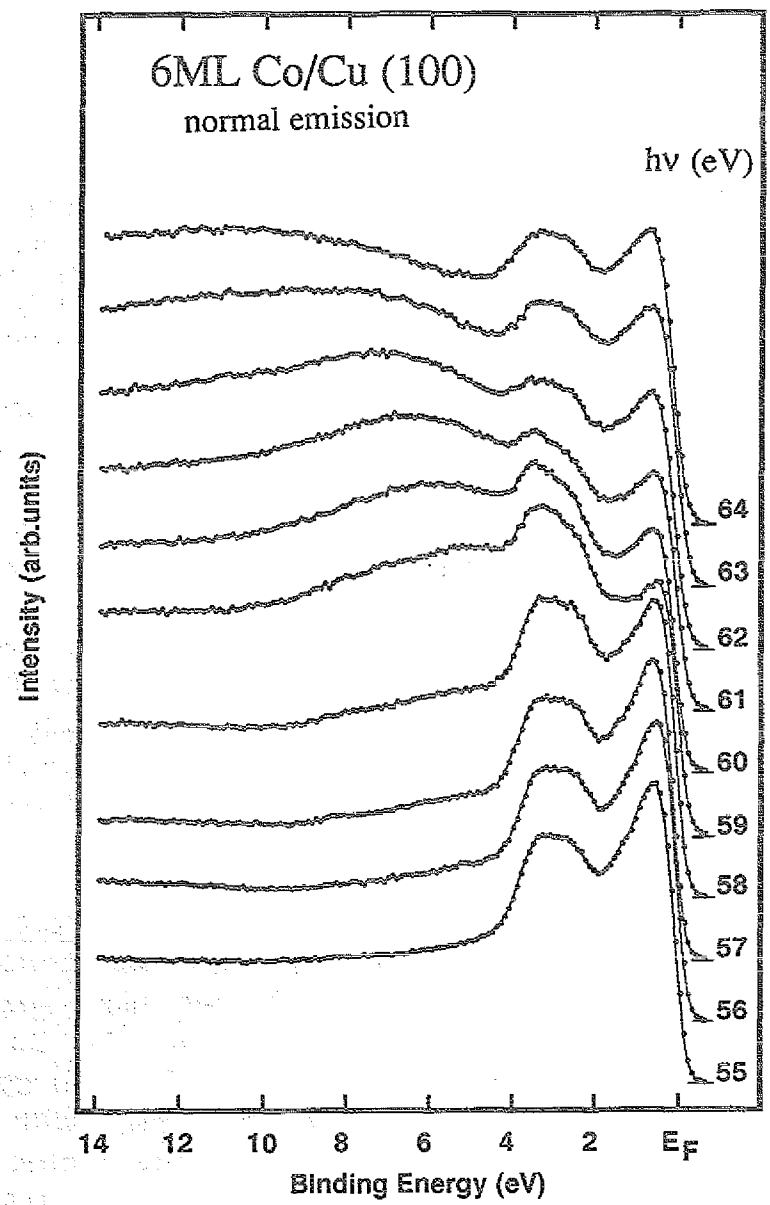

Fig. 5.11: Spin integrated photoemission spectra of 6ML Co /Cu(100) taken in normal emission with s-polarized light varying the photon energy around the Co 3p threshold energy of about 61 eV

5.2 Bandstructure Determination of fcc Co(100)

In the previous discussion we have seen that the Co films of 2.5 ML thickness and more seem to have three dimensional character. But for a clear identification we need spin resolved spectra. In fig. 5.6 we identified already the spin character of the Co derived features in the spectra. There is a minority and a majority peak near the Fermi energy and an additional majority structure at higher binding energy. The emission from the Cu substrate is unpolarized.

By using linear polarized light in normal incidence ($\rightarrow$ s - polarized light) and measuring the electrons for normal emission from the (100) surface of a cubic crystal. we can detect only bands of Δ_5 symmetry of the three dimensional Brillouin zone (see chapter 3). In fig. 5.15 we show a calculated bandstructure in the high symmetry Γ - X direction for fcc Co with the Cu lattice constant [Noffke priv.]. There is one band with Δ_5 symmetry. Because of the ferromagnetism of Co it is exchange split. The majority band is at higher and the minority band at lower binding energies.

In fig. 5.12 we show spin resolved spectra of rel. thick Co films of 12 and 14 ML thickness for photon energies from 18 to 45 eV. Here one can see a minority peak with low intensity at 18 eV photon energy at a binding energy of about 0.4 eV. With increasing photon energy the intensity of this peak increases and at 45 eV photon energy its intensity is even higher than the majority emission. Its maximum is shifted now to 0.9 eV binding energy. There is also a majority structure at 0.6 eV binding energy in the spectra. This peak does not change with the photon energy, it remains at a constant binding energy and intensity. There is another majority structure at higher energies; the position of this peak is hard to find from the spectra alone, but one can evaluate it by using difference curves, as discussed in chapter 5.3. These majority structures shift with the photon energy in the same way as the minority peak. The majority and minority peak that shift have 3 dimensional character. Because of the symmetry rules mentioned above, they must be due to the exchange split Δ_5 band of the bulk Brillouin zone. To determine the bandstructure we need to know the final state to find out the $k^{\perp}$ values of the initial state. We assume a free electron parabola with an effective electron mass of 1 m_e as final state. For the exact determination we need to know the inner potential of this final state. Therefore we need to have more spectra, especially at photon energies that correspond to emission around the Γ - point.

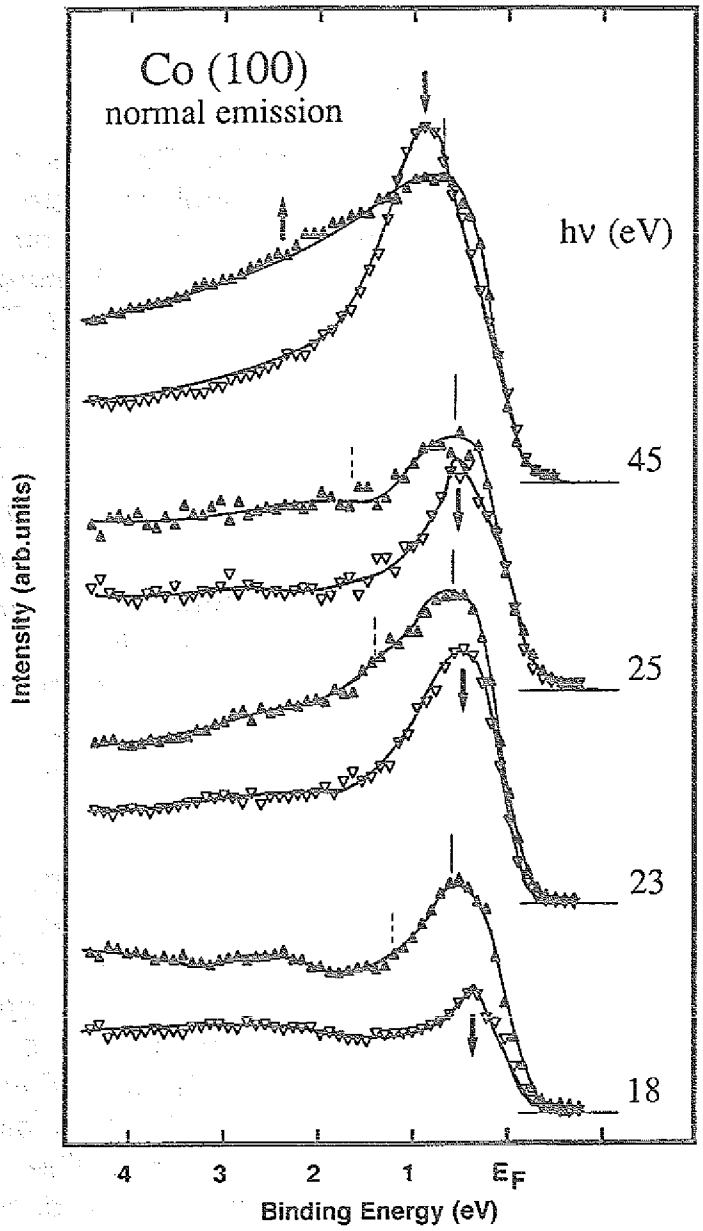

Fig. 5.12: Spin resolved photoemission curves of Co / Cu (100) taken in normal emission with s-polarized light varying the photon energy. The thickness of the Co films is 14 ML for the top spectrum and 12 ML for others. (△) indicates majority and (▽) minority spin emission, rsp.

Because of the loss of some 10^{-3} in the intensity due to spin analysis it takes much more time and effort to take spin resolved spectra than spin integrated ones. One problem in the spin integrated spectra is that one can not identify their spin character. But in fig. 5.6 and 5.12 we have done this, so we can go on from now with spin integrated spectra. Fig. 5.13 shows a set of spin integrated spectra of a 8ML Co film taken in normal emission with photon energies from 12 to 50 eV. With this Co coverage one can still identify the Cu substrate emission, marked with Cu. From fig. 5.6 and 5.12 we could also mark the majority and minority peaks in these spectra. The Cu peak shows the same dispersion with the photon energy as for the uncovered surface. The majority peak $A^{\uparrow}$ also shifts in energy from about 0.6 eV at 12 eV photon energy to a maximum of about 2.4 eV in the range of 45 eV photon energy. In the spectra around 30 eV photon energy the position of this peak cannot be identified unambiguously,

here it is marked with dashed lines. The minority peak can be distinguished from the other majority peak only for photon energies above 25 eV in these spectra. It shifts to a maximum value of 0.9 eV binding energy near 45 eV photon energy. The majority peak at 0.6 eV binding energy does not shift in energy over the whole photon energy range.

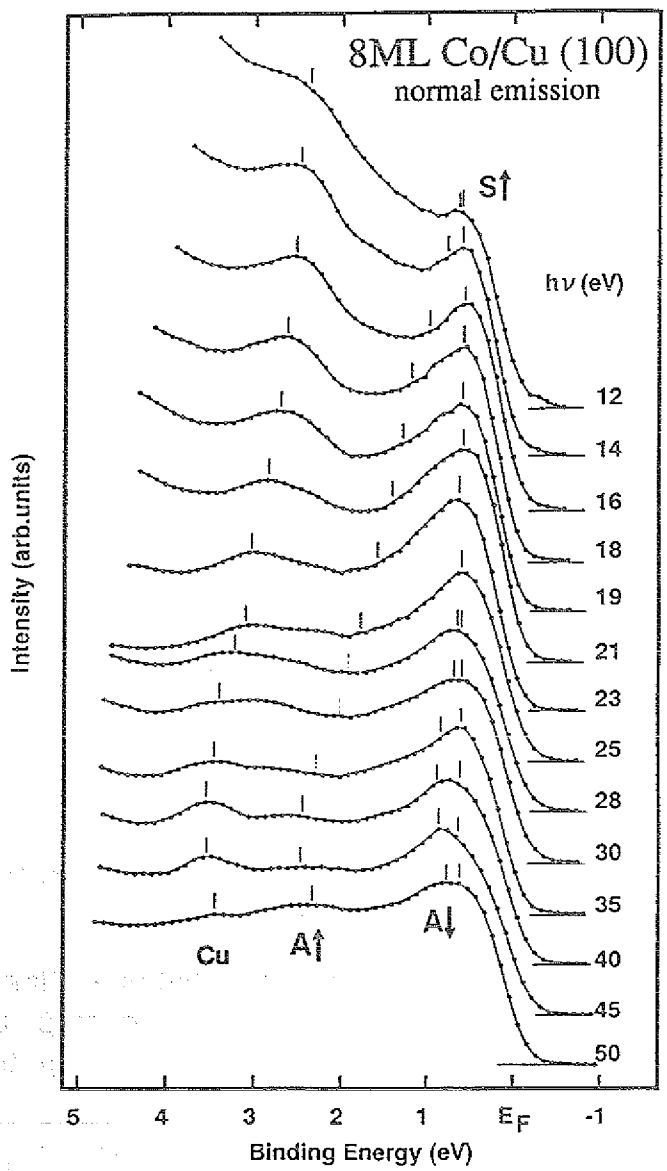

Fig. 5.13: Spin integrated photoemission spectra of 8 ML Co/Cu(100) taken in normal emission with s-polarized light varying the photon energy.

Now we have seen the dispersion of the peaks coming from the Δ_5 band, but to determine the inner potential we must know the photon energy corresponding to emission from the Γ point with more accuracy. Therefore we have taken another set of spectra with photon energies varied around 45 eV where the peaks have their maximum in binding energy. This is shown in fig. 5.14 for a 9ML Co film. The maximum for the dispersion of the Cu peak is at 45 eV photon energy and for Co it is at 43 eV photon energy. This leads to an inner potential for the Co final state of -5 eV (according to eq. 3.13).

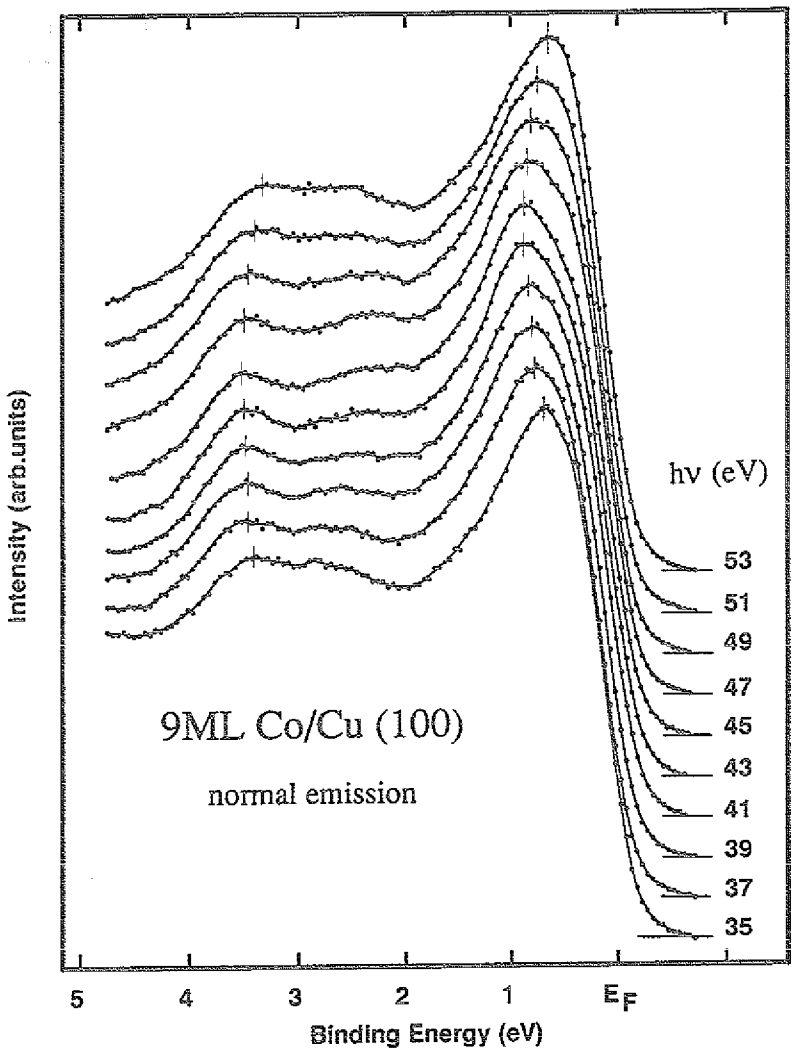

Fig. 5.14: Spin integrated photoemission spectra of 9 ML Co/Cu(100) taken in normal emission with s-polarized light varying the photon energy around the 45 eV.

Now we can calculate using eq. 3.12 the $k^{\perp}$ values of the initial states from the peak positions and the photon energies of the photoemission spectra and determine the Co bandstructure in the Γ - X direction of the Brillouin zone, see fig. 5.15.

The calculations show that, at 8 ML coverage, the experimental spectral features and their energy dispersion are well accounted for by bulk transitions. The spin-up peak at a constant binding energy of about 0.6 eV below E_F, which displays no dispersion upon variation of the photon energy is an exception, having no correspondence in the bulk band structure. We attribute this feature to a Co 3d spin polarized surface state or surface resonance. Further support to this interpretation is given by the surface sensitivity of this majority spin feature, which is strongly attenuated by small (1-3 L) oxygen exposures, see chapter 6.

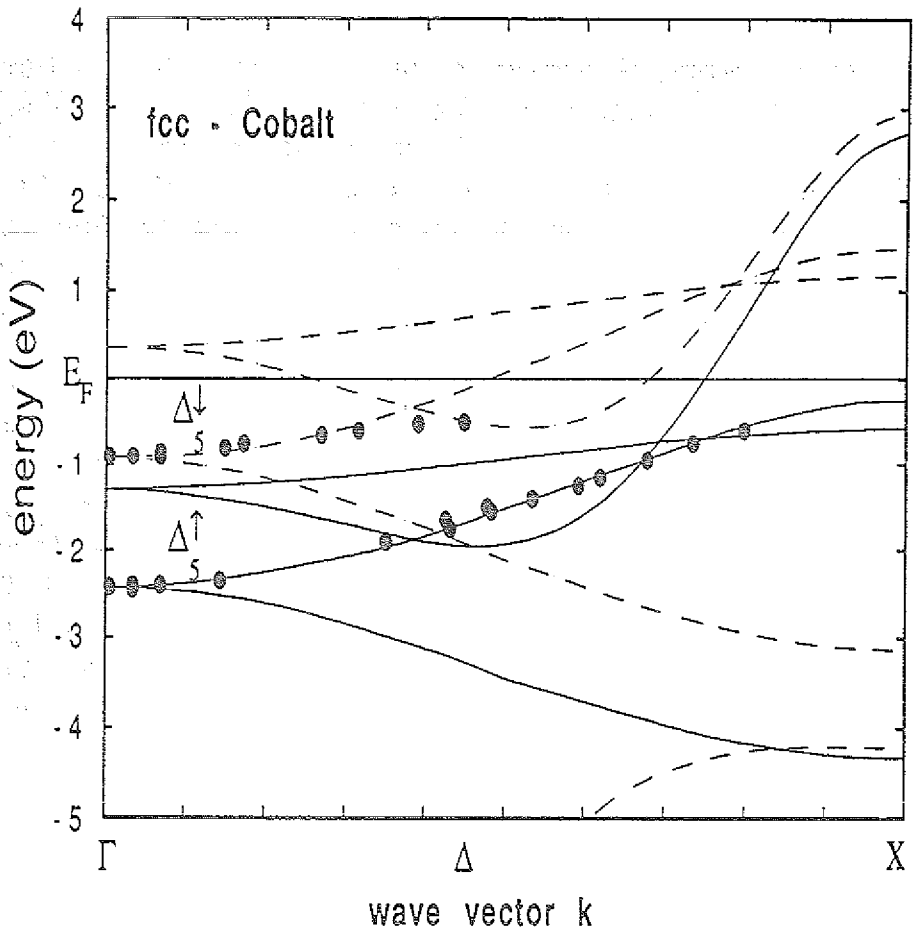

Fig. 5.15: Band structure of fcc Cobalt in the Γ - X direction of the Brillouin zone. The solid (dashed) lines show the calculated majority (minority) bands of fcc Cobalt in the Cu lattice constant [Noffke priv.]. The dots correspond to experimental determination of the Δ_5 bands from the energy distribution curves of Co films having bulk character (Co thickness > 5ML)

A pair of exchange split states of Δ_5 - symmetry at the center of the Brillouin zone contributes to the spin-up emission at 2.45 eV binding energy and to the corresponding spin-down features at 0.9 eV binding energy. Their exchange splitting for bulk like Co films (> 5ML thickness) is (1.55 ± 0.15) eV, in good agreement with the calculated value of 1.55 eV [Noffke priv.].

We notice that the overall agreement between the experimental results and the calculated band structure shows that a single particle description of these photoemission spectra based on an

itinerant picture of the Co 3d states is satisfactory, at least within the present level of accuracy. Furthermore we observe that no multi-electron satellite could be detected even at low coverage (0.5-2 ML), indicating that correlation effects in this two-dimensional system may be significantly smaller than theoretically predicted [Chen 90]

In a previous work, Schneider et al. [Schneider 90 (2)] have also determined the bandstructure of fcc Co on Cu (100). They find consistent results with the calculated band structure of Noffke [Noffke priv.]. But they could not see a dispersion of the peaks in the spin integrated spectra and they found an exchange splitting which is significantly smaller than given by the band structure calculation. Schneider et al. have been restricted to photon energies up to 30 eV. Therefore they were able to detect emission corresponding to the range of the X-point of the Brillouin zone to the center of the Γ - X direction but not from the Γ point of the Brillouin zone. The determination of the exchange splitting near the center of the Γ - X direction is complicated because the minority band crosses the Fermi level. In this case one sees the peak of this band in the photoemission spectra of different photon energies at nearly constant binding energy but with changing intensity, as we have seen it in fig. 5.12. This is also the reason why the two minority-dots in the middle of the Γ - X direction in our band structure determination, do not fit to the band structure. The reason why Schneider et al. saw no dispersion in the spin integrated spectra might be because the peaks from the Co bands are overlapping with the majority surface state that does not show dispersion and is quite strong in intensity.

5.3 Quantum Size Effects and the Enhancement of the Exchange Splitting in Ultrathin Co-Films

The modification of a bulk wave function of an infinite solid caused by a reduction of at least one of the dimensions is referred to as quantum size (QS) effect. QS effects in general result in a change of the eigenvalue spectrum of the solid. In semiconductor overlayers and heterostructures this is readily observed, for example, as a change in the bandgap. Thus QS effects even found technological applications in quantum well lasers [Kolbas 84].

For thin metallic films this particular effect of the reduced dimensionality is more difficult to detect since bandgaps exist only at certain k-points in the Brillouin zone. Therefore only few

experimental studies of QS effects in these systems are available today. One of them is Pd on Nb(110) [Pan 88] where Nb is expected to show a partial bandgap between bcc bonding and antibonding states. Another work is done for Ag on Fe(001) [Brookes 91], where the Ag 4d band and the Fe 3d band are well separated in energy and hybridization effects are small. Himpsel [Himpsel 91] studied Quantum-well states in Fe films on Au (100), where the Fe 3d and Au 5d bands are also well separated in energy. But until now there is no systematical study on the influence of QS effects on magnetic properties in ultrathin magnetic films.

All of the theoretical efforts so far have focussed upon the understanding of the magnetic ground state structure of monolayer systems. In particular, spin polarized band structure calculations by several groups [Fu 85], [Li C. 88], [Li C. 90], [Richter 85], [Blügel 89] predict an enhancement of the ground state magnetic moment in 3d metal monolayers in those systems where the overlayer-substrate hybridization is weak.

This work presents the first systematic experimental and theoretical investigation of the influence of QS effects on magnetic properties of thin magnetic films. We have chosen Co overlayers on Cu(100) because the Co and Cu 3d hybridization is expected to be weak and because Co grows epitaxially in the layer by layer mode on Cu (100). We studied the dependence of the exchange splitting of the Δ_5 bulk band of Co on the dimension (D) of the Co film by varying the Co coverage from 1-14 atomic layers, thus changing the dimension of the film from 2D to 3D.

In Fig. 5.16 we show energy distribution curves of the clean Cu(100) substrate and of 1 and 2.5 ML Co on Cu(100). The spectra are measured with 45 eV s-polarized light in normal emission at room temperature. The spectrum of the clean Cu(100) substrate shows a strong peak at 3.5 eV binding energy which is due to emission from bulk states of Δ_5 symmetry close to the Γ point (see discussion above and ref [Thiry 80]). The shoulder at 2.5 eV is attributed to Umklapp processes involving transitions from the flat Δ_5 band near the X point.

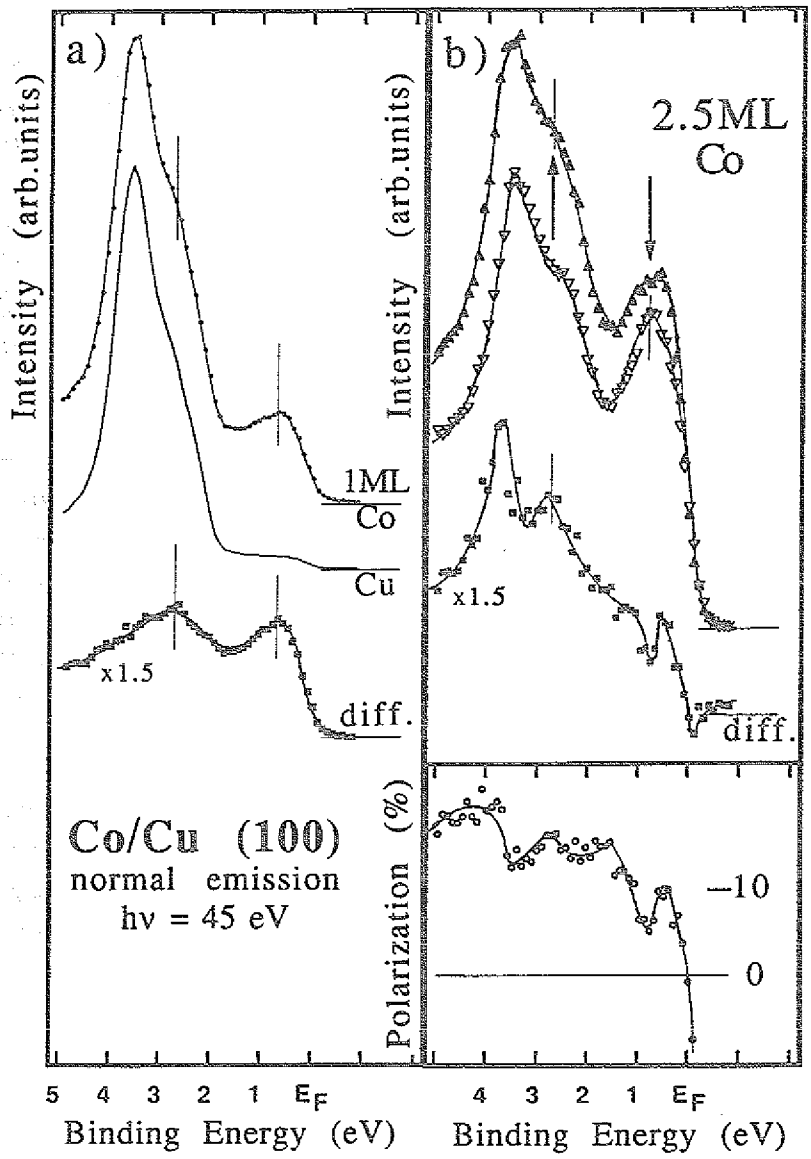

Fig. 5.16: Energy distribution curves taken in normal emission with 45 eV photon energy for 1 and 2.5 ML Co coverages on Cu (100). a) Spin integrated spectrum of 1ML Co compared to a spectrum of clean Cu (100) and the difference curve. b) Spin resolved spectrum of 2.5 ML Co with majority (▲) and minority (▽) spin emission. The arrows show the position of the minority (↓) and the majority (↑) states of the Δ_5 band near the Γ - point of the Brillouin zone, rsp. The difference curve between majority and minority spectra ($N^{\uparrow} - N^{\downarrow}$) is shown underneath ( ). The spin polarization curve ($P = N^{\uparrow} - N^{\downarrow} / N^{\uparrow} + N^{\downarrow}$) is shown at the bottom of the figure.

Upon Co deposition new spectral features appear within 3 eV from the Fermi level. Up to 1 ML coverage the Co-induced features do not show energy dispersion varying the photon energy, see fig. 5.7, as expected for two-dimensional states (i.e. states which are localized near or at the surface plane). The difference curve in fig. 5.16a shows the double-peaked lineshape of the Co induced emission for 1 ML coverage.

Above 2 ML the onset of the photoelectron spin polarization reveals that the overlayer attains long range ferromagnetic order in the surface plane. The 2.5 ML spectrum in fig. 5.16b shows a spin-up (majority) and a spin-down (minority) peak within 1 eV from the Fermi level. Another spin-up Co state, superimposed on the unpolarized Cu d band emission, grows near 2.5 eV. This peak and the spin-down peak below 1 eV binding energy correspond to emission from the Δ_5 derived state near the Γ - symmetry point. We evaluated the exact position of the Δ_5 spin-up peak in the spectra on the basis of a subtraction of the minority spin photoemission from the majority spin photoemission which is also shown in fig. 5.16b. A maximum in the difference curve at 2.7 eV binding energy corresponds to the spin-up peak position. A second structure around 3.5 eV binding energy, that appears also in the polarization curve shown at the bottom of fig. 5.16b, may be an indication for a weak but not negligible hybridization between the Cu substrate and the Co overlayer. The spin resolved spectra for higher Co coverages are shown in fig. 5.17:

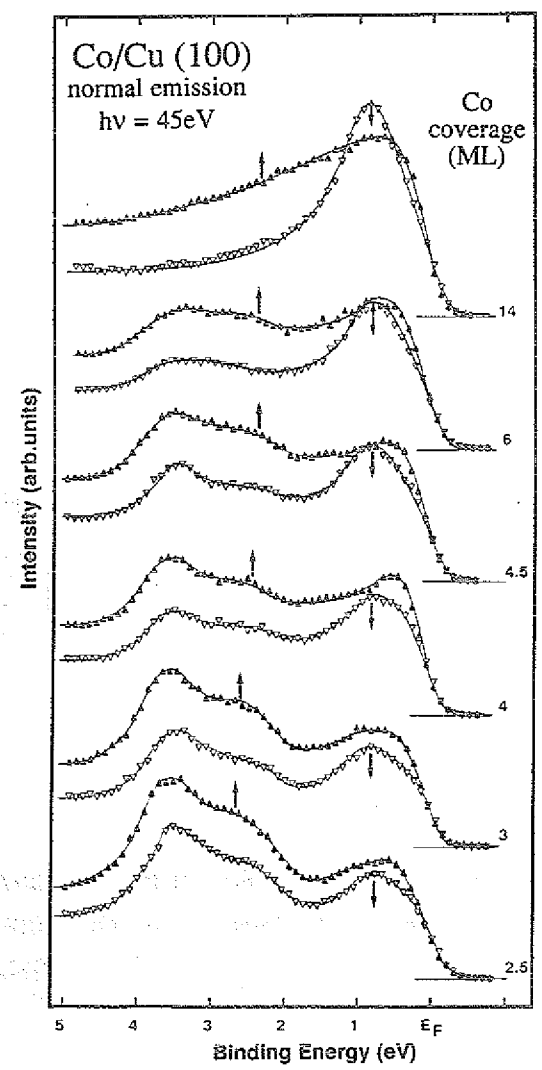

Fig. 5.17: Spin resolved photoemission spectra of Co films on Cu (100) with different Co thicknesses taken in normal emission with 45 eV photon energy. Filled triangles (▲) correspond to majority and open triangles (▽) to minority spin electrons, respectively.

The spectra in fig. 5.17 display rather similar spin polarized features but the peak positions for the Co Δ_5 spin up and spin down states shift in energy; their positions have been evaluated for all Co coverages in the same way as discussed for the 2.5 ML sample. The peaks shift with increasing Co coverage in the way that their energy difference, the exchange splitting, becomes smaller with increasing Co coverage.

The values of the experimentally determined exchange splitting of the Δ_5 band at the center of the Brillouin zone are shown in Fig. 5.18 as a function of the overlayer thickness. All spectra show an exchange splitting, which is a microscopic property, however the photoelectrons are spin polarized only for films larger than 2 monolayers coverage. The exchange splitting for 1ML coverage is obtained from the spin integrated difference curve of Fig. 5.16. The monolayer exchange splitting is found to be enhanced by 25±5 % with respect to thick bulk-like films. The value of the exchange splitting decreases rapidly with increasing Co coverage and approaches the bulk value of 1.55 eV above 5 ML.

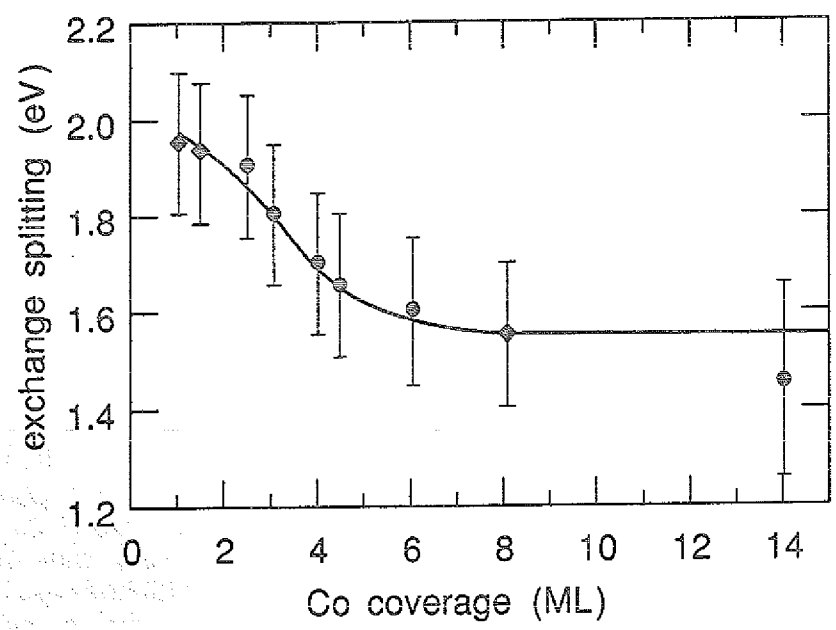

Fig. 5.18: Experimentally determined exchange splitting of the Δ_5 band of fcc Co at the Γ - point of the Brillouin zone as a function of Co coverage on Cu (100). The values are taken from spin resolved (●) and spin integrated (◆) photoemission spectra, rsp.

The exchange splitting is a quantity of a specific electronic state in the film. Depending on the relative amplitude of the wavefunction of this state within the various layers of the film, this state samples the layer dependent magnetic properties in a corresponding manner. We have chosen (by selection of the photon energy, the polarization, the emission angle, and the energy of the observed electrons) a state which as we know develops into the Bloch state representing the Δ_5 state at the Γ point of the bulk Brillouin zone. Consequently we are measuring the change in the exchange splitting as this state develops from a bulk Bloch state to a state with a wavefunction which becomes confined to two dimensional geometry. In other words, these measurements represent bulk measurements of the film studied here and reflect the generally assumed surface enhancement of the magnetic moment only to the extent that the Δ_5 derived state has an amplitude in the surface layer.

5.4 Calculation of the Electronic Structure for the Co/Cu(100) System

The experimental data for the thickness dependence of the electronic structure of Co overlayers on Cu(100) are compared to calculations for this system.

The electronic structure of the solid is determined by the quantum mechanical many electron wave function. It is a function of the spin and space coordinates of each electron. If one is interested in ground state properties, the solution becomes considerably easier by using the density functional theory. In this case the most important property is the electron density that depends only on the space coordinates (3 dimensional vector) of the infinite solid. The electron density, which is normally unknown, is the solution of a highly non-linear functional that cannot be written in a chosen analytical form. The equations split into two non-linearly coupled, three dimensional, time independent partial differential equations, which are the single particle Schrödinger equation and the Poisson equation. If the electron density is known at each point of the solid, one can determine the potential in the solid using the Poisson equation. With this potential one can solve the Schrödinger equation and one obtains the single particle wavefunction. The square of this wavefunction leads to a new electron density. These two equations are solved iteratively until self-consistency in the electron density is achieved.

In general the choice of the method for solving the three main problems i) Schrödinger equation, ii) Poisson equation and iii) self consistency depend on a specific problem at hand. For perfect crystals with high symmetry there are very efficient bandstructure methods (like e.g. the linear muffin tin orbital method (LMTO)) with which one can solve simple problems even on the PC. But in the case of very complex systems such as systems with low dimensionality, low symmetry and magnetism, which we want to discuss here, the effort to solve the 3 mentioned points above increases very rapidly. The method that we use, the FLAPW method (Full Potential Augmented Plane Wave Method, see ref. [Wimmer 81], [Weinert 82]) is by far the most advanced and most successful method of today to solve the electronic structure of these low dimensional systems. The calculations in this chapter have been performed with Stefan Blügel.

The main effort within each iteration cycle is the solution of the Schrödinger equation. The wavefunctions are expanded with problem-oriented basis functions (augmented plane waves) and the solution of the Schrödinger equation is mapped to an eigenvalue problem. The dimension of the matrix depends on the specific problem and is typically in the order of 300 - 1000. For each iteration cycle these matrices have to be generated and diagonalized for about 50 - 300 times. The generation of the matrix elements needs about 30 % of the calculational time. The solution of the Poisson equation is done quite efficiently with the help of a Green's-function method. We use modern algorithms coming from the problem of minimizing high dimensional functions, to reduce the number of iterations to obtain self-consistency.

With these calculations we are able to determine many physical properties like magnetic moments, magnetic spin configurations, work function, spin dependent band structures and others from first principles. In this context we are interested in the development of the electronic structure of Co from the monolayer regime to thicker layers. We have chosen an unsupported (isolated) Co(100) monolayer (UML), and films of 5 layers of Cu (100) coated with a monolayer (1 ML), bilayer (2 ML), and triple layer (3 ML) of Co on each side of the Cu surface, as well as an 11 layer Co(100) slab. The geometry of the 1-3 ML systems is shown in fig. 5.19.

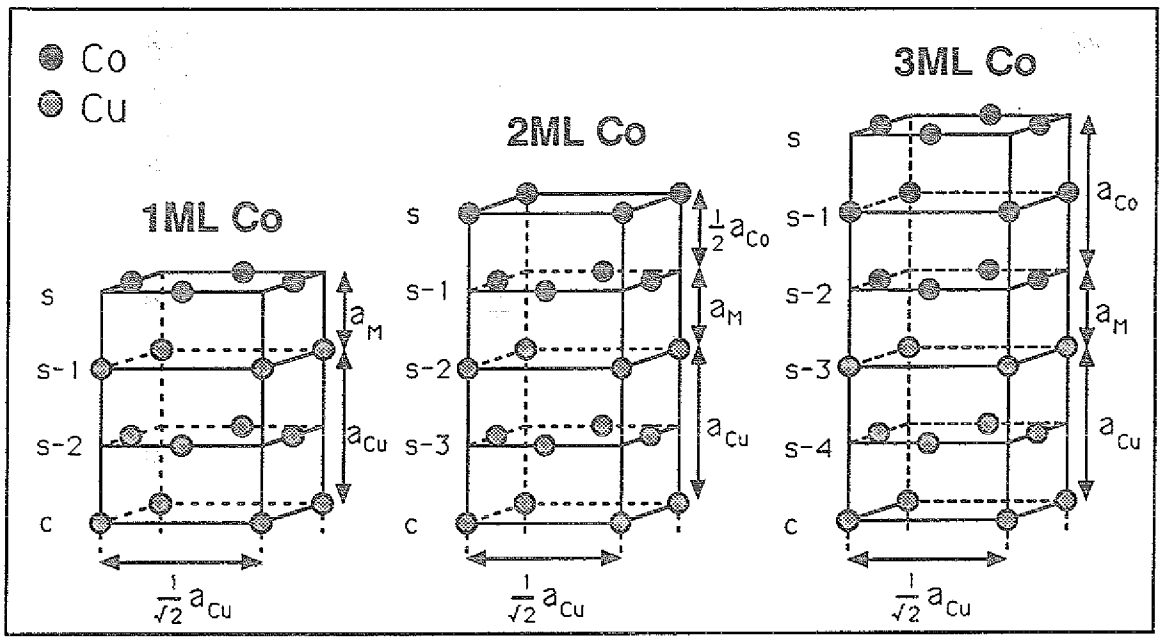

Fig. 5.20: Geometry used for the calculations

For the calculations a total number of about 100 symmetrized pane waves is used as variational basis set. We found that sufficiently accurate Brillouin zone integrations can be performed by using 36 $k_{||}$ points in the irreducible wedge of the 2D Brillouin zone for each system. The systems have been checked additionally with 78 $k_{||}$ points. Lattice harmonics with angular momentum components $l \leq 8$ are included to describe charge and potential inside touching muffin tin spheres. All states including core states are calculated self-consistently. The local density of states (LDOS) and local magnetic moments presented below are data with respect to the muffin-tin spheres.

For Co we assumed an fcc pseudomorphic growth mode with the in-plane lattice constant of Cu of a_{Cu} = 6.83 a.u. (= 3.61 Å) and a lattice constant for fcc Cobalt of a_{Co} = 6.54 a.u. (= 3.46 Å) normal to the film. This represents the experimental determined tetragonal contraction of 3 - 6 % in the Co film [Clarce 87] The interlayer distance between Co and Cu has been estimated to be $1/4 \cdot (a_{Co} + a_{Cu})$. The calculational results in terms of the local magnetic moments and average exchange splittings (explained below) are summarized in Table 5.1.

System	Co-Layer	Magnetic Moment (μ_B)	Exchange Splitting (eV)
UML Co		2.11	1.92
1 ML Co/Cu	s	1.85	1.76
2 ML Co/Cu	s	1.84	1.75
	s-1	1.60	1.58
3 ML Co/Cu	s	1.89	1.79
	s-1	1.67	1.66
	s-2	1.62	1.59
Co	s	1.88	1.78
	s-1	1.68	1.66
	s-2	1.68	1.65
	s-3	1.68	1.64
	s-4	1.68	1.65
	c	1.68	1.65

Table 5.1: Calculated local magnetic moments and average exchange splittings for the fcc Co-Cu (100) systems. s, s-1, s-2 indicates the surface and sub-surface Co layers, respectively; c indicates the center layer of the 11 layer Co slab.

It is shown, that the top surface (s) Co layer has, in agreement with ref.[Li C. 88], [Li C. 90], a magnetic moment of roughly 1.85 μ_B regardless whether the s-1 sub-surface layer is made out of Co or Cu. This is clearly larger ($\approx$ 0.25 μ_B) than the moments of the sub-surface Co-layers, which are approaching the fcc-Co-bulk moment [Li C. 88], [Min 86]. For an UML of Co the magnetic moment is roughly 0.25 μ_B larger than that of the top Co layer. Since fcc Co is a strong ferromagnet (majority band filled) for all systems, the change of the magnetic moment is controlled by the strength of the sp-d hybridization. Thus changing the coordination number from 4 to 8 to 12 for UML, surface (s), and s-1, s-2 sub-surface Co-layers, respectively, increases the strength of the sp-d hybridization and reduces the magnetic moments in steps of $\approx$ 0.25 μ_B. The magnetic moment of 1.68 μ_B of the bulk like atoms in the 11 ML Co slab is slightly larger than the value calculated for a similar calculation of a 9 layer fcc Co (001) slab by Li et al. [Li C. 88] or for bulk fcc Co [Min 86], who both found a bulk magnetic moment of 1.64 μ_B. But this is consistent because we used larger lattice constants (the Cu lattice constant in the plane of the film and the average of the Co and Cu lattice constant normal to the film). Larger lattice constants lead to enhanced magnetic moments due to the reduced sp-d hybridization.

Furthermore we calculated the average exchange splitting as the energy difference between the centers of gravity between the

majority and minority d-bands. We found a strict proportionality between the local moments and the average exchange splitting with $\langle \Delta E \rangle = I \cdot M$, and $I = (0.95 \pm 0.02)$ eV/μ_B for all Co films. Thus the enhancement of the ground state magnetic moment is univocally related to the enhancement of the exchange splitting, and from this point of view we predict an enhancement of the average exchange splitting in the monolayer about 15%.

Now we want to discuss the calculated local densities of states (LDOS) for the Co/Cu (100) systems; they are shown in the following figures. Plotted are the density of states for majority (spin +) and minority (spin -) spin direction separately. The magnetic moment is obtained from the LDOS as the difference of the energy integral of the majority and the minority states below the Fermi energy.

Fig. 5.20 shows the local density of states for the unsupported Co monolayer (UML) compared to the LDOS of bulk Co (taken from the center layer of the 11 ML Co slab) and of bulk Cu (taken from the center layer of 1ML Co/Cu). Due to ferromagnetism in both Co-systems one observes a relative shift in the energy of majority and minority states, where some minority states are shifted above the Fermi level (0 eV in the figure). Co is a strong ferromagnet for all the systems, the majority bands are always filled. The loss of nearest neighbors (from 12 in the bulk system, 8 at the surface to 4 in the UML) leads i) to a reduction of the d-d hybridization and therefore the monolayer bands are narrower than in the bulk ("band narrowing"). This narrowing changes the balance between the magnetic exchange energy and the kinetic energy towards magnetism. Furthermore charge neutrality has to be obeyed. Since Co is a strong ferromagnet, the majority states are always occupied, and charge neutrality is obtained by adjusting majority and minority states rigidly with respect to the Fermi energy. In a second step ii), the loss of nearest neighbors leads to a reduction of the sp-d hybridization which changes the number of the majority d electrons, which increases the magnetic moment and the corresponding exchange splitting. That means, by obeying charge neutrality the increased drive towards magnetism due to the reduced d-d hybridization leads to an increasing exchange splitting as well as magnetic moment, after taking the reduced sp-d hybridization into account.

The LDOS for Cu shows the same states in both spin channels (slightly different shapes come from hybridization with the spin polarized Co overlayer). The main features in the Cu LDOS are between 2 and 4 eV binding energy (= -2 to -4 eV in the figure) and there are only few states near the Fermi level. Compared to the Co

states one can see that the Co majority states are mainly in the same energy region as the Cu states, while the occupied Co minority states are closer to the Fermi level where the Cu density of states is small. From this, one can expect more hybridization between the Co majority states with the Cu substrate than between the Co minority states and the Cu substrate.

Fig. 5.21 shows the LDOS for the surface (s) and s-1, s-2 sub-surface layers of 1ML Co/Cu(100). The LDOS of the Co overlayer has nearly the shape of that of the UML, but it is slightly broader. This indicates a slight hybridization effect due to the Cu substrate underneath. The LDOS of the topmost Cu layer (s-1) also shows a slightly different shape compared to the one of bulk Cu. However the induced moment of about 0.02 μ_B in this Cu layer due to the Co overlayer is negligible. The LDOS of the next Cu layer underneath (s-2) has already nearly the bulk shape. Fig. 5.22 presents the results for the 2 ML Co/Cu system. The Co surface LDOS is again different, it has become even broader but is still narrower than the bulk DOS. The second Co layer LDOS has already more the bulk-like shape. The three layer system is shown in fig. 5.23. Now the surface LDOS has not changed very much any more and also the LDOS for the Co layers underneath are quite similar and bulk-like. The results for the pure 11 ML Co slab, presented in fig. 5.24, show again quite the same behavior.

As with the magnetic moments one can distinguish here between the LDOS of Co surface and bulk. Already the second Co layer is bulk-like.

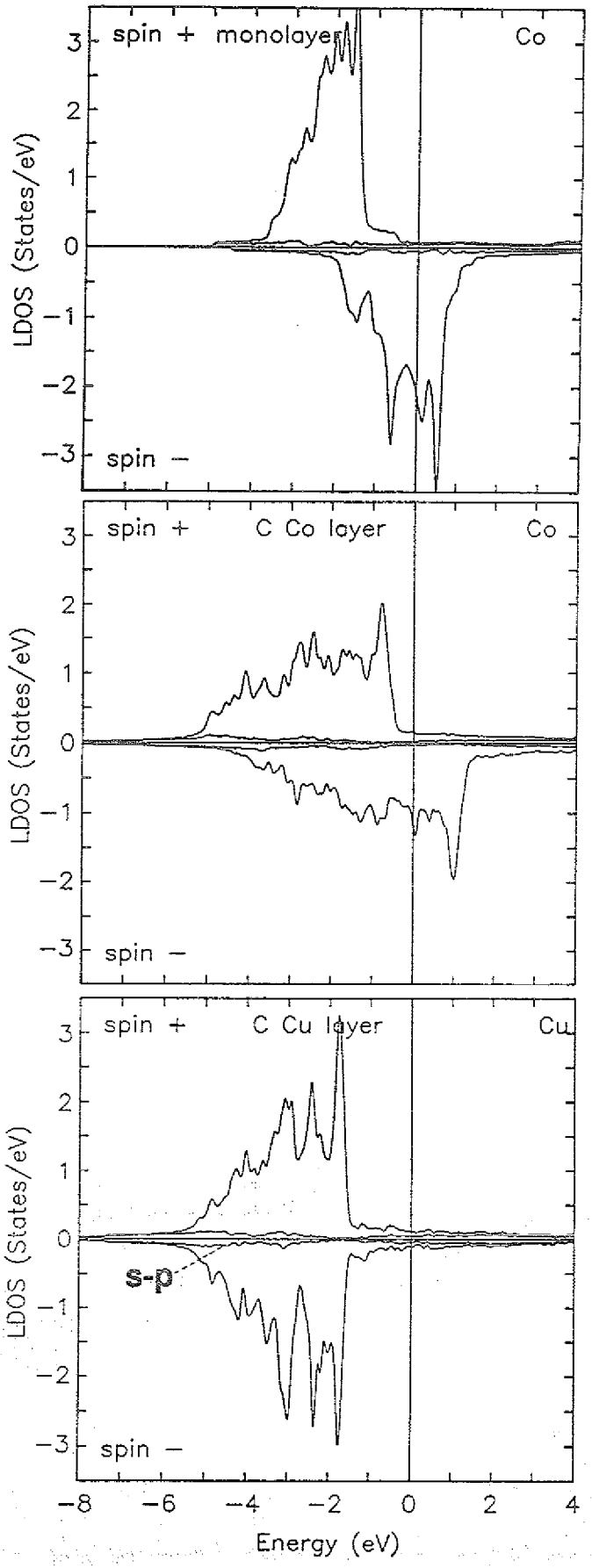

Fig. 5.20: LDOS of a) unsupported monolayer of Co; b) bulk fcc Co and c) bulk Cu

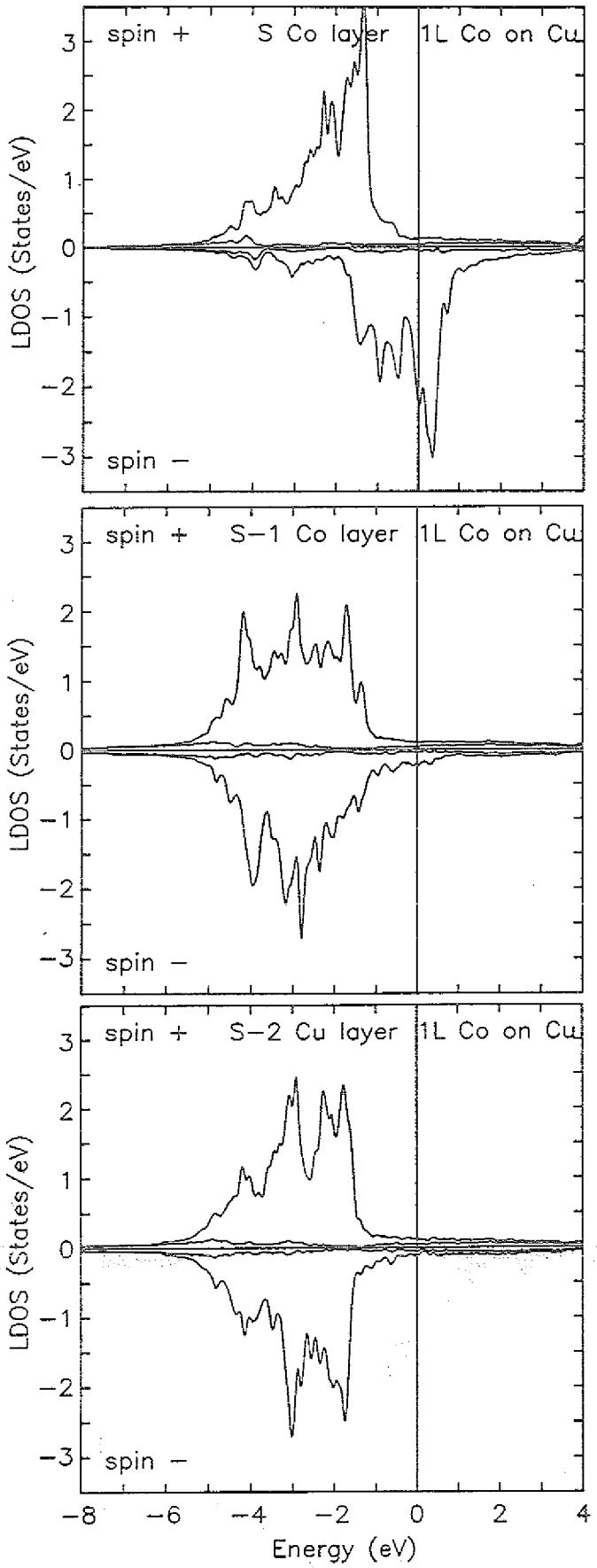

Fig. 5.21: LDOS of 1 ML Co / Cu (100). s, s-1, s-2 indicate the surface and subsurface layers, respectively

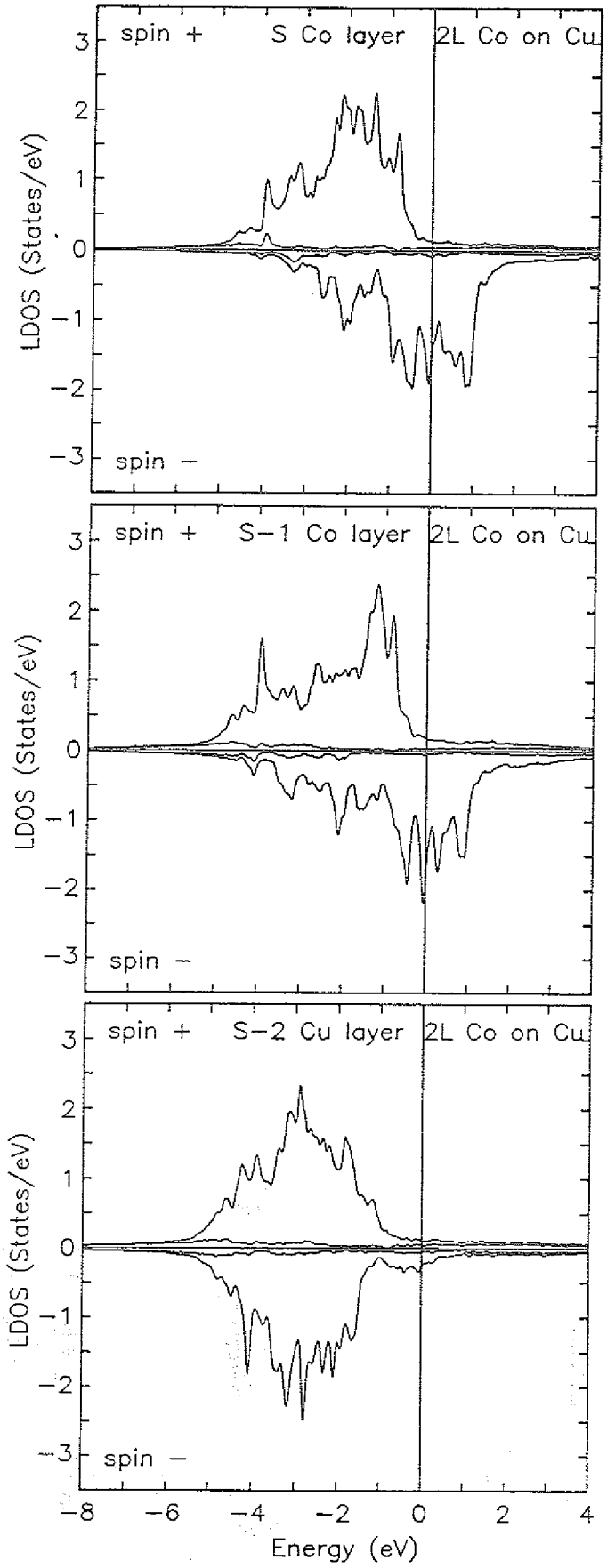

Fig. 5.22: LDOS of 2 ML Co / Cu (100). s, s-1, s-2 indicate the surface and subsurface layers, respectively

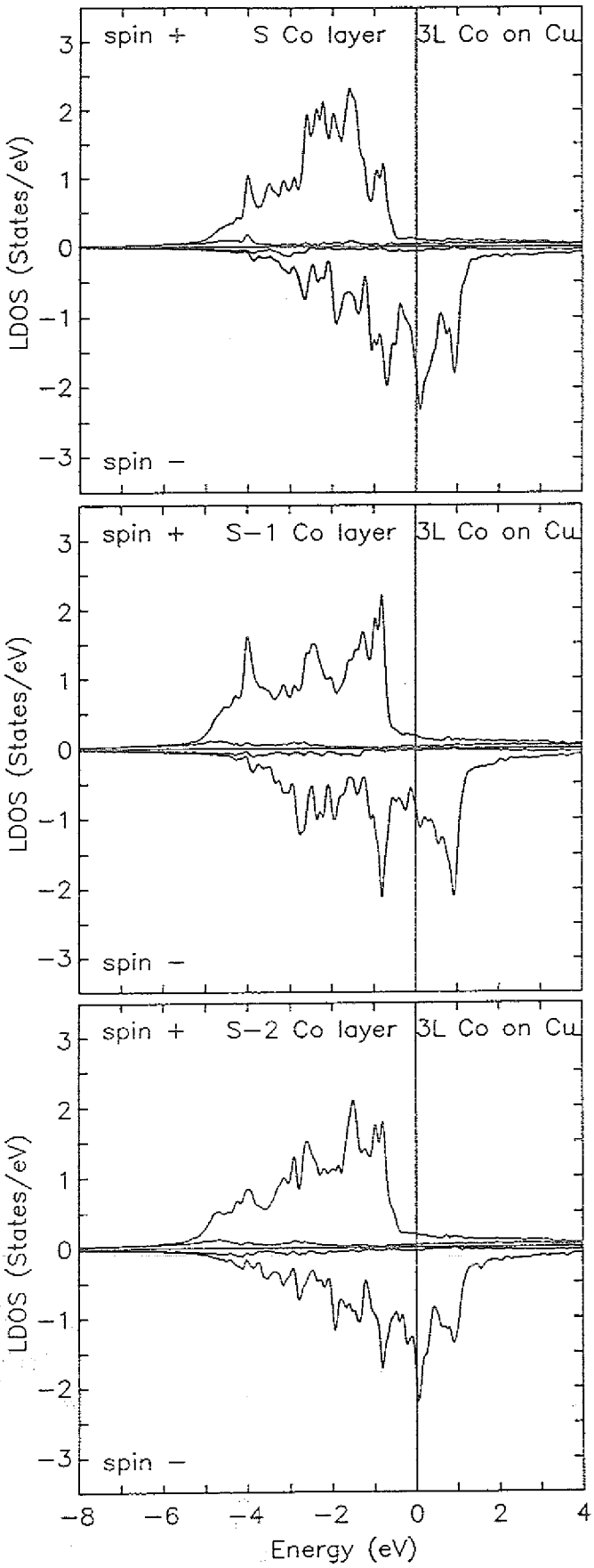

Fig. 5.23: LDOS of 3 ML Co / Cu (100). s, s-1, s-2 indicate the surface and subsurface layers, respectively

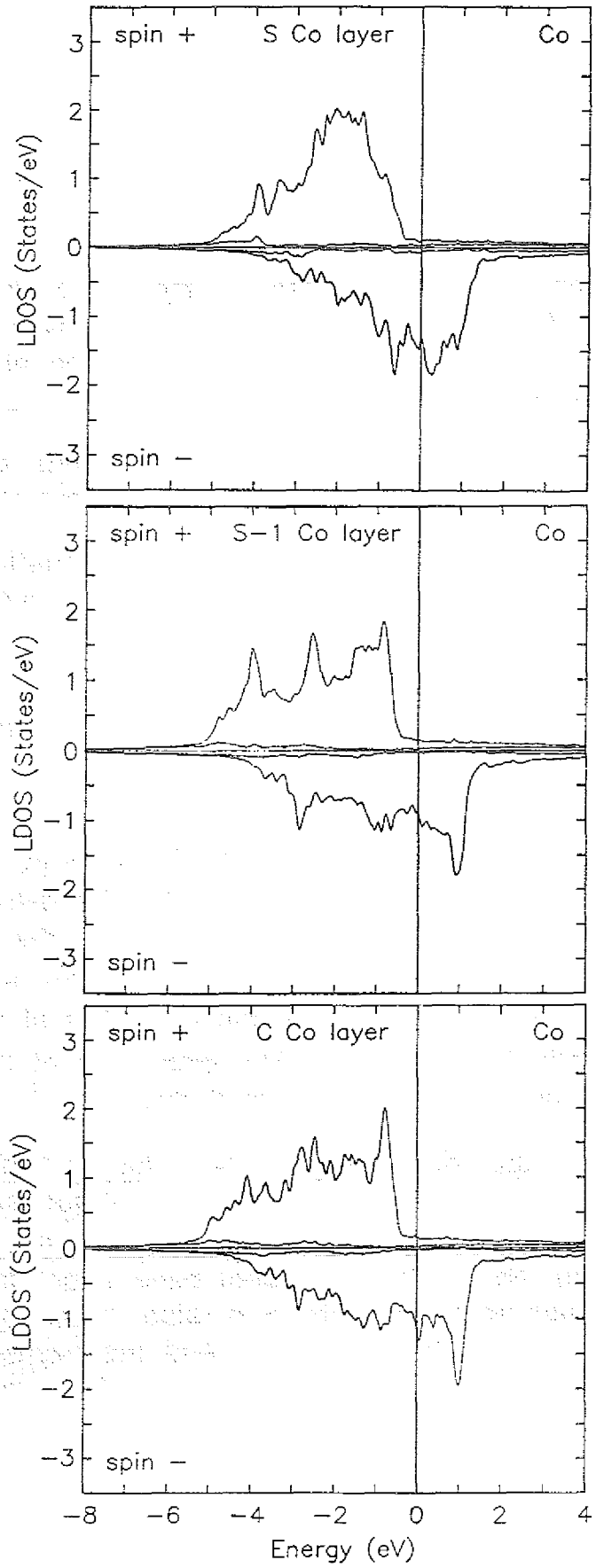

Fig. 5.24: LDOS of Co (100). s, s-1, c indicate the surface, subsurface, and center layers, respectively

5.5 Summary of Chapter 5

In this chapter we have characterized the system Co/Cu (100) and measured the spin dependent electronic structure of ultrathin fcc Co films.

The dispersion of the Cu Δ_5 band in the Γ - X direction of the Brillouin zone was found to be in good agreement with a calculated band structure. An additional feature due to Umklapp processes was identified in the spectra.

Co grows epitaxially in the layer by layer mode on Cu (100), adapting the fcc structure and the in plane lattice constant of Cu.

The onset of long range in plane ferromagnetic order was established to occur at a coverage of 2 monolayers at room temperature.

The monolayer Co on Cu (100) shows a two dimensional behavior, while already for thicknesses of little more than 2 ML a three dimensional character could be seen. Co films of 5 or more atomic layers of Co are bulk-like.

The bandstructure determination for thick, bulk like fcc Co films showed good agreement with a calculated bandstructure of fcc in the Cu lattice constant. The binding energies of the majority and minority states with Δ_5 symmetry at the Γ – point and thus the exchange splitting of the Δ_5 band at the Γ - point of 1.55 eV is in good agreement with the calculation. The dispersion of the Δ_5 bands along the Γ - X direction agrees with the theory as well.

We observed a spin dependent QS effect for Co films on Cu(100) with Co thicknesses less than 5 ML. As a consequence of this the exchange splitting of the bulk Δ_5 state in this low dimensional system is enhanced. New layer dependent band structure calculations confirm these experimental results and also show proportionality between the enhanced magnetic moment and the exchange splitting. Thus the experiment gives evidence of an enhanced local moment for a ML Co on Cu(100).

6. Results from the Reaction of O_2 with fcc Co (100)

The influence of adsorbates on the electronic structure of metal surfaces is of fundamental interest because the surface electronic structure is modified by adsorbates. A question of considerable interest is whether adsorbates destroy the magnetic order on the surface of magnetic materials. This aspect is of topical interest, because recent research shows that thin magnetic films and multilayers become important for magnetic storage with high information density [Erice 91]. In these thin films, some magnetically "dead layers" at the surface induced by adsorbates would have dramatic influence on their magnetic properties.

The chemisorption of different atoms and molecules on transition-metal surfaces has been the subject of a number studies [Plummer 82]. Less well studied has been the interplay of the magnetic or spin properties of the substrate with the chemisorptive activity [Johnson 90]. The measurements on single crystal surfaces are limited until now to Fe and Ni and the results are controversial. They depend on details of the oxidation conditions, on the metal and also on the choice of the crystal surface. The experimental and theoretical models include both the possible formation of magnetic dead layers in the surface region as well as the presence of magnetic moments on the adsorbate.

In the case of oxygen chemisorption on Ni Abraham and Hopster [Abraham 87] found that for Ni (110) there are about two magnetic dead layers induced by the chemisorbed O-c(2x1) structure. Adsorbate induced magnetic dead layers on Ni (110) have also been found by Schmitt et al. [Schmitt 85] and confirmed by theoretical analysis [Feder 85 (2)]. But in more recent work by the same group [Schmitt 87 (1)], [Schmitt 87 (2)], under slightly different experimental conditions, no influence due to oxygen chemisorption has been found on the exchange splitting of Ni (110). On the other hand, Schönhense et al. [Schönhense 88 (1)] found that the O 2p derived bands of chemisorbed oxygen on Ni (110) are exchange splitted, indicating a ferromagnetic order even in the oxygen overlayer. On Ni (001) no appreciable effect on the measured spin dependence or spectral intensity of the Ni 3d photoemission is found [Klebanoff 87], and for Ni (111) Elmers and Gradmann [Elmers 88] found a steep linear decrease of the magnetic moment during chemisorbtion of oxygen, where one single O atom eliminates the magnetic moment of 3.8 - 4.5 bulk Ni atoms.

For chemisorption of oxygen on iron surfaces, the situation is less controversial but also not unambiguous. In an earlier work Allenspach et al. [Allenspach 85] found a complex magnetic structure of an oxidized Fe (001) surface with a mixing of paramagnetic and ferromagnetic layers. Schmitt et al. [Schmitt 87 (2)] found no changes in the binding energy for the Fe d bands for O-p(2x2)/Fe (110). But the chemisorbed O 2p bands on Fe (110) are found to be exchange splitted [Schönhense 88 (2)] and therefore ferromagnetically ordered. The chemisorbed O 2p bands on Fe (001) [Johnson 88] also show an exchange splitting. This is again an indication for the presence of an induced magnetic moment in the oxygen overlayer, which has already been predicted in an earlier theoretical work by Huang and Hermanson [Huang 85]. The Curie temperature of ultrathin Fe films on W (110) is even found to increase due to small exposures (up to 1 L) of oxygen [Weber 90].

With respect to the change of the spin dependent electronic properties due to oxidation of Co single crystal surfaces there is nothing known at all until now. Because of the hcp/fcc phase transition in Co at 720 K it is not possible to get a high quality single crystal surface of a bulk Co crystal. The oxidation studies of Co single crystals in the hcp and fcc phase have mainly been restricted to studies of recrystallized samples with a rather limited crystalline quality and without spin analysis. There is only one study about the oxidation of Co overlayers on Cu (100) [Gonzales 81].

Castro and Küppers [Castro 82] and Matsuyama and Ignatiev [Matsuyama 80] report a first absorption stage for low oxygen exposures on hcp Co followed by oxide phase formation at higher exposures. Maglietta et al. [Maglietta 78] found that the interaction of the (100) fcc Co surface with oxygen produces ordered chemisorbed layers with first a p(2x2) and then a c(2x2) reconstruction. They conclude from a LEED analysis that oxygen is chemisorbed in the fourfold hollow sites with a O-Co distance of 1.94 Å, which is little smaller than in CoO (2.13 Å). The atomic arrangements and metal-oxygen distances are analogous to those observed and studied on Ni(100) [Rae 64]. The reaction of oxygen on the Co overlayers on Cu (100) [Gonzales 81] again shows a similar behavior: a chemisorbed stage at low oxygen exposures and the growth of a surface oxide layer with higher exposures.

Here we have studied the effect of O_2 chemisorption on the electronic structure and magnetism of fcc Co overlayers on Cu (100) by spin- and angle resolved photoelectron spectroscopy, and complemented these experiments by Auger and LEED studies.

6.1 Atomic and Magnetic Structure of the Co Oxides

There are two thermodynamically stable oxides of Cobalt, CoO and Co_3O_4 [Henrich 83].

CoO, like the other transition-metal monoxides MnO, FeO and NiO, is electrically insulating; at elevated temperatures, CoO is a p-type semiconductor. CoO crystallizes in the rocksalt structure (NaCl - Structure, see fig. 6.1) [Goodenough 72], with a lattice constant for CoO of 4.26 Å. Co^{2+} and O^{2-} ions occupy lattice sites on two interpenetrating face-centered-cubic lattices. Both types of ions are sixfold coordinated in the bulk. Below the Néel temperature of 293 K. CoO is antiferromagnetic. CoO exhibits [111] antiferromagnetism, in which all Co^{2+} ions in a given (111) plane have the same magnetic moment and spin direction, which is, due to superexchange through the O^{2-} ions, opposite to the magnetic moment and spin direction of the two neighboring (111) planes of Co^{2+} ions.

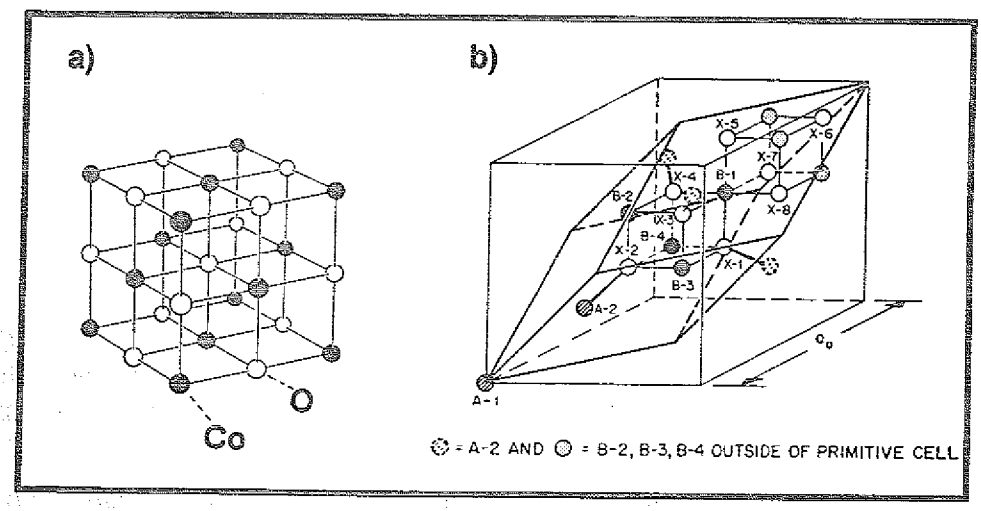

Fig. 6.1: Atomic structure of (a) CoO (rocksalt structure) and (b) Co_3O_4 (spinel structure (shown is the primitive cell)).

Co_3O_4 has the spinel structure (from the spinel $MgO \cdot Al_2O_3$ crystal; Co_3O_4 can also be described as $CoO \cdot Co_2O_3$), see fig. 6.1. The structure is complex, in that there are 8 "molecules" or a total of 8 x 7 = 56 ions, per unit cell. The large oxygen ions are packed quite close together in a face centered cubic arrangement, and the smaller metal ions occupy the spaces between them. These spaces are of two kinds. One is called a tetrahedral or A site, because it is located at the center of a tetrahedron whose corners are occupied by oxygen

ions. The other is called an octahedral or B site, because the oxygen ions around it occupy the corners of an octahedron. The interatomic distance of the A sites is 1.93 Å and of the B sites 1.92 Å [Kündig 69]. In Co_3O_4 the A sites are occupied by Co^{2+} and the B sites by Co^{3+} ions. Co_3O_4 is an antiferromagnet below the Néel temperature of 40 K [Roth 64]. The Co^{3+} have zero permanent moment as a consequence of the splitting of the 3d levels by the octahedral cubic field. The magnetic structure is due to antiferromagnetic ordering of spins in the A sites; each Co^{2+} ion in an A site is surrounded by four nearest neighbors with oppositely directed spins.

Under equilibrium conditions, the system Co_3O_4/CoO shows the behavior of a thermodynamical regular system [Aukrust 64]. There is a clear borderline between stability regions of each phase, where one can say in general that at higher temperatures and lower oxygen pressures CoO is stable and at lower temperatures and higher oxygen pressures Co_3O_4 is stable.

6.2 Valence Band Photoemission, LEED- and Auger-Study

We present here first the results on the oxidation of relatively thick fcc Co films (8-14 ML), which have already developed a bulk-like character.

a) Spin Integrated Photoemission Spectra. Oxidation Stages and Reaction Products.

Spin integrated photoemission spectra measured for oxygen exposures at room temperature are shown in Fig. 6.2. The spectra are measured with 45 eV photon energy for normal electron emission. The clean Co spectrum shows 3d emission in the region within 3 eV from the Fermi level. Most of these features originate from the spin-up and spin-down states with bulk-like character near the Γ symmetry point, as discussed in chapter 5. A small shoulder near 3.5 eV is due to the Cu substrate emission. Exposing the clean Co surface to O_2 produces drastic changes in the spectra. We distinguish in the following between two distinct stages of the oxygen reaction with fcc Co. Oxygen exposures up to about 6 Langmuirs (L) correspond to the first stage. In this range of exposures the photoemission spectra show the growth of an oxygen induced state at 6 eV. In this stage the photoemission spectra show also some changes induced by the oxygen adsorption on the Co 3d valence states. The most remarkable effect is the attenuation of the peak near the Fermi level. Our previous study of the electronic band structure of clean Co layers has

identified a two dimensional spin up surface state (or surface resonance) at 0.6 eV binding energy. The strong changes of the intensity near E_F with low oxygen exposure confirms the surface origin of this feature. Further evidence will be provided in the following by the spin resolved spectra. In the second oxidation stage, above 7 L, several new features appear in the photoemission spectra.

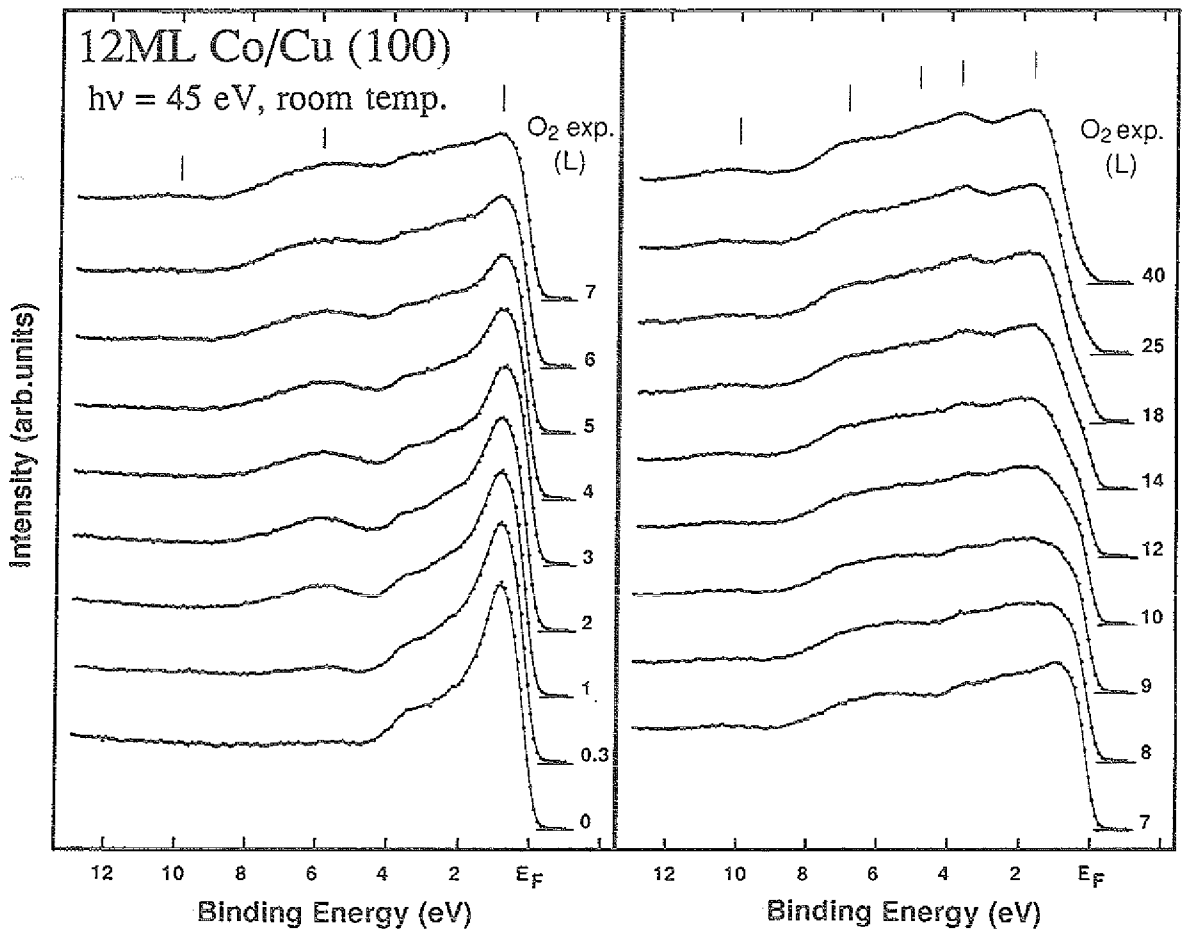

Fig. 6.2: Spin integrated energy distribution curves of 12 ML Co/Cu(100) taken in normal emission with s-polarized light of 45 eV photon energy. The spectra for different Oxygen exposures at room temperature (T = 298 K) are shown.

At 10 eV binding energy a satellite appears in the spectra with intensity increasing with the oxygen exposure, see Fig. 6.3. In the 4-8 eV binding energy region a broad feature develops, which includes several components. Also the Co 3d valence band emission changes dramatically its shape. New Co 3d derived features grow at 1.9 eV and 3.8 eV binding energy. The development of the spectra described above takes place mostly between 7 and 21 L oxygen exposure. For

higher exposures only little changes are observed indicating saturation.

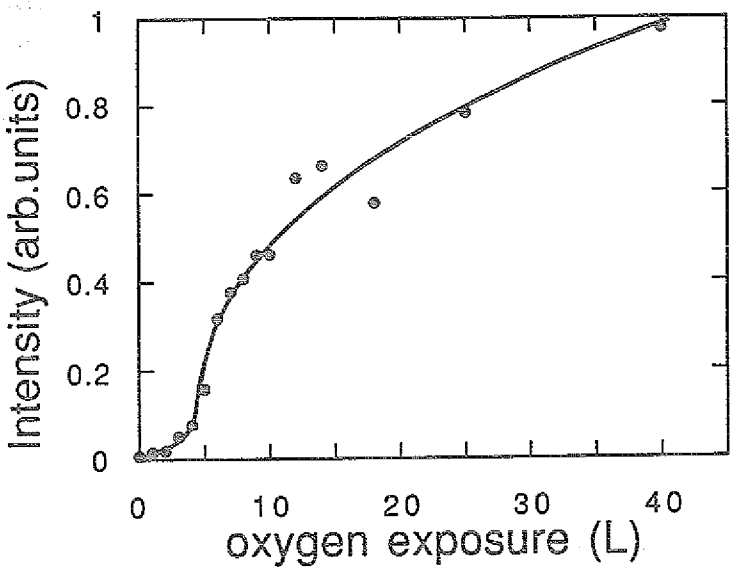

Fig. 6.3: Intensity of the 10 eV satellite in the spectra of 12ML Co/Cu(100) shown in fig. 6.2.

In Fig. 6.4 we present an analogous set of spectra to those presented in Fig. 6.2 only with an even thicker Co film of 14 ML thickness, so that there is no more shoulder from the Cu substrate emission visible at 3.5 eV binding energy in the clean spectrum. The peak positions and the development of the spectra with increasing oxygen exposure are exactly the same as described in Fig. 6.2.

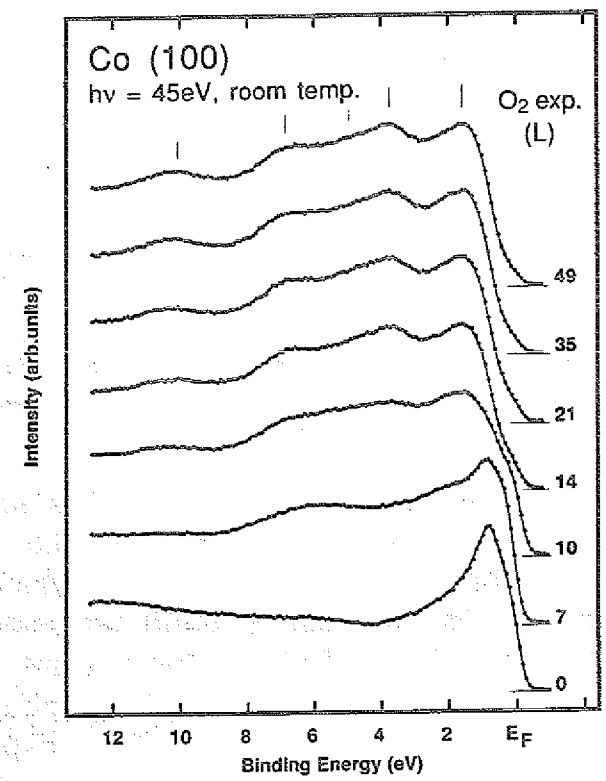

Fig. 6.4: Spin integrated energy distribution curves of 14 ML Co/Cu(100) taken in normal emission with s-polarized light of 45 eV photon energy. The spectra for different oxygen exposures at room temperature are shown.

To obtain a better understanding of the oxidation process we have also characterized the sample by Auger electron spectroscopy (AES) and low energy electron diffraction (LEED). Fig. 6.5 shows the measured AES oxygen (503 eV) to cobalt (775 eV) peak-to-peak ratio as a function of oxygen exposure. Here one can also identify two distinct stages. First the ratio increases drastically up to about 2 L and forms a plateau at R ≈ 0.3 for higher exposures, indicating the first stage (I). Above ≈ 7 L there is again a drastic increase of the ratio, this is the onset of the second stage (II), reaching a saturation limit of O/Co ≈ 1.5. An equal concentration of Co and O in the sample within the probing depth of the experiment corresponds to an Auger ratio of O/Co ≈ 1.9 [Matsuyama 81]). So we can interpret our result in the way that at the surface layers there is a 1:1 concentration of Co and O, corresponding to the formation of CoO, while there are Co layers underneath (within the probing-death) that have still not reacted. An analogous behavior of the Auger ratio has been detected by Matsuyama and Ignatiev [Matsuyama 81] who have studied the oxidation of the hcp (0001) Co surface.

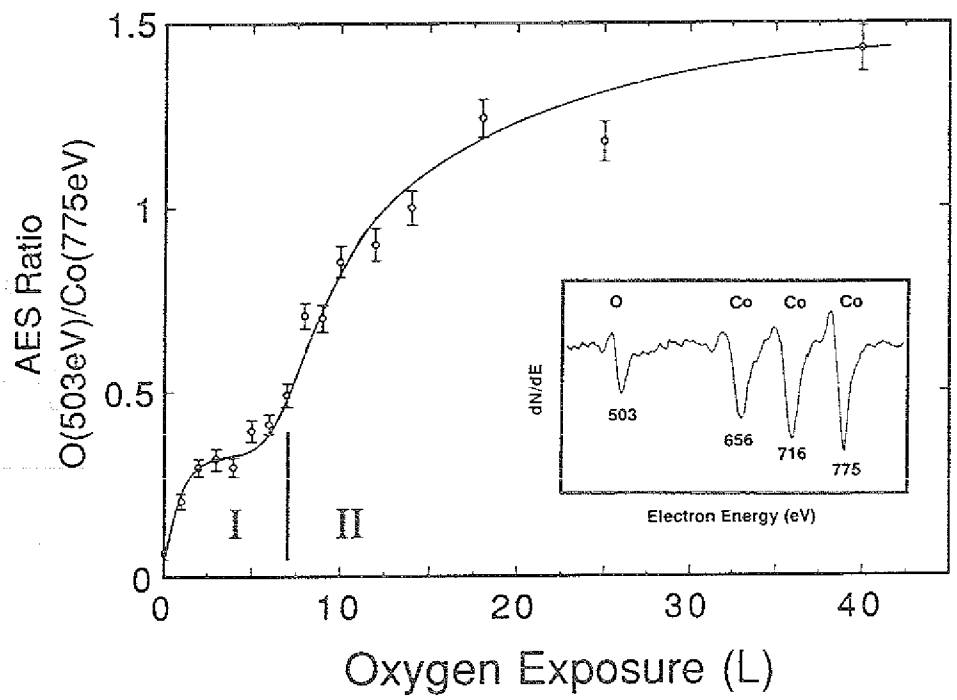

Fig. 6.5: Auger-Analysis of the adsorption process of O_2 on 14ML Co/Cu(100) at room temperature. Ratio of the Auger peak to peak intensity of Oxygen (503 eV) and Cobalt (775 eV) versus oxygen exposure. I and II indicate the regions of formation of two different oxidation stages. Inset: derivative Auger-spectrum after 6L O_2- exposure

The results of our LEED study are shown in Fig 6.7. Picture a) shows the pattern of the Cu(100) substrate surface. The lower right part of it is shown again in b) (see the arrows; the spot on the upper left side is due to the electron gun). Picture c) shows the pattern after evaporation of 5 ML Co. This is identical to b), indicating the epitaxial growth of Co. Pictures d)-f) show the patterns after exposure of 4, 10 and 20 L oxygen on the Co surface at room temperature. For exposures above 2 L the LEED pattern shows extra spots (see the arrow in pict. d) that correspond to a c(2x2) symmetry. This is explained in Fig 6.6, which shows the comparison of a c(2x2) superstructure between the reciprocal two dimensional lattice (→ LEED pattern) and the real surface lattice. The intensity and sharpness of the LEED extra-spots reach a maximum at 4-5 L, followed by a rapid decrease at higher exposures. Above an exposure of 10 L the whole pattern becomes diffuse, indicating a loss of order at the surface. The formation of an O-c(2x2) superstructure at low oxygen exposures has also been found by Maglietta et al [Maglietta 78] on fcc Co (100) and by Matsuyama and Ignatiev [Matsuyama 81] on hcp Co (0001), who also found the disappearance of the surface order at higher exposures.

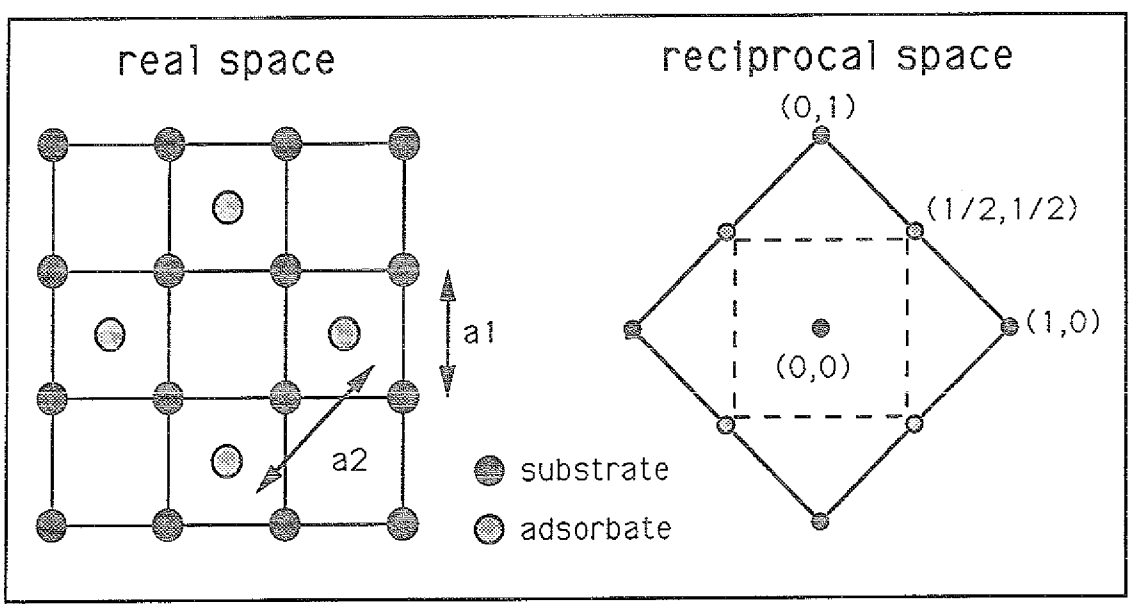

Fig. 6.6: Comparison between the c(2x2) superstructure of an adsorbate on a fcc (100) substrate surface in real and in reciprocal space.

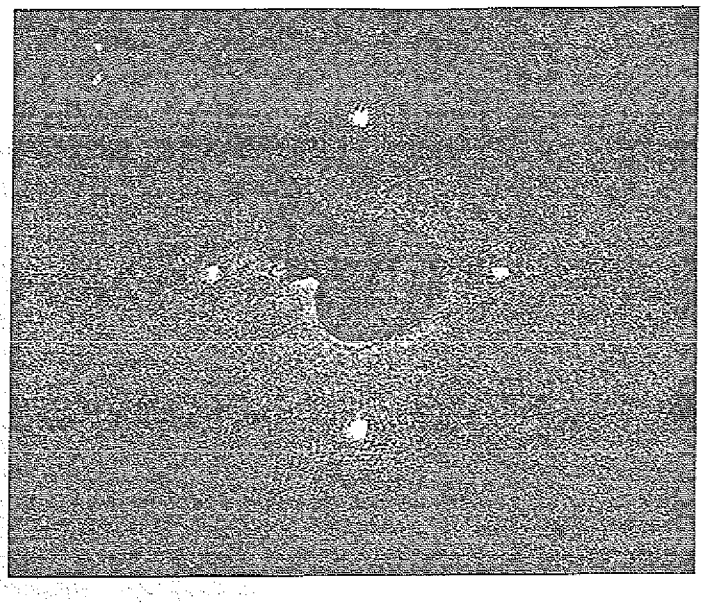

a) Cu

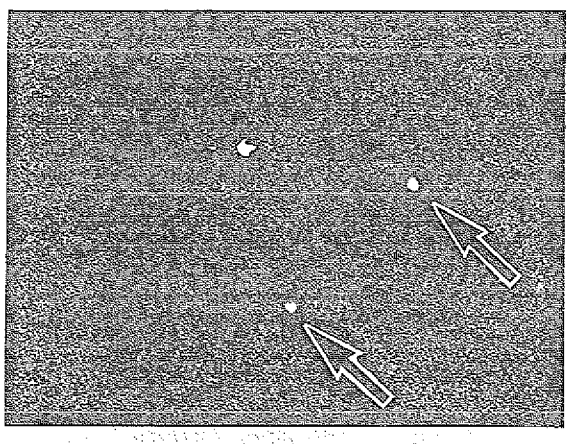

b) Cu

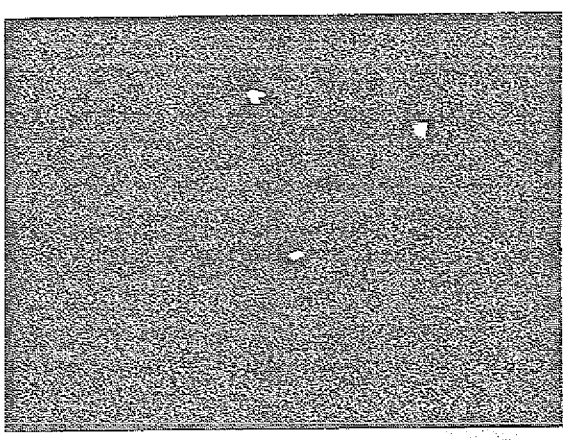

c) 5ML Co

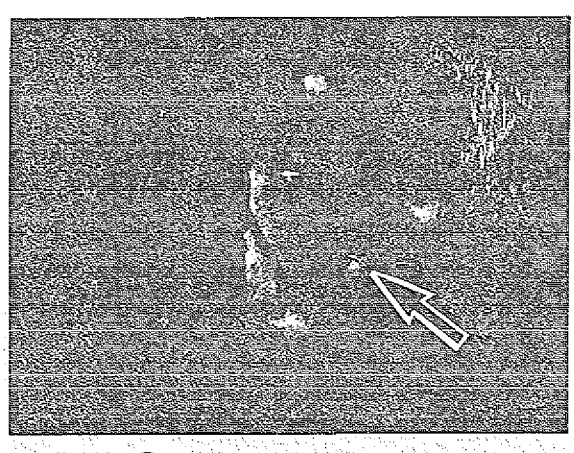

d) 4L O_2

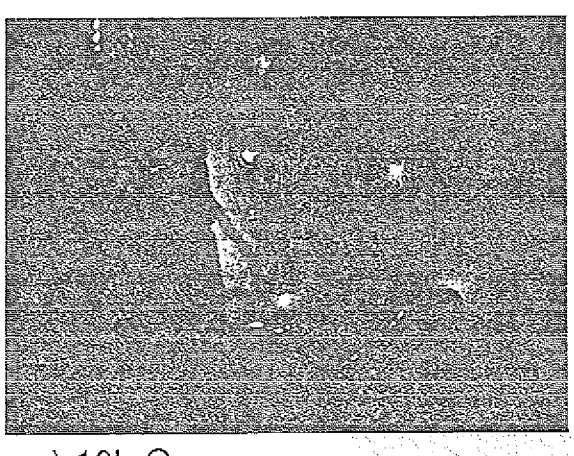

e) 10L O_2

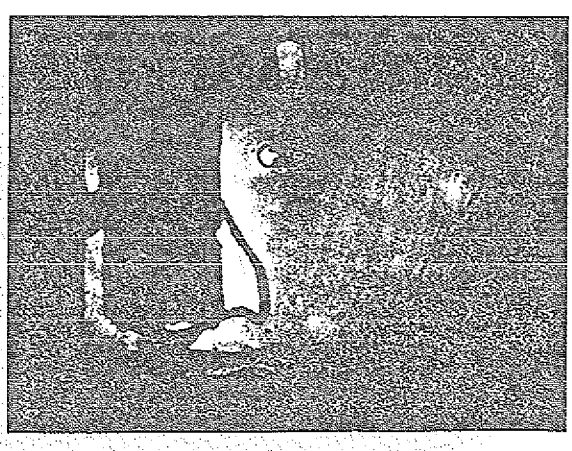

f) 20L O_2

Fig. 6.7: LEED pictures with an electron energy of 159 eV. a) and b) clean Cu (100); c) 5ML Co / Cu (100) clean; d) - f) after exposure of 4, 10, 20L O_2 at room temperature, respectively.

To identify the structure in the photoemission spectra in the second oxidation stage, we additionally studied the oxidation process by photoemission with different photon energies. By varying the photon energy one can expect several changes in the photoemission spectra, even if the surface is not well ordered. The escape depth for the photoelectrons changes because the mean free path of the electrons in solids varies with their kinetic energy, see chapt. 3. It has a minimum of about 3 Å at ≈ 40 eV kinetic energy [Seah 79], therefore photoemission is more surface sensitive at a photon energy of hν = 45 eV (with a work function of 5 eV, the electrons coming from emission near the Fermi energy have nearly 40 eV kinetic energy) than at lower or higher photon energies. Another aspect is that the intensity of the peaks depends on the cross sections of the photoemission process. Table 6.1 shows the atomic cross sections (Mbarn) for the photoionization process for copper, cobalt and oxygen at selected photon energies. The atomic cross section can approximately be taken also for solids, but only for a qualitative analysis.

hν (eV)	16.7	21.2	26.8	40.8	80.0	132.3	151.4
Cu 3d	6.449	7.553	8.190	9.934	8.712	5.139	4.441
Co 3d		4.356	5.917	8.738	7.154	3.719	2.907
O 2p	10.43	10.67	9.772	6.816	2.064	0.5772	0.4037
Co/O		0.41	0.61	1.28	3.47	6.44	7.2

Table 6.1: Atomic subshell photoionization cross sections (Mb = 10^6 barns) for Cu and Co 3d and O 2p shells at selected photon energies after Yeh and Lindau [Yeh 85] The bottom line shows the Cobalt 3d to oxygen 2p ratio.

From this table one sees that Co and Cu have quite the same cross sections, especially at about 40 eV, where they both have their maximum of ≈ 9 Mb. But the oxygen cross section shows a different behavior. Its maximum is observed at about 20 eV photon energy and it decreases rapidly with increasing photon energy. By looking at the Co/O ratios of the cross sections one expects in spectra of 20-30 eV photon energy a dominating oxygen emission, in spectra of ≈ 40 eV photon energy a slightly dominating Co emission and at 130-150 eV photon energy a totally dominating Co emission of the oxidized Co surface.

We can use this behavior of the photoionization cross sections to identify the origin of the structures in the photoemission spectra.

In our case we want to know which structures belong to Cobalt and which to oxygen. Therefore we study the oxidation process in the following at different photon energies.

The oxidation process studied with photoemission at 18 eV photon energy is represented in Fig 6.8.

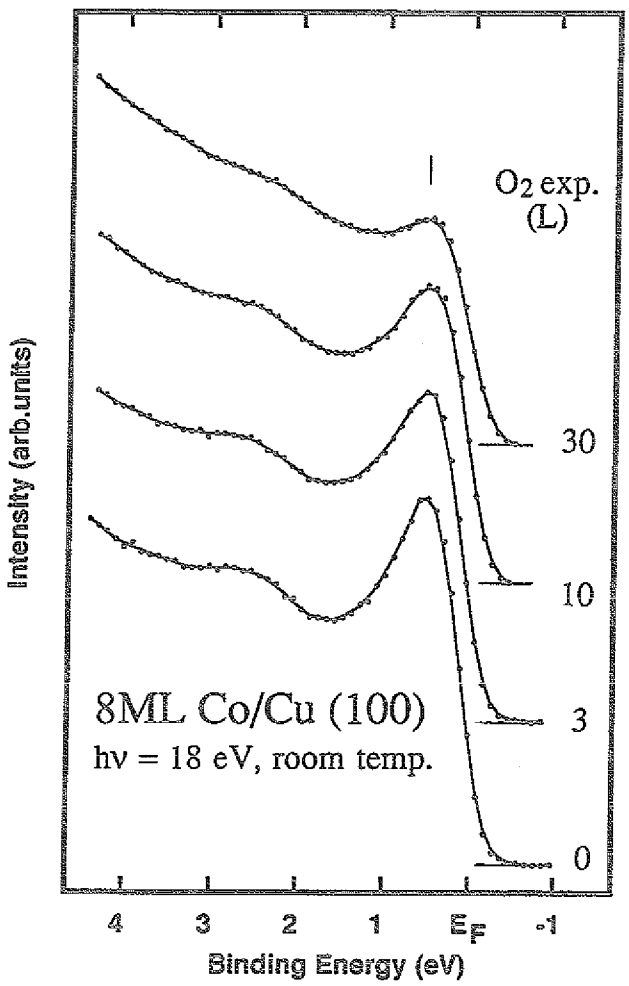

Fig. 6.8: Spin integrated spectra of 8ML Co/Cu(100) at 18 eV photon energy after different oxygen exposures at room temperature.

The feature at 2-3 eV binding energy in the spectrum of the clean sample comes from the Cu substrate while the peak near the Fermi energy is due to Co 3d emission. The main change in the spectra after O_2 exposure is a decrease of the Co 3d emission; but even at high exposures there is still a peak visible at the same binding energy, in contrast to the oxidation process watched at 45 eV photon energy. This might be due to emission from deeper lying Co layers, that are not affected by the oxidation. Varying the photon energy up to 28 eV, as shown in fig. 6.9 one can clearly identify a broad oxygen induced feature at ≈ 5.8 eV binding energy that dominates the spectrum, as expected from the small Co/O cross section ratio at this photon energy.

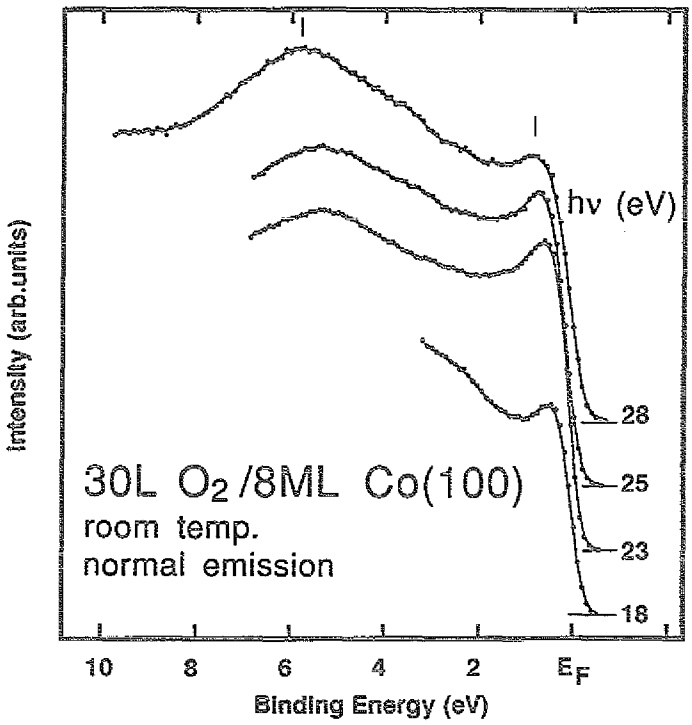

Fig. 6.9: Spin integrated spectra of 30L / Co (100) with different photon energies at normal electron emission.

This changes dramatically if one goes to a photon energy of 138 eV, at which we present the oxidation process in Fig. 6.10.

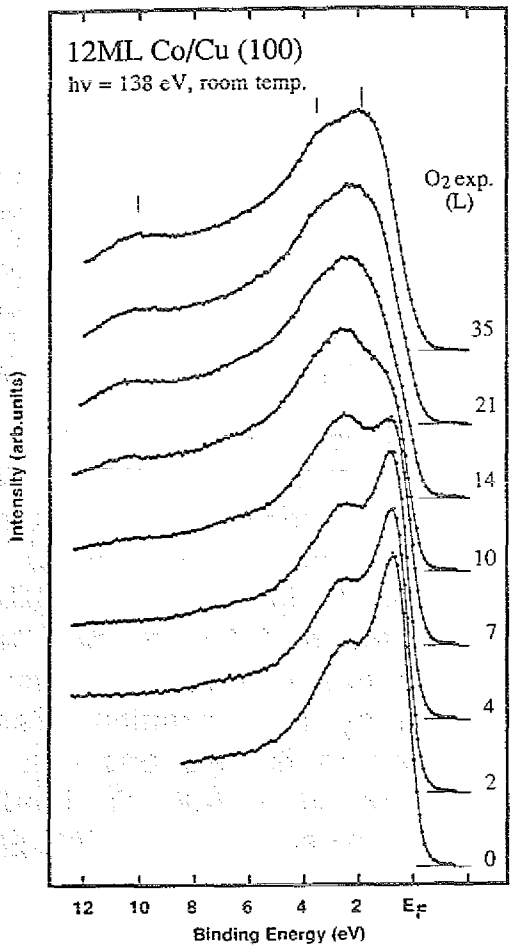

Fig. 6.10: Spin integrated spectra of 12 ML Co/Cu(100) at 138 eV photon energy at normal electron emission for different oxygen exposures at room temperature.

Again the peak near the Fermi level in the clean spectrum is due to Co 3d emission while the shoulder at 2-3 eV comes from the Cu substrate. The development of the spectra after oxygen exposure shows qualitatively the same behavior as in Fig 6.2. Again one can identify two stages, below and above ≈ 7 L. The main difference with respect to the spectra taken at 45 eV photon energy is that there is nearly no structure seen in the spectra between 4 and 8 eV binding energy, in both oxidation stages, while the other peaks described in Fig. 6.2 are clearly seen.

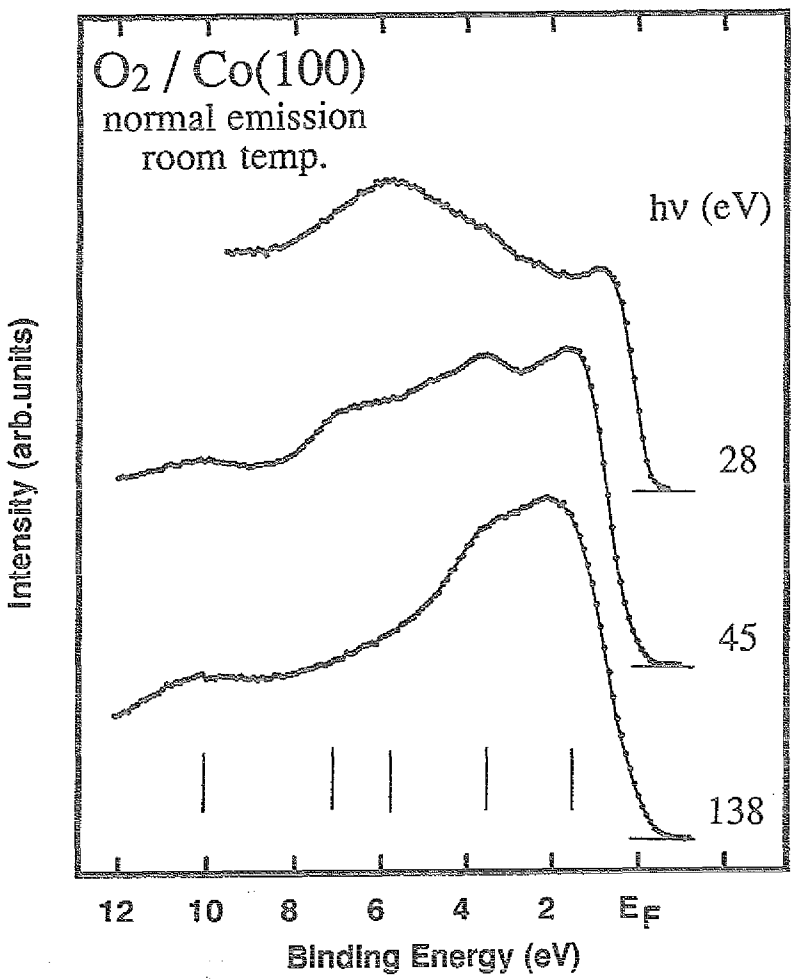

Fig. 6.11: Spin integrated spectra of room temperature oxidized Co surfaces at 28, 45 and 138 eV photon energy. (spectra taken from fig. 6.9, 6.4 and 6.10, respectively)

In Fig. 6.11 we show a comparison between the spectra of the oxidized Co surface at 28, 45 and 138 eV photon energy. One can clearly see that the structure at ≈ 6 eV binding energy dominates the spectra at lower photon energy, while the other structures dominate at higher photon energies. This is a strong indication that the peaks at 1.9, 3.8 and 10 eV binding energy are due to emission from Cobalt, while the structure at 4 - 8 eV binding energy mostly corresponds to oxygen 2p emission. But there must also be emission coming from Co in this region, otherwise the intensity in the 138 eV spectrum would be less in this energy region.

As Matsuyama et al. [Matsuyama 81] identified two different oxidation products on hcp Co at room temperature (→ CoO) and at 120 K (→ Co_3O_4), we also studied the oxidation process at low temperature. In Fig. 6.12 we report the photoemission spectra measured for oxygen exposure at 150 K with a photon energy of 45 eV. The spectra up to 5 L are very similar to those measured at room temperature for the surface ordered adsorption stage. New features appear in the spectra for oxygen exposures above 5L. We attribute these changes to a second reaction stage with formation of a surface oxide phase different from that at room temperature.

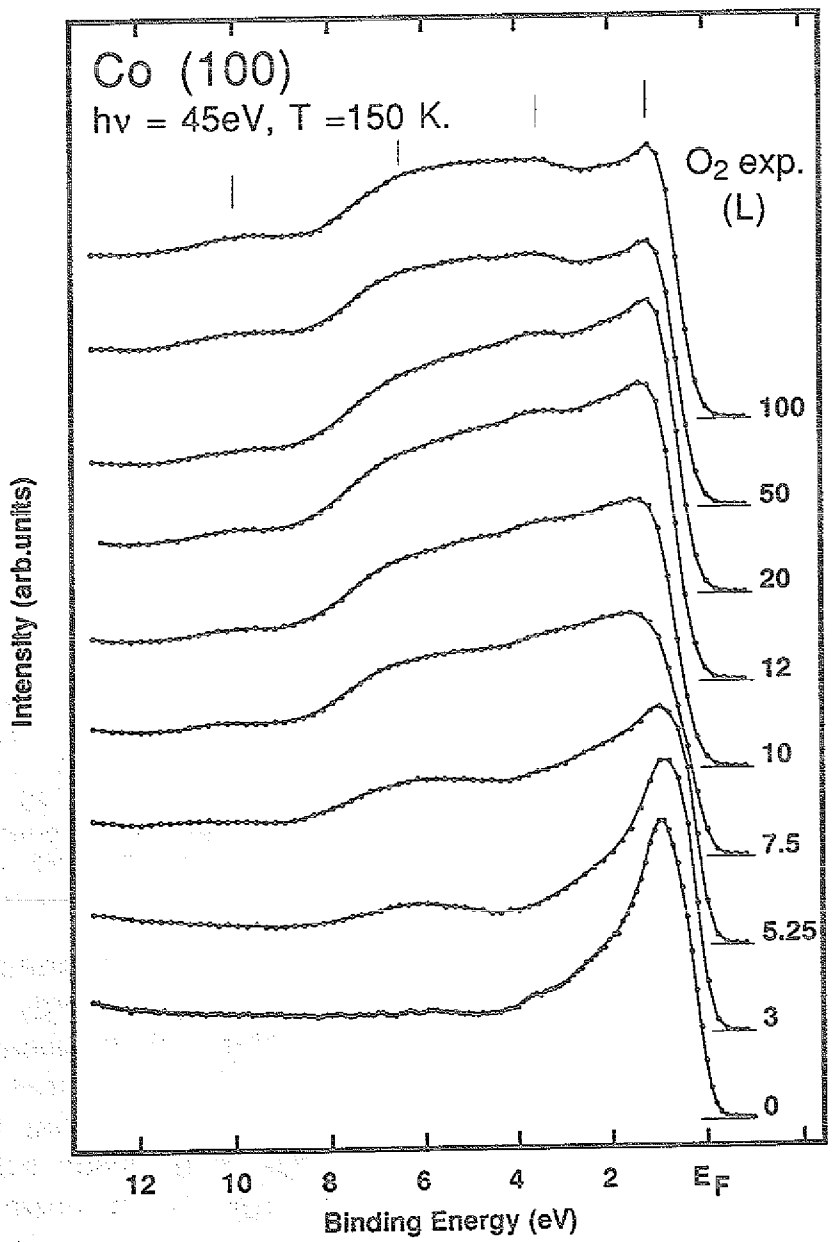

Fig. 6.12: Spin integrated spectra of the oxidation process of 14 ML Co/Cu(100) at T = 150 K taken with a photon energy of 45 eV at normal electron emission.

For a further characterization of the structure of the oxidized surface, we took a set of spectra of this sample with photon energies near the Co 3p threshold energy of ≈ 60 eV, see Fig 6.13, where one expects resonance effects in the Co states but not in the oxygen (see text to fig 5.12 or ref. [Jeng 91]). A problem is that going above the threshold energy also the broad Co MNN Auger peak with ≈ 53 eV kinetic energy appears in the spectrum, that makes the interpretation more complicated. But nevertheless one can see that the emission of the 10 eV satellite becomes stronger above 60 eV photon energy, which is a further evidence for this peak belonging to Co.

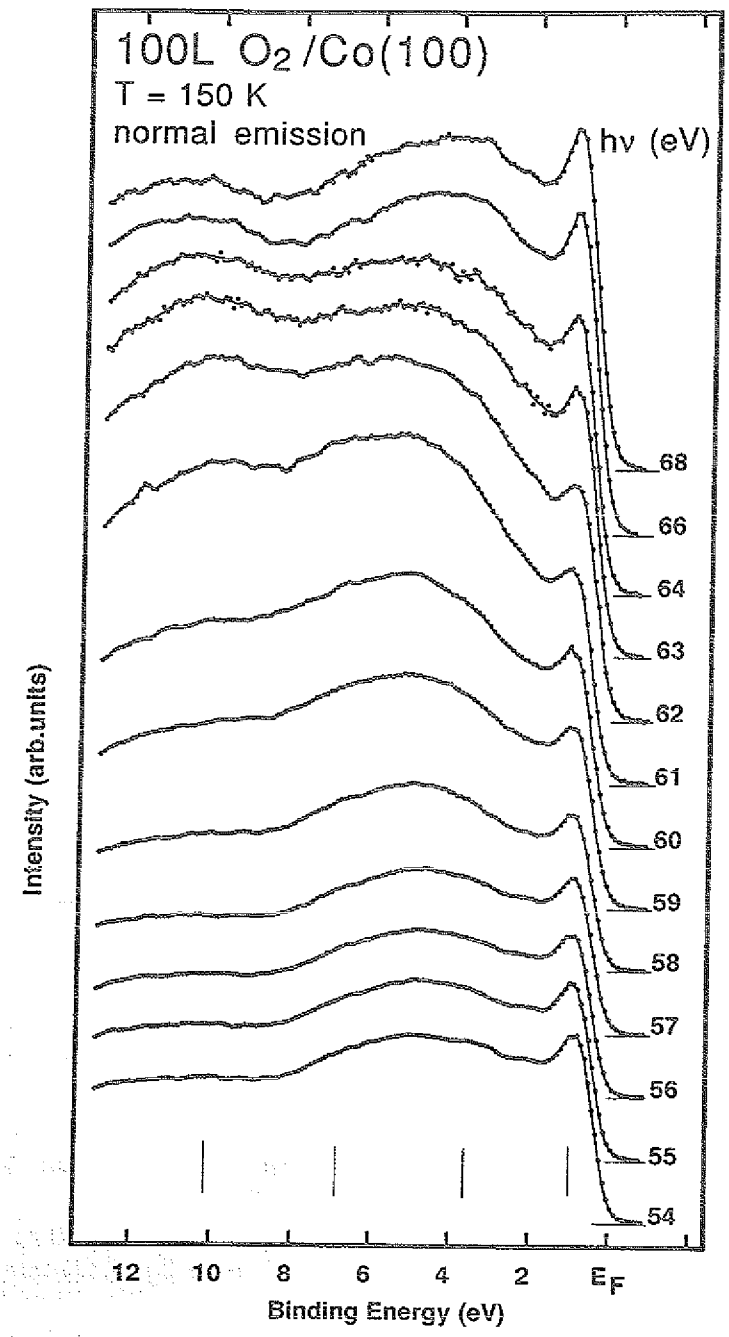

Fig. 6.13: Spin integrated spectra of the at 150 K oxidized Co film (14 ML Co/Cu(100)) for different photon energies near the Co 3p threshold energy of ≈ 61 eV at normal electron emission.

Based on the discussion above about the oxygen reaction of the Co (100) surface, we identify the second oxidation stage as the formation of a surface oxide phase that is different for oxidation at room temperature and at low temperature. This identification seems unambiguous if the spectra obtained for high oxygen exposures are compared to those of the bulk monooxide, CoO for the room temperature (RT) oxidation and of the bulk Co_3O_4 for the oxidation at 150 K (low temperature (LT)) [Jugnet 79].

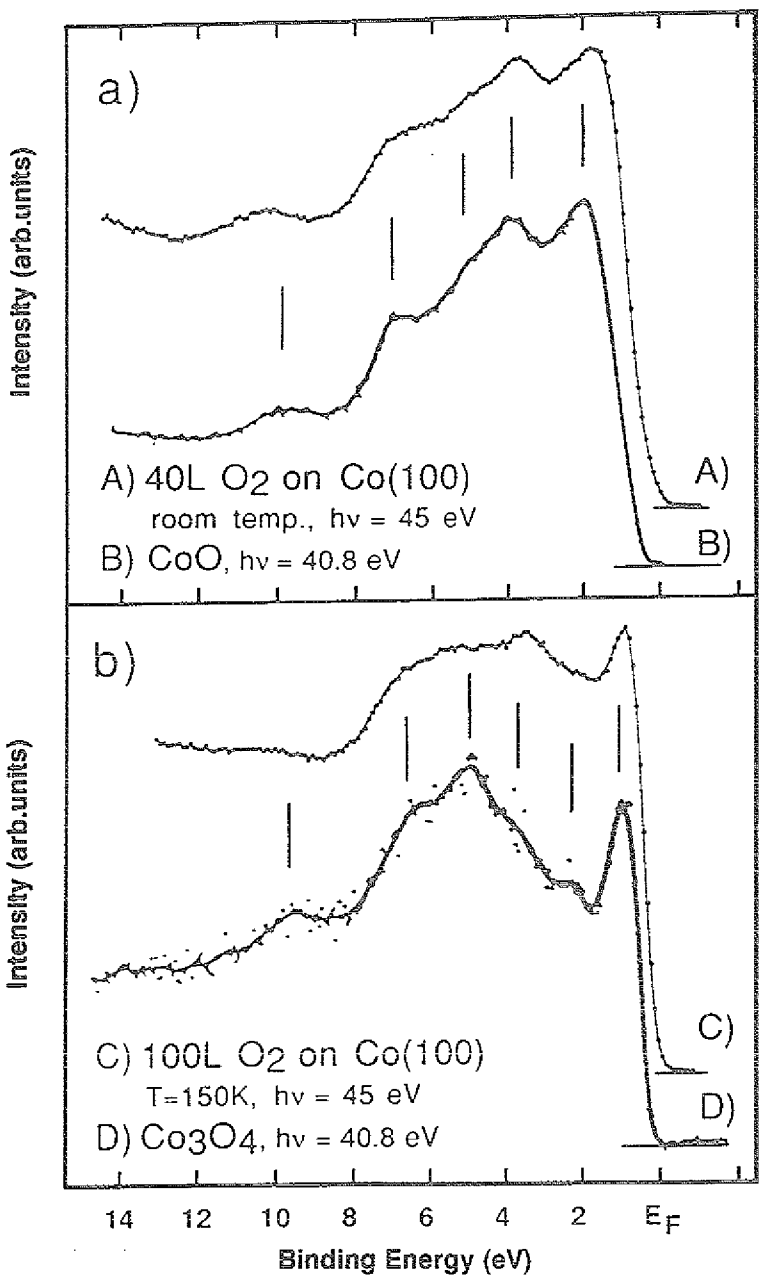

Fig. 6.14: Comparison of spectra with saturated oxygen exposure on 14 ML Co/Cu(100) with bulk CoO and Co_3O_4 spectra of ref [Jugnet 79].
a) spectrum with oxygen exposure at room temperature (see fig. 6.4) compared to a bulk CoO spectrum. b) spectrum with oxygen exposure at T = 150 K (see fig. 6.12) compared to a bulk Co_3O_4 spectrum.

Fig. 6.14 shows that all the spectral features have the same binding energy and a very similar overall shape in the two systems. According to ref. [Kim 75], [Jugnet 79], [Mackay 89], [Jeng 91] and [Elp 91] the peaks in the CoO spectrum are identified as follows: The peaks at 1.8 and 3.8 eV binding energy origin from Co 3d emission, while the structure around 5.5 eV is due to O 2p emission. The identification of the 7 eV structure is not obvious. According to ref [Kim 75], [Mackay 89] and [Jeng 91] it is assigned to O 2p and according to ref. [Jugnet 79] to Co 3d. The 10 eV satellite arises from monopole charge transfer (shakeup) transition (O 2p $\rightarrow$ Co 3d), accompanying photoemission in the Co 3d shell; for further discussion see ref. [Kim 75] and [Elp 91]. The peaks in the Co_3O_4 spectrum are identified according to ref [Jugnet 79] as Co 3d emission at 1.1, 2.5 and 6.7 eV , as O 2p emission at 3.7 and 5 eV and again as a Co satellite at 10 eV binding energy. Although the energy positions of the Co_3O_4 spectrum and the spectrum of oxygen exposure at low temperature fit very well, the overall shape of these curves do not fit as well as the curves in Fig 6.13 a). The peak at 1.1 eV binding energy and its shape is reproduced very well in both spectra, but the 5 eV peak of the Co_3O_4 is hardly seen in the LT spectrum. On the other hand the peak at 3.7 eV in the LT spectrum is only a shoulder in the Co_3O_4 spectrum. There might be several reasons responsible for these differences. The spectra are not taken under exactly the same conditions, for example different photon energies and different polarization of the light are used, a bulk oxide on the one hand and an oxide of only a few layers on the other hand, so it is more surprising, that the shapes of the CoO and RT spectra are so similar. But there is also the possibility that the LT spectrum does not only belong to a single oxide phase but a mixture of different oxides. This is not surprising because in our experiment the reaction of oxygen with the Co surface is not an equilibrium reaction. Here the kinetics of the system are more important and also diffusion of oxygen into the bulk must be taken into account.

We conclude that probably most of the oxide phase in the LT spectrum belongs to the building of Co_3O_4 on the surface because of the overall agreement in these spectra especially with the characteristic shape of the peak at 1.1 eV binding energy; but there might also be some portion of different oxide phases inside. The oxide phase in the RT spectrum is clearly identified as CoO.

b) Spin Resolved Spectra.

We present here the spin dependent results of the oxidation of a 14 ML Co film at room temperature and at 150 K.

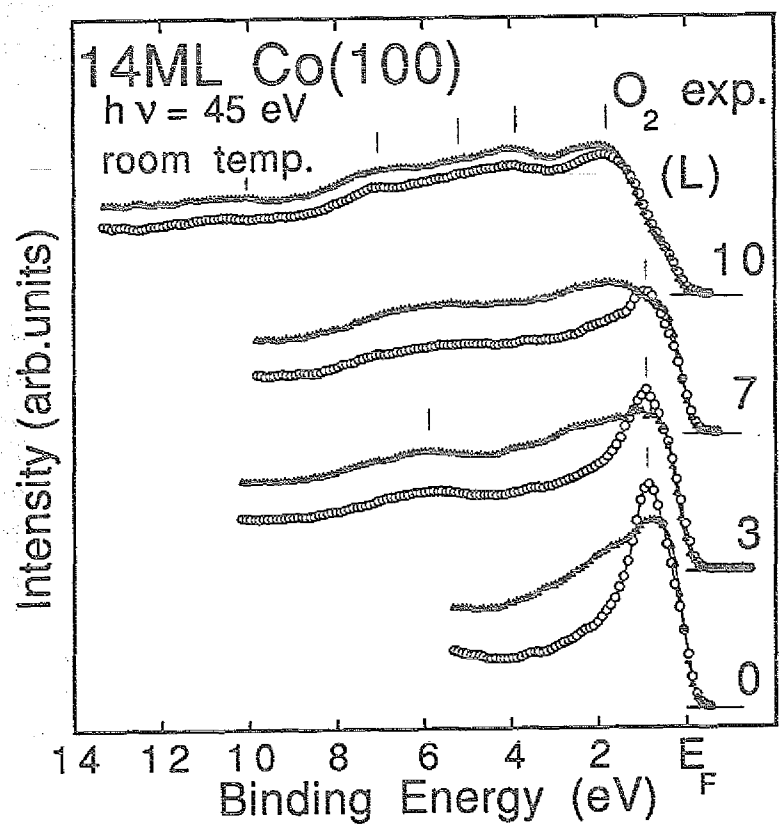

Fig. 6.15: Spin resolved spectra of 14 ML Co/Cu(100) taken in normal emission with s-polarized light of 45 eV photon energy. The spectra for different oxygen exposures at room temperature are shown. The filled triangles (▲) correspond to emission from majority and the open circles (o) to minority electron spin-direction, respectively.

Fig. 6.15 shows spin resolved spectra taken in normal emission with 45 eV photon energy and oxygen exposures at room temperature up to 10 L. The filled triangles (Δ) correspond to emission from majority and the open circles (o) to minority spin direction, respectively. The clean Co spectrum has already been discussed in chapter 5. The peak at 0.9 eV binding energy in the minority spin spectrum is due to emission from the $\Delta_5(\downarrow)$ band near the Γ - symmetry point. The structure in the majority spectrum is broader because there are two features in it, the $\Delta_5(\uparrow)$ state (near Γ) at about 2.4 eV binding energy and another peak near the Fermi energy that cannot be explained as a direct transition in the bulk bandstructure and shows no dispersion with $k_\perp$. After an oxygen exposure of 3 L, when the oxygen forms a c(2x2) superstructure on the surface, the spectrum shows remarkable changes. The Co

minority peak at 0.9 eV binding energy is slightly suppressed, while its shape and position remains the same. The structure of the majority spectrum changes more drastically. The peak at lower binding energy is reduced more than the $\Delta_5(\uparrow)$ emission at 2.4 eV binding energy, so that this feature becomes more pronounced than in the clean spectrum. This is again an evidence for the interpretation of the surface nature of the majority peak near the Fermi energy. Besides the fact that it shows no dispersion by changing $k_\perp$ and that it has no corresponding state in the bulk band structure, it is also strongly sensitive to contamination. These points show, that this peak is most probably a surface state or surface resonance.

At about 5.8 eV binding energy there is the oxygen induced peak that corresponds to the first oxidation phase as discussed above. This peak grows in both spin channels. In Fig. 6.16 the region of this peak is shown again, with the polarized background subtracted.

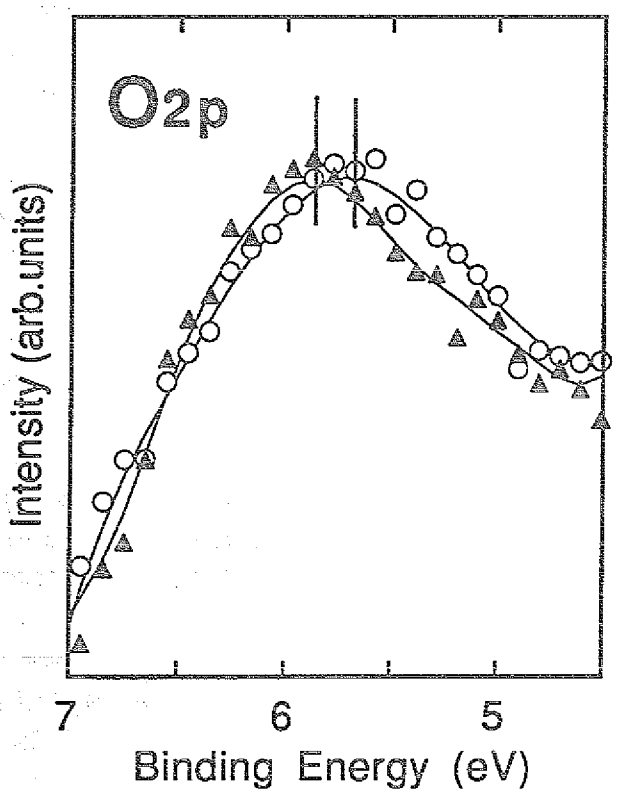

Fig 6.16: spin resolved spectra of 14 ML Co/Cu(100) after 3L oxygen exposure at room temperature in the region of the Oxygen 2p emission. It shows an induced exchange splitting of (0.2 ± 0.1) eV. The filled triangles (▲) correspond to emission from majority and the open circles (o) to minority electron spin-direction, respectively.

The intensity of this peak is equal in both spin directions, but it shows an exchange splitting of (0.2 ± 0.1) eV. The maximum in the majority peak is at 5.9 and in the minority peak at 5.7 eV binding

energy. Since the majority components of the adsorbate induced features are at higher binding energy than the minority components it may be deduced that the magnetic moments on the adsorbate are ferromagnetically aligned with the bulk moments of the substrate. This has also been seen with oxygen adsorbed on Fe (001) [Johnson 88], for which theory predicted an induced magnetic moment at the oxygen sites [Huang 85]. Whilst the exchange split photoemission peaks suggest the presence of a magnetic moment on the adsorbate they do not allow any quantitative determination of the magnitude of that moment [Johnson 90]. But we can conclude from the induced magnetic moment in the adsorbate site, that also the topmost Co layers carry a magnetic moment, i.e. there are no magnetically "dead layers" on the Co surface induced by the adsorbate.

The spectrum in Fig. 6.15 for 7 L oxygen exposure shows already the transition from the first (O-c(2x2) superstructure) to the second (surface-oxide formation) reaction phase. The oxygen induced emission is much broader than in the 3 L spectrum and an exchange splitting is not observable any more. The oxygen features consist already of more than one peak, but they still doe not show the structure of the CoO spectrum. The minority Δ_5 peak near the Fermi energy is still clearly visible but its intensity is even more suppressed, while the majority feature near E_F has changed its shape more drastically. From the surface peak there is now only a shoulder left and one can see the formation of a new feature around 2 eV binding energy. The spectrum for 10 L oxygen exposure is again different. Its shape has already nearly the form of the oxygen saturated spectrum, that means this spectrum corresponds mostly to the second reaction phase. One can clearly identify the peaks at 1.9 and 3.8 eV binding energy due to the Co 3d emission, the broad structure around 6 eV binding energy from the oxygen and the onset of the 10 eV satellite. All these peaks are visible in both spin channels, there is only a nearly constant small polarization left due to inelastically scattered electrons. Because the peaks are in both spin channels and at the same binding energy, we conclude that the surface of the oxidized sample is not ferromagnetically ordered any more. But this is not surprising, because CoO is antiferromagnetic with a Néel temperature of about 293 K, only little below room temperature (298 K). So the oxide might even be already in the paramagnetic phase. We can not distinguish from our spectra between antiferromagnetic and paramagnetic phases.

In Fig. 6.17 we plot the difference of the spin polarization measured at 2.4 eV and at 0.9 eV binding energy (P(2.4 eV) - P(0.9 eV)) as a function of oxygen exposure at room temperature. The

spectra show the largest polarization difference between these two energies, because these are the peak positions of the majority and minority Δ_5 state, respectively. The polarization-difference for the clean spectrum (0 L oxygen exposure) has a maximum value of 35 %. With increasing oxygen exposure the polarization decreases drastically in an exponential way (solid curve), even in the first oxidation stage below 7 L. At 10 L exposure there is only 5 % polarization-difference left and for exposures above 20 L it nearly vanishes. This drastic decrease even in the first reaction stage (below 7 L) is surprising, because we have seen that the oxygen overlayer has an induced magnetic moment in this range of exposure. Because we have measured the polarization in this figure only for two points in the spectrum, we cannot conclude too much from this figure. But nevertheless, by looking at the spectra of fig. 6.15 on can see that in the whole spectra the polarization decreases very fast. This behavior can be interpreted in the way that besides the ordered c(2x2) structure also islands of CoO are forming on the surface even in the first reaction stage. This has also been reported for the Ni(001) oxidation reaction [Godby 85], where islands of NiO are formed on the surface, while the oxygen is mainly adsorbed in a c(2x2) superstructure. This will be investigated in more detail below studying the core level photoemission.

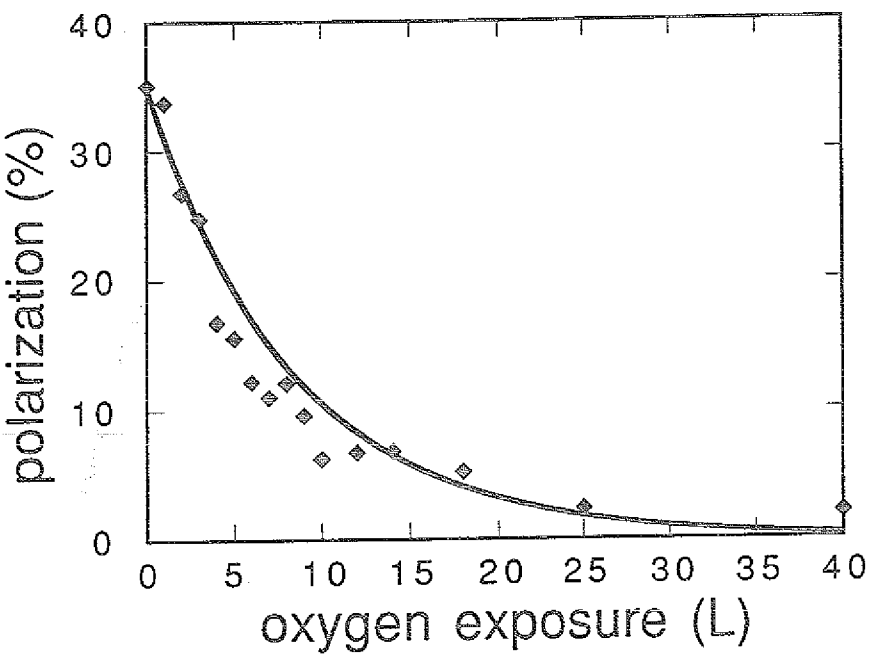

Fig 6.17: Difference of the polarization at 2.4 eV and at 0.9 eV binding energy of photoemission spectra (P(2.4 eV) - P(0.9eV)) of 12ML Co/Cu(100) versus oxygen exposure at room temperature. The corresponding (spin integrated) spectra are shown in fig 6.2.

The spin resolved photoemission study of the oxidation reaction at low temperature (150 K) is shown in Fig. 6.18. The spectra for the clean sample and for oxygen exposure of 5 and 35 L are shown. The spectrum of the clean sample is identical to that at room temperature. After 5 L oxygen exposure the reaction at low temperatures is already in the region between the first and the second reaction phase. The spectrum is totally different from the clean one and the polarization is nearly lost, but it still does not have the typical shape that corresponds to the second reaction phase. The formation of the 10 eV satellite can be seen as an indication for the second phase, but the typical structure at about 1 eV binding energy is not developed yet. This 1 eV peak is developed at higher oxygen exposures, as shown in the spectrum for 35 L. Here the polarization is totally lost, the spectra of both spin channels are identical, indicating again that the surface oxide has no more long ranged ferromagnetic order.

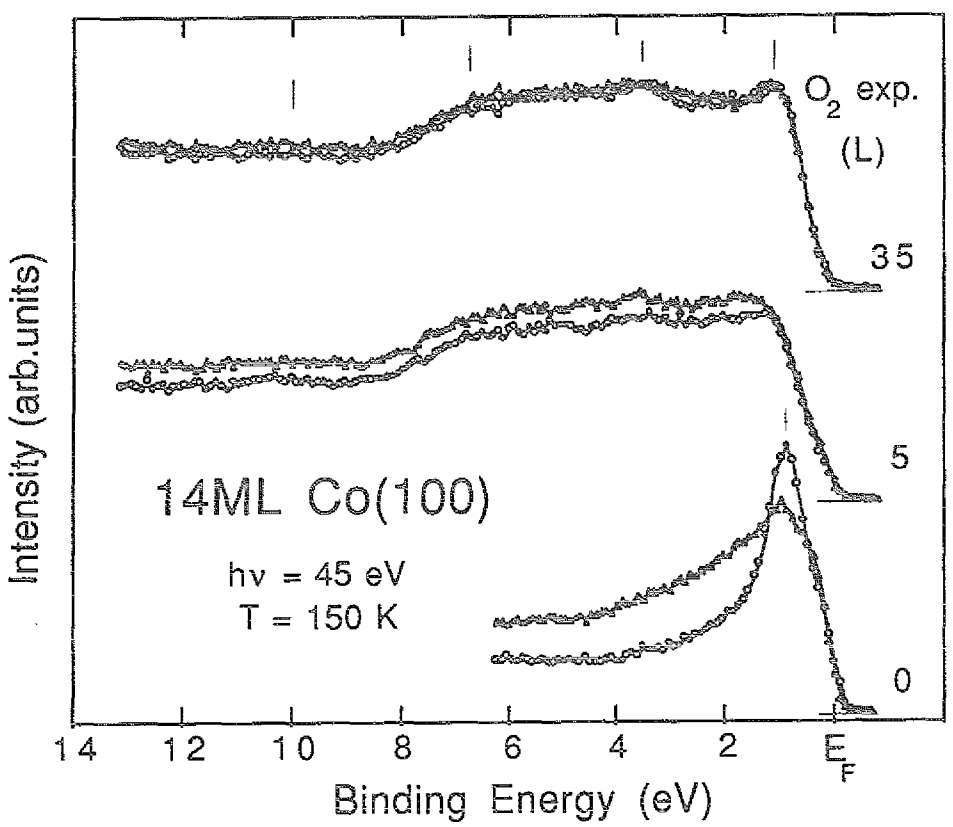

Fig. 6.18: spin resolved spectra of 14 ML Co/Cu(100) taken in normal emission with s-polarized light of 45 eV photon energy. The spectra for different oxygen exposures at T =150 K are shown. The filled triangles (Δ) correspond to emission from majority and the open circles (o) to minority electron spin-direction, respectively

Now we present valence band photoemission studies of the oxidation reaction of Co films of less than 10 ML thickness, all taken at room temperature. We want to see if the electronic structure behaves different to the reaction of the thick layers. One can expect a different behavior for several reasons. i) The Co films become ferromagnetic in the thickness range of 2 ML ii) We found a quantum size effect in the Co films up to 5 ML thickness and iii) the reaction kinetics are different for thin films than for bulk systems iv) Weber et. al. [Weber 90] found that the Curie temperature of ultrathin Fe films increases due to small oxygen exposures. All these points might also have an effect on the chemical reactivity and on the spin dependent electronic structure during the reaction of the films.

We report both spin integrated and spin resolved spectra of the oxidation for different Co film thicknesses. If not mentioned otherwise, all of the following spectra are taken in normal emission with 45 eV photon energy. In Fig. 6.19 we show the spectra of the oxidation reaction of a 1 ML Co film on Cu (100).

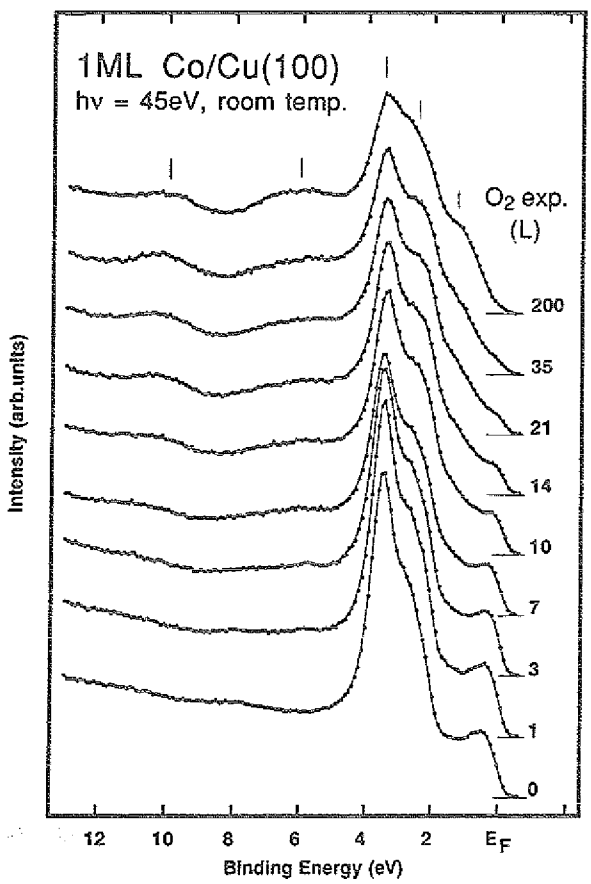

Fig. 6.19: Spin integrated photoemission spectra of 1 ML Co/Cu(100) taken at 45 eV photon energy at normal emission after different oxygen exposures at room temperature

In the spectrum of the clean sample one can identify emission coming from Co 3d states near the Fermi energy, the shoulder at about 2.5 eV binding energy originates from emission both from Co and from the Copper substrate. The dominant peak at 3.5 eV binding energy is due to emission from the Copper Δ_5 state at the Γ symmetry point. At higher binding energies there is only a slightly increasing background-emission visible. During the oxidation process, the spectra change quite in a similar way as for the thick films discussed above. The intensity of the Co peak near the Fermi energy decreases with the oxygen exposure, while new structures appear at higher binding energies. The shoulder at 2.5 eV binding energy becomes stronger, while the Cu peak at 3.5 eV remains at the same position with the same shape. At about 6 eV a new structure develops and at 10 eV binding energy there grows again a satellite.

At high exposures one can also see the development of a new structure (shoulder) at about 1.2 eV binding energy. But it is not easy to identify the oxidized sample from the spectrum as being CoO or Co_3O_4. The structures at 6 and 10 eV binding energy one can find in both oxides and the features at lower binding energies do not fit very well to the spectra of the two oxides, even if one subtracts the Cu peak at 3.5 eV. There are no spin resolved spectra of this sample, because the long range in plane ferromagnetic order starts only above 2 ML thickness, as discussed in chapter 5.

For a Co thickness of 2.5 ML we show the spin integrated spectra in Fig 6.20.

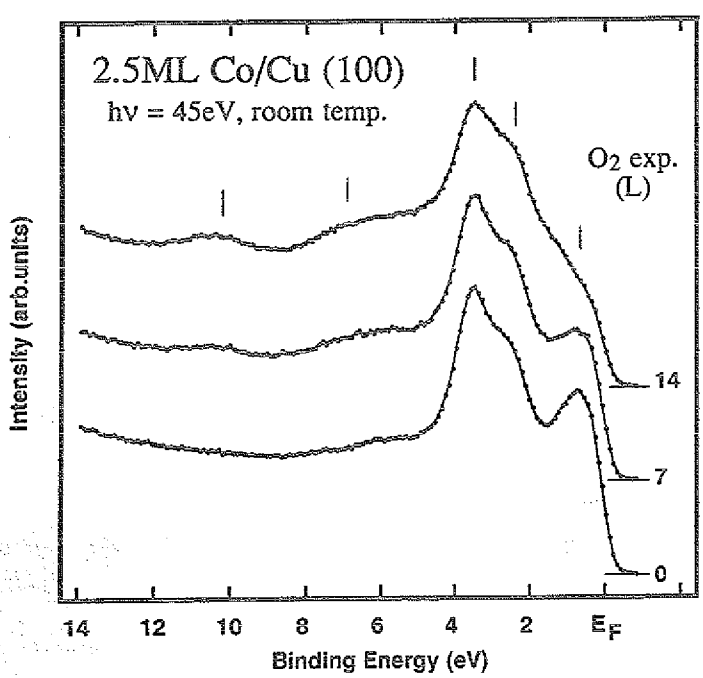

Fig. 6.20: Spin integrated photoemission spectra of 2.5 ML Co/Cu(100) taken at 45 eV photon energy at normal emission after different oxygen exposures at room temperature

The spin resolved spectra of the oxidation process of 2.5 ML we present in Fig. 6.21.

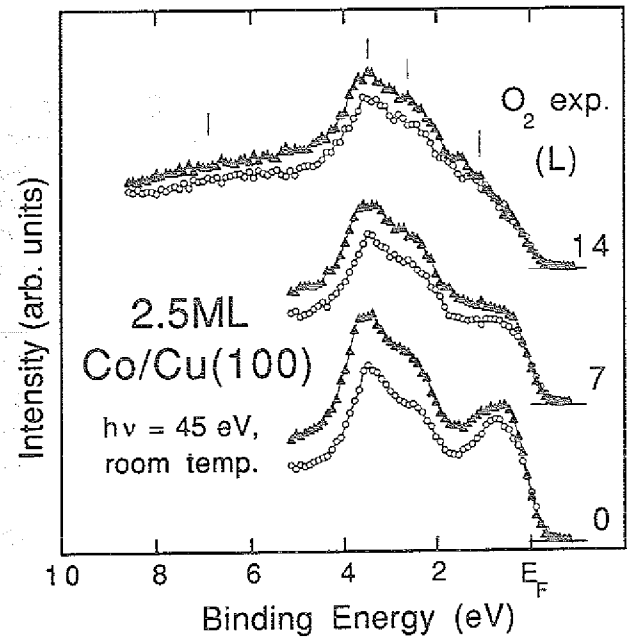

Fig. 6.21: Spin resolved photoemission spectra of 2.5 ML Co/Cu(100) taken at 45 eV photon energy at normal emission after different oxygen exposures at room temperature. The filled triangles (▲) correspond to emission from majority and the open circles (o) to minority electron spin-direction, respectively.

The spectra for the clean sample and for oxygen exposures of 7 and 14 L are shown. The development of the spin integrated spectra during the oxidation process is comparable to that of the 1 ML film. So we can also not identify the oxidized phase clearly. The spin resolved spectra show a loss of spin polarization with increasing O_2 exposure, indicating again that the surface of the oxidized sample is not ferromagnetic any more.

The spectra of 4 ML thickness with oxygen exposure up to 7 L are shown spin integrated in Fig. 6.22 and spin resolved in Fig 6.23.

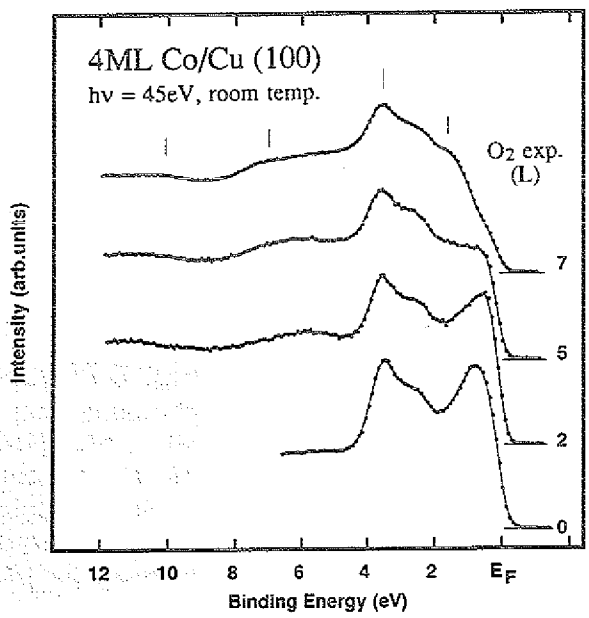

Fig. 6.22: Spin integrated photoemission spectra of 4 ML Co/Cu(100) taken at 45 eV photon energy at normal emission after different oxygen exposures at room temperature.

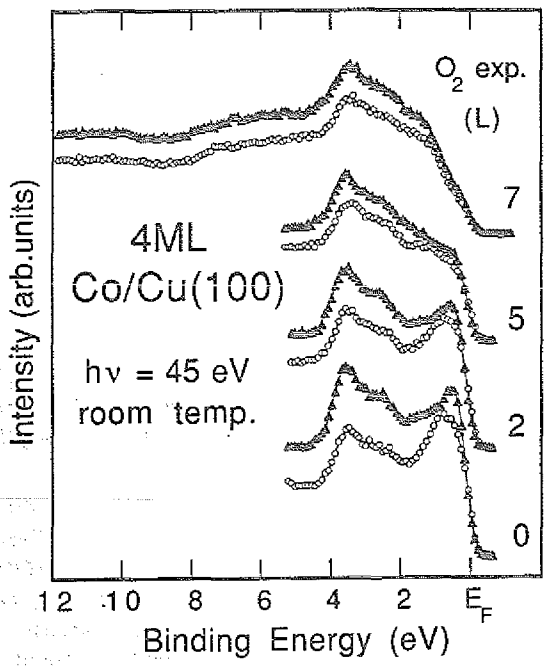

Fig. 6.23: Spin resolved photoemission spectra of 4 ML Co/Cu(100) taken at 45 eV photon energy at normal emission after different oxygen exposures at room temperature. The filled triangles (▲) correspond to emission from majority and the open circles (o) to minority electron spin-direction, respectively.

Here the spectrum of the oxidized sample has more clearly the structure of the CoO spectrum. The structure of the oxygen derived feature between 5 and 7 eV binding energy and especially the feature at 1.7 eV binding energy fit quite well to the CoO spectrum. The spin resolved spectra also show an analogous behavior to those of the thick layer. At low exposures (2 L), the Co emission near the Fermi energy is suppressed in both spin channels, but the majority feature is changing more its shape than the minority feature. Above 5 L exposure both spin channels show the same structure, there is only a small background polarization left.

The spectra of the oxidation of 5 ML Co, shown in Fig. 6.24, show again more likely the development of CoO than of Co_3O_4, but it is still not as clear as for the thick film.

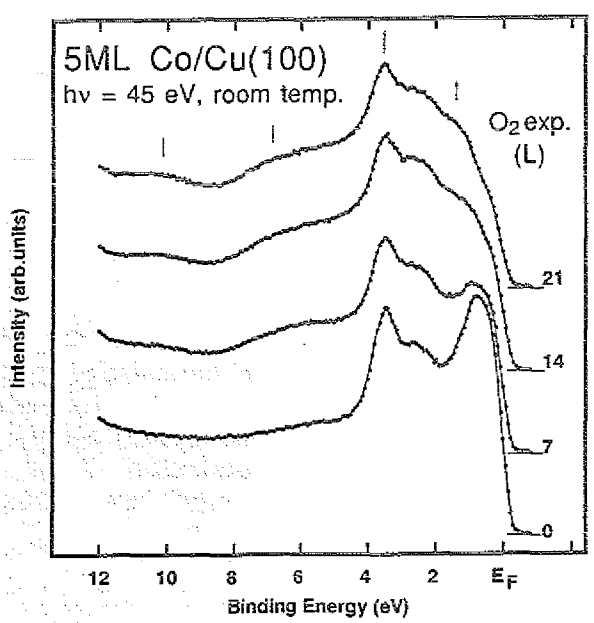

Fig. 6.24: Spin integrated photoemission spectra of 5 ML Co/Cu(100) taken at 45 eV photon energy at normal emission after different oxygen exposures at room temperature.

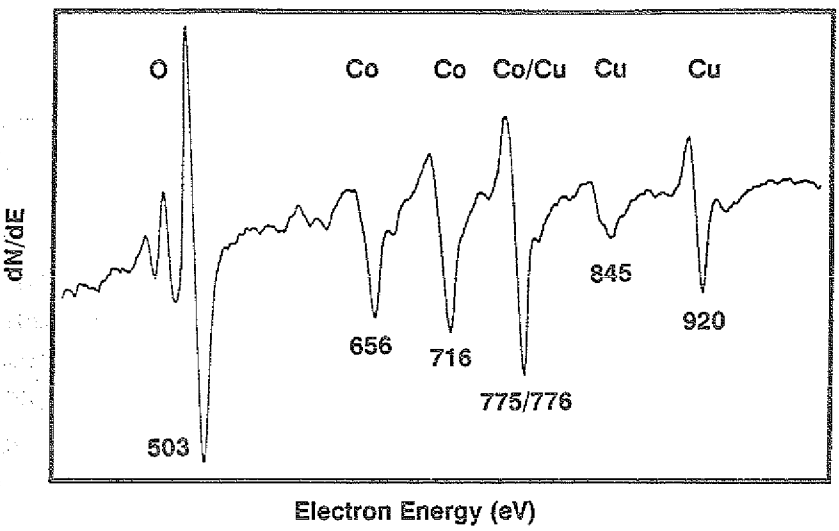

Fig. 6.25: Derivative Auger spectrum (dN/dE) of 40 L O_2 exposure at room temperature on 5 ML Co/Cu(100).

The Auger spectrum of 5 ML Co with an exposure of 40 L oxygen at room temperature is presented in Fig. 6.25. The typical oxygen, Co and Cu peaks with their electron energies are indicated. With this exposure, the oxygen peak at 503 eV dominates over all the other features.

As for the low temperature oxide we can characterize also the oxidized sample at room temperature with the help of resonance effects. An identification of the peaks can be done by varying the photon energy for normal emission again in the range of the 3p threshold energy of about 61 eV. For the low temperature oxidized thick Co-film this is shown already in fig. 6.13. In fig. 6.26 we show a set of spectra of a 6 ML Co film after 30 L oxygen exposure at room temperature.

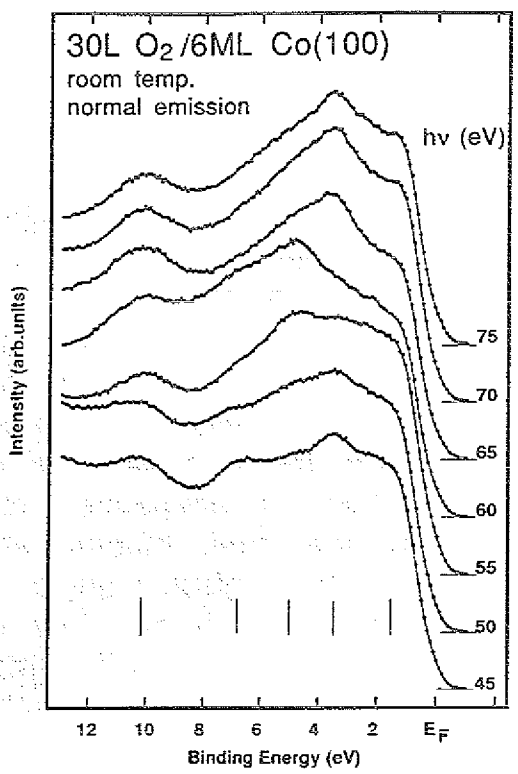

Fig. 6.26: Spin integrated photoemission spectra of 6 ML Co/Cu(100) after 30 L oxygen exposure at room temperature taken at normal emission with different photon energies near the Co 3p threshold energy of ≈ 61 eV.

At this range of oxygen exposure the oxidation reaction has come to a saturation. The spectrum shows the overall structure of CoO (see fig. 6.14) only at 1.9 eV binding energy there is not a peak as in the CoO spectrum but a shoulder. In fig. 6.26 the photon energy is changed from spectrum to spectrum by 5 eV. This is too coarse for observing clearly resonance effects and also the spectra are not normalized, but a qualitative understanding can be derived anyway. The spectra of 55 and 60 eV photon energy are quite different from the others. At 60 eV photon energy the peak at 5 eV binding energy is dominating above all other structures in the spectrum, while it is hardly visible in the spectra of lower or higher photon energies. As explained already above, one expects resonance effects of the Cobalt states near the threshold energy, while the emission from oxygen states should not change much in this photon-energy region. The situation becomes more complicated because above the threshold energy of the Co 3p states there also appears an Auger peak in the spectrum that makes the interpretation harder. Nevertheless, from this set of spectra, one can say that the emission near 5 eV binding energy has a different origin than the emission in the other part of the spectrum. As this region has already been identified as oxygen 2p emission, the peaks at 3.8 and 1.9 eV binding energy are probably due to Co emission, while the origin of the emission at 6.7 eV binding energy still is not clear, because in all the spectra, independent of the photon energy, there is a shoulder seen at this energy. About the 10 eV satellite we cannot deduce much from this picture; because of the arbitrary way of normalizing the spectra we cannot determine whether its intensity changes upon variation of the photon energy.

6.3 Core Level Spectroscopy

We report here the effect of oxygen reaction with fcc Cobalt on the Co 3p core levels. The interpretation of core level photoemission is quite different from that of valence band states. While valence band states are extended through the whole crystal, the core levels have an atomic character. For core levels, such as the 3p states of the 3d transition metals, a description with a reciprocal lattice and a bandstructure like in the case of the valence band does not make much sense, as the binding energies are independent of the k value of the electrons. This means also that their binding energies do not shift, varying the photon energy or the emission angle. So, the binding energies of core levels are very well defined (they only consist of different peaks (multiplet splitting) due to the different quantum numbers of the corresponding electrons in each level), they

can only change due to chemical bonding, which is well known as 'chemical shift', or indirectly through hybridization effects in the valence band (e.g. at the surface). Fig. 6.27 shows the spin integrated spectrum of the Cu 3p state of the clean Cu substrate taken at 138 eV photon energy after subtraction of a constant background of inelastically scattered electrons. The Cu 3p state consists of $3p_{3/2}$ emission at 75.1 eV and $3p_{1/2}$ emission at 77.3 eV binding energy.

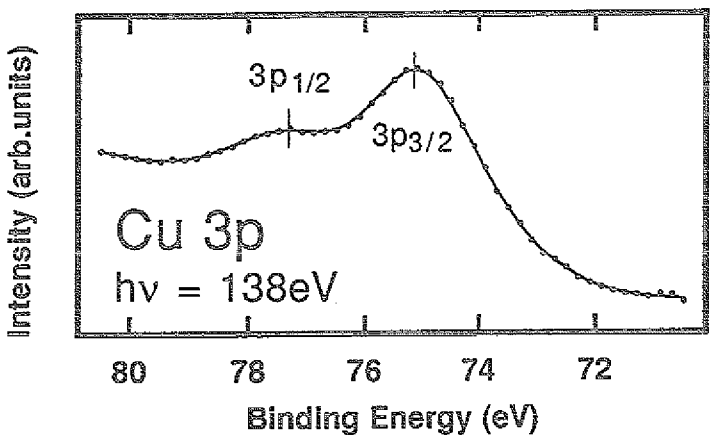

Fig. 6.27: Spin integrated photoemission spectra of the Cu 3p core levels taken at 138 eV photon energy. A constant inelastically background is subtracted. Binding energies: Cu $3p_{3/2}$ = 75.1 eV and Cu $3p_{1/2}$ = 77.3 eV.

After evaporation of 14 ML Cobalt, the Cu emission has vanished and one can see the Co 3p states at 58.9 eV binding energy, shown in fig. 6.28 at 133 and 138 eV photon energy.

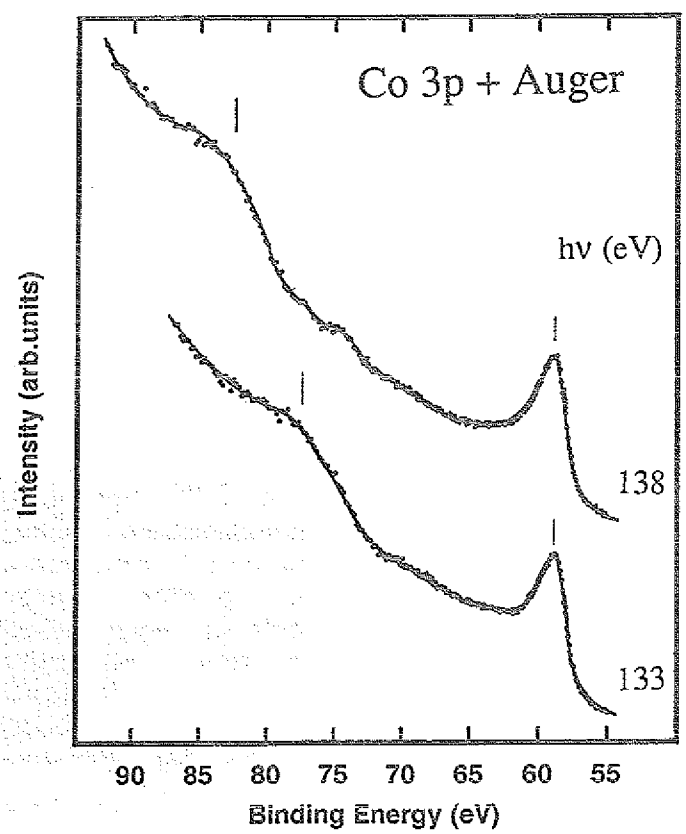

Fig. 6.28: Spin integrated photoemission spectra of Co 3p core levels at 58.9 eV binding energy and Co MNN Auger emission at 53 eV electron energy taken with 133 eV and 138 eV photon energy. A constant inelastically background is subtracted.

In this figure one can also see a 5 eV broad structure between 75 and 80 eV binding energy that shifts to higher binding energies by the same amount as the photon energy changes; so at 133 eV photon energy, its maximum is at about 78 eV "binding energy" and at 138 eV photon energy at about 83 eV "binding energy". This structure corresponds to the Co MNN Auger emission with a constant electron kinetic energy of about 53 eV. Because the spectra are always shown relative to the Fermi energy, the Auger peak shifts in the spectrum varying the photon energy.

The following spectra are taken at a photon energy of 138 eV, where the Auger feature is far away from the Co 3p structure in the spectrum, and in the figures, a constant background of inelastically scattered electrons is subtracted. In fig. 6.29 we show spin integrated spectra of the Co 3p core level and its changes induced by reaction with oxygen at room temperature.

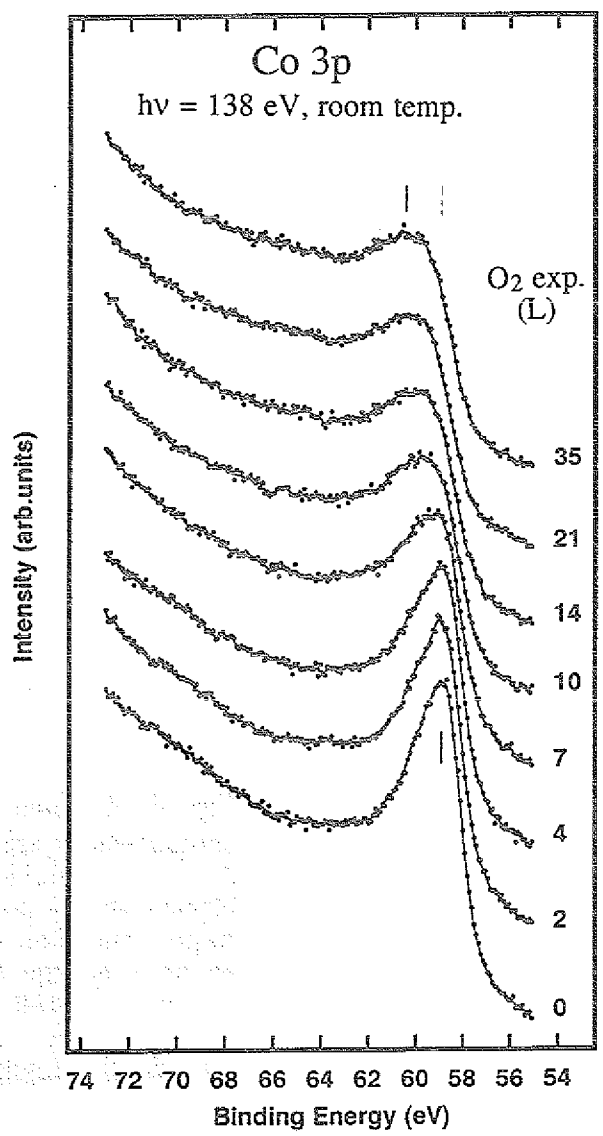

Fig. 6.29: Spin integrated photoemission spectra of Co 3p core levels taken at 138 eV photon energy for different oxygen exposures at room temperature. A constant inelastically background is subtracted in each spectrum.

The sample preparation and gas exposure conditions are the same as for the valence band measurements, the thickness of the Co film is 14 ML. For the clean sample the spectrum has one peak at 58.9 eV binding energy, which corresponds both to $3p_{1/2}$ and $3p_{3/2}$ state emission. This set of spectra gives further support for the distinction we have made between the two reaction stages. Also the 3p spectra display as a function of oxygen exposure two distinct behaviors. Up to 6 L few changes can be observed in the 3p lineshape, as it is expected for the Co weakly interacting with the surface adsorbed oxygen. Above 7 L a 1.5 eV chemically shifted component emerges, corresponding to the formation of surface CoO. The value of the chemical shift is in agreement with published data for CoO [Kim 75], where the Co 3p state in CoO is found to be at 60.4 eV binding energy. But also the entire shape of the spectrum changes in the range of 60 to 70 eV binding energy and new features appear due to oxygen exposure, but they are too broad to be distinguished. This structures can be interpreted according to ref [Kim 75] as emission from multielectron excitations (electron shakeups) and multiplet splittings. So, the development of the core level spectra is again a very good identification of the room temperature oxidized sample with CoO, by a chemical shift of the Co 3p state of 1.5 eV to higher binding energy. Fig. 6.30 shows again the spectra of the clean and the oxidized Co surface in the energy range from 55 to 90 eV binding energy, where one can also see the Co Auger peak at about 82 eV binding energy. For the oxidized sample, the Auger peak at this energy is much broader, indicating that the electronic structure of Co has changed during the oxidation.

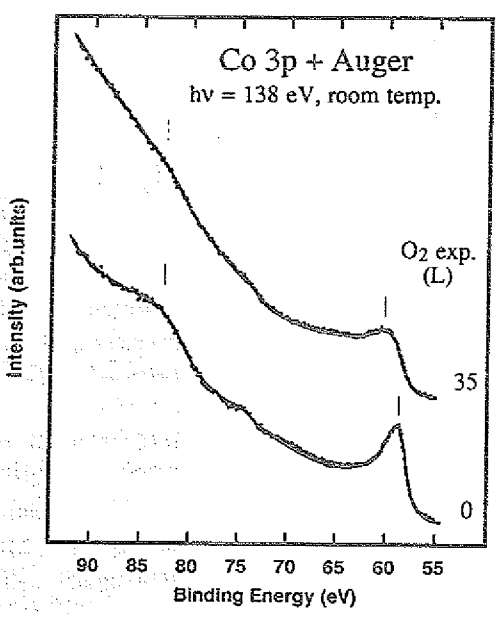

Fig. 6.30: Spin integrated photoemission spectra of Co 3p core levels and Co MNN Auger emission taken at 138 eV photon energy. The spectra for the clean sample and after 35 L oxygen exposure at room temperature are shown. A constant inelastically background is subtracted in each spectrum.

Now we want to discuss the influence of the oxidation on the Co 3p core level in spin resolved spectra. The spin resolved measurements of core levels is problematic because of the low count rate due to the small photoionization cross section, see table 6.1. Therefore one needs a high photon flux for photon energies above 100 eV. This is only available at an Undulator-beamline of a synchrotron. Until now for the clean surfaces, there are only spin and energy resolved measurements of the 3p core levels of Fe, Co and Ni [Kachel 89], [Carbone 88] and of the Fe 3s core level [Carbone 90]. The influence of adsorbates on the spin dependent electronic structure of the core levels has been investigated until now only for the Fe 3p level with oxygen chemisorption [Sinkovic 90].

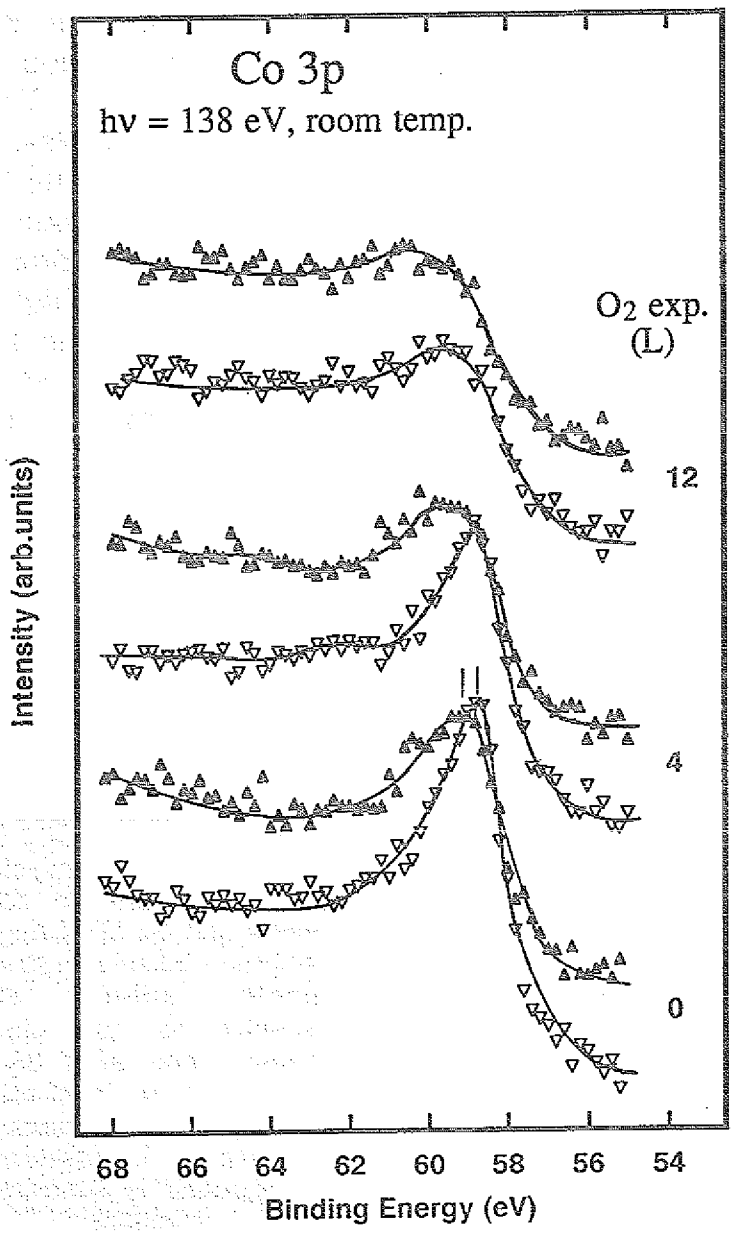

Fig. 6.31: Spin resolved photoemission spectra of the Co 3p core levels taken at 138 eV photon energy. The spectra for different oxygen exposures at room temperature are shown. A constant inelastically background is subtracted in each spectrum. The filled triangles (▲) correspond to majority and the open triangles (▽) to minority spin electrons, respectively.

In fig. 6.31 we report the spin resolved spectra of the Co 3p state of the clean sample and after 4 and 12 L oxygen exposure at room temperature. The spectrum of the clean sample shows an overall dominating majority emission due to the polarization of the background. Only at the Co 3p peak the minority emission dominates. The Co 3p peak is split by (0.3 ± 0.15) eV. After 4 L oxygen exposure the minority peak decreases, but remains at the same energy position. The majority structure becomes broader, new structures appear at about 60 eV binding energy, the minority peak gets less in intensity but its shape remains the same. This slightly different behavior in both spin directions of the Co 3p level might be an indication that the oxide, which is formed already in the first reaction stage, is magnetically ordered, while this ordering gets lost with higher oxygen exposures.

In the region of 61 - 68 eV binding energy the spectra in both spin channels are still quite similar to those of the clean sample, because with 4 L oxygen exposure one is still mainly in the first reaction stage.

The spectra for 12 L oxygen exposure show already the feature for the second reaction stage. They have nearly the same structure in both spin channels, only the majority spectrum is still higher in intensity due to background polarization of not reacted Co layers underneath. This is similar to what we have observed in the spin resolved valence band spectra. The additional emission between 60 and 68 eV binding energy is not polarized, it appears simultaneously in both spin channels. This shows again that the surface oxide has no more long range ferromagnetic order.

6.4 Summary of Chapter 6

In this chapter we discussed the reaction of oxygen with ultrathin fcc Co (100) films at room temperature and at lower temperature (150 K).

At room temperature with oxygen exposures up to about 6 L, oxygen forms a c(2x2) superstructure on top of the Co surface. The corresponding oxygen 2p state at about 6 eV binding energy in the photoemission spectrum is exchange splitted by (0.2 ± 0.1) eV, indicating the possibility of an induced magnetic moment in this overlayer parallel to the bulk Co film. From this we also conclude that the topmost Co layers cannot be magnetically "dead" due to the oxygen adsorption in the first reaction stage. With higher oxygen exposures the formation of a surface oxide starts, accompanied by a rapid decrease of the surface ordering and the spin polarization in the photoemission spectra. The photoemission spectra change drastically their shape; while the Co 3d emission near the Fermi energy vanishes. New structures at higher binding energies appear due to oxide Co 3d states, oxygen 2p states and a Co satellite at 10 eV binding energy. For oxygen exposures higher than 20 L we identified the creation of CoO at the surface, which does not order ferromagnetically any more. For the various reaction stages we found an overall behavior similar to the oxidation of a Ni(100) surface.

The Co 3p core levels show a chemical shift of 1.5 eV due to reaction with oxygen for high exposures

Below 4 ML Co film thickness, the resulting structure for the oxidized sample could not be identified with CoO or another oxide unambiguously, but for Co films above 4 ML thickness we identified CoO as the reaction product.

At low temperature (150 K) exposure we observed a similar behavior of the oxygen reaction in the photoemission spectra, only the second reaction stage is observed already at lower exposures (because of the higher sticking coefficient at this temperature) and the spin polarization in the photoemission spectra vanishes faster. The reaction product for high exposures was identified to be mainly Co_3O_4.

7. Summary and Outlook

The aim of this work was to investigate the spin dependent electronic structure of ultrathin fcc Co films and the changes induced by reaction with oxygen. The experiments were carried out using spin- and angle resolved photoemission spectroscopy; the samples were characterized additionally by LEED and Auger spectroscopy. The layer dependent electronic structure of the Co overlayers has also been calculated with spin resolved band structure calculations using the FLAPW (full potential linearized augmented plane waves) method.

Co grows epitaxially in the layer by layer mode on the Cu (100) substrate adapting the fcc structure of Cu at least up to 15 atomic layers. The hybridization of the Cu substrate with the Co overlayers was found to be weak, the position and shape of the Cu-peaks in the photoemission spectra did not significantly change with the deposition of Co overlayers. We found long range ferromagnetic ordering in the plane of the surface at room temperature only for Co film thicknesses above 2 ML.

A band structure determination of the Cu(100) substrate with angle resolved photoemission could verify the dispersion of the Cu Δ_5 band in the Γ - X direction of the Brillouin zone.

Co films of more than 5 ML thickness displayed bulk electronic properties. We determined the bandstructure in the Γ - X direction and compared it to calculations of the fcc Cobalt bandstructure with Co in the Cu lattice constant. The binding energies of the majority and minority Δ_5 band at the Γ - high symmetry point and consequently their exchange splitting of (1.55 ± 0.15) eV are found to be in good agreement with the calculation. Also the dispersion of the bands could be measured well. An additional majority peak at about 0.6 eV binding energy does not fit to the bulk bandstructure. We identified this peak to correspond to a surface state or surface resonance.

We found an enhanced value of the exchange splitting at the center (Γ - point) of the Brillouin zone in Co layers with a thickness below 5 monolayers. The enhancement is 25 ± 5 % in the monolayer regime. We interpret this enhancement as a quantum size effect, where the bulk-wavefunctions are modified by the reduced dimensionality of the system.

We compared our experimental results on the enhanced exchange splitting with spin polarized band structure calculations for various Co films on Cu(100). We found (i) an enhancement of the magnetic moment strictly limited to the first Co layer; (ii) a proportionality between the enhancement of magnetic moment and exchange splitting. Taking this proportionality into account we give experimental evidence of an enhancement of the ground state local moment in the monolayer of about 25±5 %.

In the reaction of oxygen with Co films we could identify different reaction stages. At low exposures, oxygen adsorbes dissociatively in an ordered c(2x2) structure. The chemical interaction between the adsorbate and the substrate manifests itself through a reduction of the 3d surface state emission near E_F. The oxygen 2p bands exhibit an induced exchange splitting of (0.2 ± 0.1) eV at the center of the surface Brillouin zone. From this we conclude the possibility of an induced magnetic moment in the oxygen overlayer and the topmost Co layers cannot be magnetically "dead" due to the oxygen adsorbation in this reaction stage.

With higher oxygen exposure, corresponding to the formation of a CoO surface phase, the photoemission spectra show evidence for strong correlation effects in the electronic structure. A satellite appears about 10 eV below E_F in the spectra. The formation of the CoO surface oxide phase is accompanied by a decrease of the photoelectron spin polarization revealing the quenching of the surface ferromagnetic order. At low temperatures (150 K) and high exposures of O_2 the formation of another surface oxide phase was observed which again has a different electronic structure. This low temperature phase was identified to be mainly Co_3O_4.

The study of the oxidation reaction for different Co film thicknesses showed the same overall behavior for all Co films. For film of at least 4 ML Co thickness we could identify the building of a CoO oxide phase at room temperature. For thinner films we could not identify the reaction product for high oxygen exposures clearly.

In the future it would be interesting to study quantum size effects also at different conditions like in sandwich- or multilayer systems, or for instance on the (111) plane of Co. In the latter we expect a slightly smaller effect than on the (100) plane because of the larger atomic density in this plane. The influence of different adsorbates like hydrogen, sulfur or carbon monoxide on the spin dependent electronic structure of the Co surface is also of great interest because for Co there is still a lack of information compared to Fe or Ni.

References

[Abraham 87] D.L.Abraham and H.Hopster, Phys. Rev. Lett. 58, 1352 (1987)

[Allenspach 85] R.Allenspach, M.Taborelli, and M.Landolt, Phys. Rev. Lett. 55, 2599 (1985)

[Arnott 89] M.Arnott and W.Allison, Physica B 161 (1989)

[Ashcroft] N.W.Ashcroft, N.D.Mermin, *Solid State Physics*, Saunders College, Philadelphia, 1976

[Aukrust 64] E.Aukrust and A.Muan, Trans. Aime 230, 378 (1964)

[Baibich 88] M.N.Baibich, J.M.Broto, A.Fert, F.N.v.Dau, F.Petroff, P.Eitenne, G.Creuzet, A.Friederich, and J.Chazelas, Phys. Rev. Lett 61, 2472 (1988)

[Beier 88] T.Beier, H.Jahrreiss, D.Pescia, Th.Woike, and W.Gudat, Phys. Rev. Lett. 61, 1875 (1988)

[Binasch 89] G.Binasch, P.Grünberg, F.Saurenbach, and W.Zinn, Phys. Rev. B 39, 4828 (1989)

[Blügel (1)] S.Blügel, to be published

[Blügel 89] S.Blügel, B.Drittler, R.Zeller, and P.H.Dederichs, Appl. Phys. A 49, 547 (1989)

[Briggs 83] *Practical Surface Analysis*, ed. by D.Briggs and M.P.Seah, J.Wiley & Sons 1983

[Brookes 91] N.B.Brookes, Y.Chang, and P.D.Johnson, Phys. Rev. Lett. 67, 354 (1991)

[Burdick 63] G.A.Burdick, Phys. Rev. 129, 138 (1963)

[Capellmann 86] *Metallic Magnetism*, ed. by H.Capellmann, Springer Berlin 1986

[Carbone 88] C.Carbone and E.Kisker, Sol. State Comm. 65, 1107 (1988)

[Carbone 90] C.Carbone, T.Kachel, R.Rochow, and W.Gudat, Z. Phys. B - Condensed Matter 79, 325 (1990)

[Cardona 79] *Photoemission in Solids I and II*, ed. by M.Cardona and L.Ley, Springer Berlin, 1978/79

[Castro 82] G.R.Castro and J.Küppers, Surface Sci. 123, 456 (1982)

[Chappert 88] C.Chappert and P.Bruno, J. Appl. Phys. 64, 5736 (1988)

[Chen 90] C.Chen, Phys. Rev. Letters 64, 2176 (1990)

[Clarke 87] A.Clarke, G.Jennings, R.F.Willis, P.J.Rous, and J.B.Pendry, Surface Science 187, 327 (1987)

[Davis 86] L.C.Davis, *Photoemission from Transition Metals and their Compounds*, J. Appl. Phys. 59(6), R25 (1986)

[Dürr 89] W.Dürr, M.Taborelli, O.Paul, R.Germar, W.Gudat, D.Pescia, and M.Landolt, Phys. Rev. Lett. 62, 206 (1989)

[Ebel 90] H.Ebel, C.Phn, R.Svagera, M.E.Wernle, M.F.Ebel, and A.Jablonski, J. Electron Spectrosc. Relat. Phenom. 50, 109 (1990)

[Eberhardt 80] W.Eberhardt and F.J.Himpsel, Phys. Rev. B21, 5572 (1980)
[Elmers 88] H.J.Elmers, U.Gradmann, Surf. Sci. 193, 94 (1988)
[Elp 91] J.van Elp, J.L.Wieland, H.Eskes, P.Kuiper, G.A.Sawatzky, F.M.F. de Groot, T.S.Turner; Phys. Rev. B 44, 6090 (1991)
[Erice 91] International School of Materials Science and Technology, 21st Course: *Surface and Thin-Film Magnetism*, Erice (Sicily) 1 - 13 July 1991
[Eriksson 91] O.Eriksson, R.C.Albers, and A.M.Boring, Phys. Rev. Lett. 66, 1350 (1991)
[Falicov 90] L.M. Falicov, D.T.Pierce, S.D.Bader, R.Gronsky, K.B.Hathaway, H.J.Hopster, D.N.Lambeth, S.S.P.Parkin, G.Prinz, M.Salamon, I.K.Schuller, R.H.Victora; J. Mater. Res. 5, 1299 (1990)
[Feder 85 (1)] *Polarized Electrons in Surface Physics*, ed. by R.Feder, World Scientific Publishing, Singapore (1985)
[Feder 85 (2)] R.Feder and H.Hopster, Sol. State Comm. 55, 1043 (1985)
[Fu 85] C.L.Fu, A.J.Freeman, and T.Oguchi, Phys. Rev. Lett. 54, 2700 (1985)
[Germar 88] R.Germar, W.Dürr, J.W.Krewer, D.Pescia and W.Gudat, Appl. Phys. A 47, 393 (1988)
[Godby 85] R.W.Godby, G.A.Benesh, R.Haydock, and V.Heine, Phys. Rev. B32, 655 (1985)
[Gonzales 81] L.Gonzales, R.Miranda, M.Salmeron, J.A.Verges, and F.Yndurain, Phys. Rev. B24, 3245 (1981)
[Goodenough 72] *Metallic Oxides,* J.Goodenough in Progress in Solid State Chemistry, ed. by H.Reiss (Pergamon, New York, 1972), Vol. 5, p.145
[Gradmann 74] *Ferromagnetism near Surfaces and thin Films*, U.Gradmann, Appl. Phys. 3, 161 (1974)
[Gradmann 86] U.Gradmann, *Magnetic Surface Anisotropies*, J. M. M. M. 54-57, 733 (1986)
[Greuter 86] F.Greuter, I.Strathy, E.W.Plummer, and W.Eberhardt, Phys. Rev. B 33, 736 (1986)
[Grünberg 90] P.Grünberg, S.Demokritov, A.Fuss, M.Vohl, and J.A.Wolf, J. Appl. Phys. 69, 4789 (1990)
[Heinen 90] W.Heinen, C.Carbone, T.Kachel, and W.Gudat, Vacuum 41, 495 (1990)
[Heinrich 87] B.Heinrich, K.B.Urquhart, A.S.Arrott, J.F.Cochran, K.Myrtle, and S.T.Purcell, Phys. Rev. Lett. 59, 1756 (1987)
[Henrich 83] V.E.Henrich, Progress in Surface Sci. 14, 175 (1983)
[Hermanson 77] J.Hermanson,Solid State Comm. 22, 9 (1977)
[Himpsel 80] F.J.Himpsel, *Experimental Determination of Bulk Band Dispersions*, Appl. Opt. Vol. 19, 3964 (1980)

[Himpsel 83] F.J.Himpsel, *Angle resolved measurements of the Photoemission of Electrons in the Study of Solids*, Advances in Phys. **32**, 1 (1983)
[Himpsel 91] F.J.Himpsel, Phys. Rev. B44, 5966 (1991)
[Huang 85] H.Huang and J.Hermanson, Phys. Rev. B32, 6312 (1985)
[Ibach 77] *Electron Spectroscopy for Surface Analysis*, ed. by H.Ibach, Springer Berlin (1977)
[Jeng 91] S.P.Jeng, Z.Zhang and V.E.Henrich, Phys. Rv. B44, 3266 (1991)
[Johnson 88] P.D.Johnson, A.Clarke, N.B.Brookes, S.L.Hulbert, B.Sinkovic, and N.V.Smith, Phys. Rev B61, 2257 (1988)
[Johnson 90] P.D.Johnson, J. Electron Spectrosc. Relat. Phenomena 51, 249 (1990)
[Jonker 86] B.T.Jonker, K.H.Walker, E.Kisker, G.A.Prinz, and C.Carbone, Phys. Rev. Lett. **57**, 142 (1986)
[Jugnet 79] Y.Jugnet and T.M.Duc, J. Phys. Chem. Solids, 40, 29 (1979)
[Kachel 89] T.Kachel, C.Carbone, W.Heinen, and W.Gudat, BESSY Jahresbericht 1989, 178
[Kerkmann 89] D.Kerkmann, Appl. Phys. A 49, 523 (1989)
[Kern 79] R.Kern, G.de Lay, and J.J.Métois in *Current Topics in Materials Science*, chapt. 3, Vol. 3, ed. by E.Kaldis, North Holland, Amsterdam 1979
[Kessler 85] J.Kessler, *Polarized Electrons.*, 2nd ed., Springer Series on Atoms and Plasmas, Vol.1, Springer Berlin (1985)
[Kim 75] K.S.Kim, Phys. Rev. B, 11, 2177 (1975)
[Kirschner 85] J.Kirschner, *Polarized Electrons at Surfaces*, Springer Tracts in Modern Physics **106**, Springer Berlin 1985
[Kisker 79] E.Kisker, M.Campagna, W.Gudat, E.Kuhlmann, Festkörperprobleme **XIX**, 259 (1979)
[Kisker 85] E.Kisker, K.Schröder, W.Gudat, and M.Campagna, Phys. Rev. B **31**, 329 (1985)
[Kisker/Carbone] E.Kisker and C.Carbone, to be published in *Angle resolved Photoemission*, ed. by S.D.Kevan, Pergamon Press
[Kittel] *Introduction to Solid State Physics*, C.Kittel, J.Wiley & Sons New York, 1986
[Klebanoff 87] L.E.Klebanoff, R.K.Jones, D.T.Pierce, and R.J.Celotta, Phys. Rev. B 36, (1987)
[Kolbas 84] R.M.Kolbas, N.Holonyak, Am. J. Phys. 52, 431 (1984)
[Kündig 69] W.Kündig, M.Kobelt, A.Appel, G.Constabaris, and R.H.Lindquist, J. Phys. Chem. Solids 30, 819 (1969)
[Landolt 89] M.Landolt, *Spin Polarized Auger Spectroscopy from Magnetically Ordered Solids*, in Springer Ser. Surf. Sci. Vol. 18, Springer Berlin 1989
[Li C. 88] C.Li, A.J.Freeman, and C.L.Fu, J. Magn. Magn. Mat. 75, 53 (1988)

[Li C. 90] C.Li, A.J.Freeman, and C.L.Fu, J. Magn. Magn. Mat. 83, 51 (1990)
[Li H. 90] H.Li and B.P.Tonner, Surface Science 237, 141 (1990)
[Liu 88] C.Liu, E.R.Moog and S.D.Bader, Phys. Rev. Lett. 60, 2422 (1988)
[Mackay 89] J.L.Mackay and V.E.Henrich, Phys. Rev. B 39, 6156 (1989)
[Maglietta 78] M.Maglietta, E. Zanazzi, U. Bardi, F.Jona, D.W.Jepsen and P.M.Marcus, Surface Sci. 77, 101 (1978)
[Mankey 90] G.J.Mankey, M.T.Kief, and R.F.Willis, J. El. Spectr. Rel. Phen. 54/55, 501 (1990)
[Matsuyama 81] T.Matsuyama and A.Ignatiev, Surface Sci. 102, 18 (1981)
[Miguel 89] J.J.de Miguel, A.Cebollada, J.M.Gallego, S.Ferrer, R.Miranda, C.M.Schneider, P.Bressler, J.Garbe, K.Bethke, and J.Kirschner, Surf. Sci. 211, 732 (1989)
[Min 86] B.I.Min, T.Oguchi, and A.J.Freeman, Phys. Rev. B 33, 7852 (1986)
[Moruzzi 78] *Calculated Electronic Properties of Metals*, V.L.Moruzzi, J.F.Janak, A.R.Williams, Pergamon New York (1978)
[Musket 82] R.G.Musket, W.McLean, C.A.Colmenares, D.M.Makowiecki, and W.J.Siekhaus, Appl. of Surf. Sci. 10, 143 (1982)
[Noffke priv.] J.Noffke and L.Fritsche, priv. comm.
[Nolting 86] *Quantentheorie des Magnetismus*, Bd. 1 u. 2, W.Nolting, Teubner Stuttgart 1986
[Oepen 90] H.P.Oepen, M.Benning, H.Ibach, C.M.Schneider, and J.Kirschner, J. Magn. Magn. Mat. 86, L137 (1990)
[Ohnishi 83] S.Ohnishi, M.Weinert, and A.J.Freeman, Phys. Rev. B 28, 6741 (1983)
[Pan 88] X.Pan, P.D.Johnson, M.Weinert, R.E.Watson, J.W.Davenport, G.W.Fernando, and S.L.Hulbert, Phys. Rev. B38, 7850 (1988)
[Parkin 90] S.S.P.Parkin, N.More, and K.P.Roche, Phys. Rev. Lett. 64, 2304 (1990)
[Peatman 89] W.Peatman, C.Carbone, W.Gudat, W.Heinen, P.Kuske, J.Pflüger, F.Schäfer, T.Schroeter, Rev. Sci. Instrum. 60, 1445 (1989)
[Pescia 87] D.Pescia, G.Zampieri, M.Stampanoni, G.L.Bona, R.F.Willis, and F.Meier, Phys. Rev. Lett. 58,933 (1987)
[Pescia 89] *Magnetism in Ultrathin Films*, ed. by D. Pescia, Appl. Phys. A49 (Solid Surfaces), No. 5 and 6, 437 (1989)
[Pescia 90] D.Pescia, D.Kerkmann, F.Schumann, and W.Gudat, Z. Phys. B 78,475 (1990)
[Plummer 82] E.W.Plummer and W.Eberhardt, *Angle resolved Photoemission as a Tool for the Study of Surfaces,* Adv. Chem. Phys. 49, 533 (1982)
[Przybylski 87] M.Przybylski and U.Gradmann, Phys. Rev. Lett. 59, 1152 (1987)

[Rae 64] A.U.Rae, Surface Sci. 1, 319 (1964)
[Richter 85] R.Richter, J.G.Gay, and J.R.Smith, Phys. Rev. Lett. 54, 2704 (1985)
[Roth 64] W.L.Roth, J. Phys. Chem. Solids, 25, 1 (1964)
[Schmitt 85] W.Schmitt, H.Hopster, and G.Güntherodt, Phys. Rev B 31, 4035 (1985)
[Schmitt 87 (1)] W.Schmitt, K.-P.Kämper, and G.Güntherodt, Surf. Sci. 189/190, 741 (1987)
[Schmitt 87 (2)] W.Schmitt, K.-P.Kämper, and G.Güntherodt, Phys. Rev B36, 3763 (1987)
[Schneider 90 (1)] C.M.Schneider, P.Bressler, P.Schuster, J.Kirschner, J.J.de Miguel, and R.Miranda, Phys. Rev. Letters 64, 1059 (1990)
[Schneider 90 (2)] C.M.Schneider, J.J.de Miguel, P.Bressler, P.Schuster, R.Miranda, and J.Kirschner, J. El. Spectr. Rel. Phen. 51, 263 (1990)
[Schönhense 88 (1)] G.Schönhense, M.Donath, U.Kolac and V.Dose, Surf. Sci. 206, l888 (1988)
[Schönhense 88 (2)] G.Schönhense, M.Getzlaff, C.Westphal, B.Heidemann, and J.Bansmann, J. de Physique, Colloque C8, nº 12, C8-1643 (1988)
[Seah 79] M.P.Seah and W.A.Dench, Surface and Interface Analysis, 1, 2 (1979)
[Shen 90] Z.X.Shen, C.K.Sih, O.Jepsen, W.E.Spicer, I.Lindau and J.W.Allen, Phys. Rev. Lett., 64, 2442 (1990)
[Sinkovic 90] B.Sinkovic, P.D.Johnson, N.B.Brookes, A.Clarke, and N.V.Smith, Phys. Rev. Lett. 65, 1647 (1990)
[Stampanoni 87 (1)] M.Stampanoni, A.Vaterlaus, M.Aeschlimann, and F.Meier, Phys. Rev. Lett. 59, 2483 (1987)
[Stampanoni 87 (2)] M.Stampanoni, D.Pescia, G.Zampieri, G.L.Bona, A.Vaterlaus, and F.Meier, Surf. Sci. 189/190, 736 (1987)
[Thiry 80] *Angle Resolved Photoemission*, Y.Petroff and P.Thiry, Appl. Opt. 19, 3957 (1980)
[Thiry 81] P.Thiry, Thesis (french), Université Pierre et Marie Curie (Paris 1981)
[Weber 90] W.Weber, D.Kerkmann, D.Pescia, D.A.Wesner, and G.Güntherodt, Phys. Rev. Lett. 65, 2058 (1990)
[Weinert 82] M.Weinert, E.Wimmer and A.J.Freeman, Phys. Rev. B26, 4571 (1982)
[White 83] *Quantum Theory of Magnetism*, R.M.White, Springer Berlin 1983
[Wimmer 81] E.Wimmer, H.Krakauer, M.Weinert and A.J.Freeman, Phys. Rev. B24, 864 (1981)
[Yeh 85] J.J.Yeh and I.Lindau, atomic data and nuclear data tables, 32, 1 (1985)
[Zangwill 88] A.Zangwill, *Physics at Surfaces*, Cambridge Univerity press, Cambridge, 1988

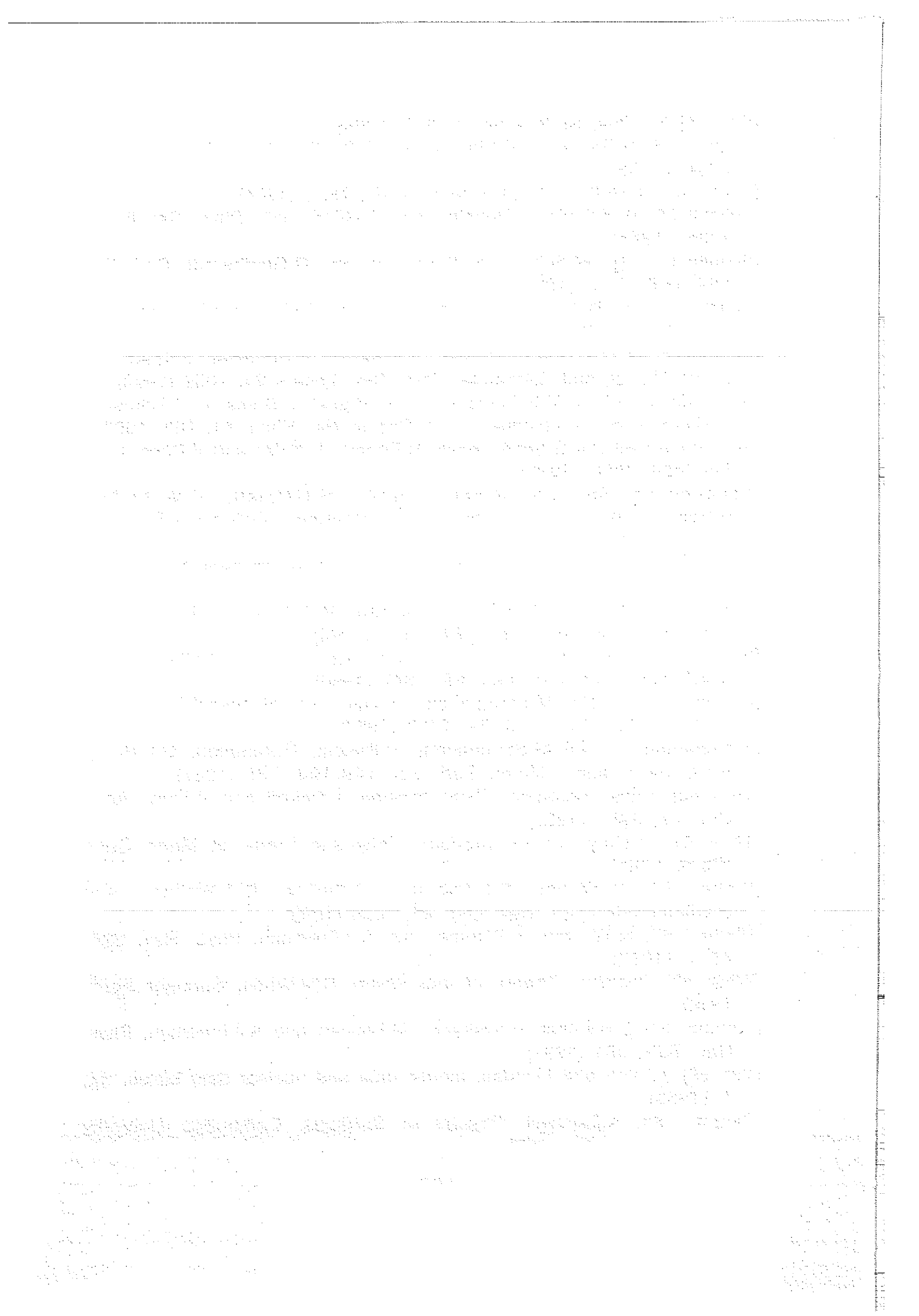

Acknowledgements

This work has been carried out at the *Institut für Elektronische Eigenschaften* (IEE) within the Institut für *Festkörperforschung* (IFF) of the *Forschungszentrum Jülich* (KFA). Work has also been performed at the electron storage ring BESSY in Berlin.

I sincerely want to thank Professor Wolfgang Eberhardt, who has suggested this work, for his encouragement and support. I have worked in the group of Dr. Carlo Carbone from whose experience and knowledge I have profited very much. Many long measuring nights at BESSY I spend with Oliver Rader. I am very grateful to him and to the other group members Dr. Elio Vescovo and Dr. Torsten Kachel. Many thanks to Professor Wolfgang Gudat for the stimulating collaboration with our group. Special thanks also to Ing. Dieter Hoffmann for his technical support.

The calculations have been performed with Dr. Stefan Blügel; I am indebted to him for the time and effort he spent doing the calculations and explaining the theoretical backround.

Many thanks also to all the other members of our institute for their collaboration and for the pleasant atmosphere.

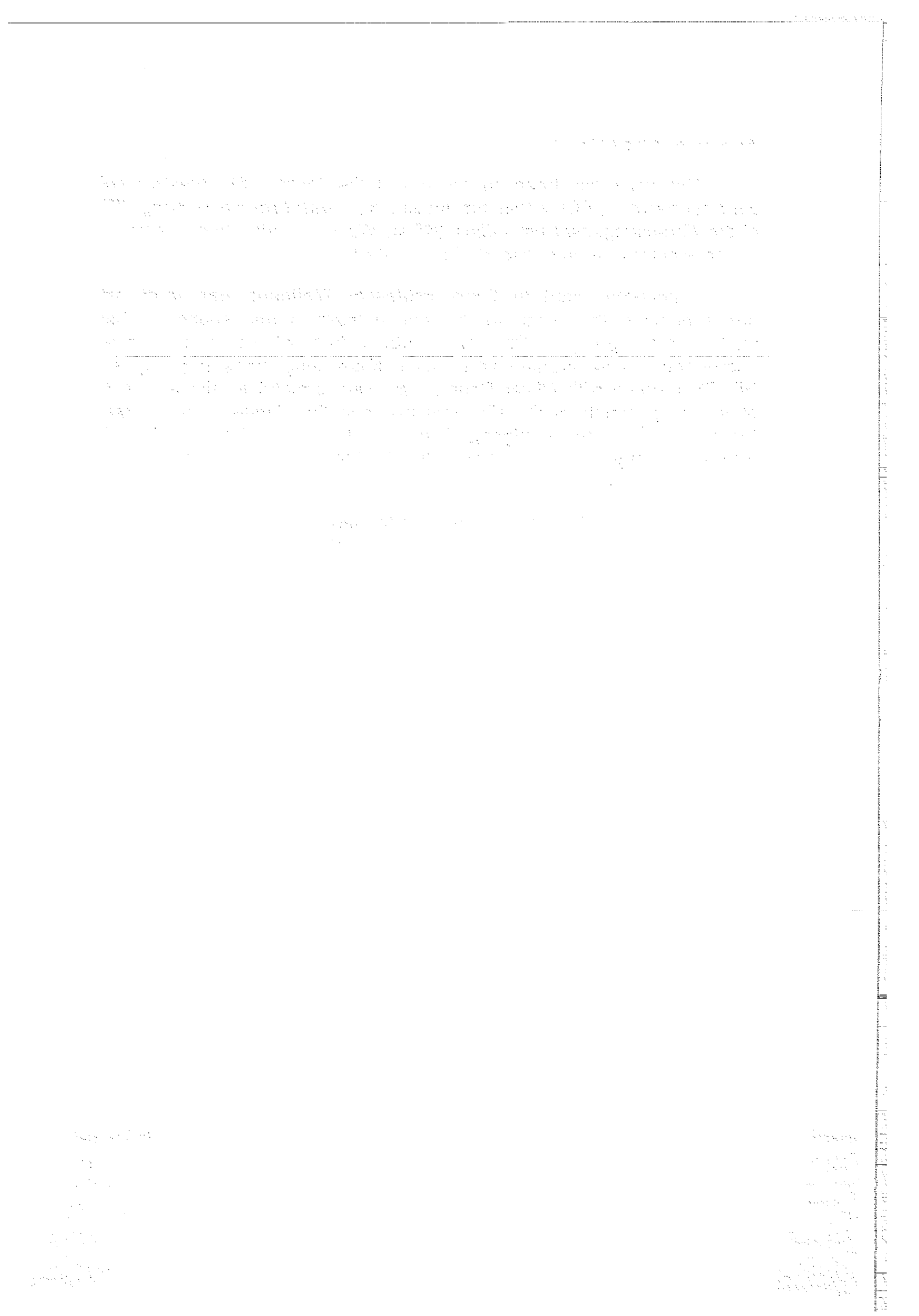

FORSCHUNGSZENTRUM JÜLICH GmbH

KFA

Jül-2601
March 1992
ISSN 0366-0885